Diplomarbeit

Photovoltaic Properties of $SrTiO_{3-\delta}$ in Single Crystalline and Thin Film Cells

zur Erlangung des akademischen Grades eines

Diplom-Ingenieurs

ausgeführt am

Institut für Chemische Technologien und Analytik E164
der Technischen Universität Wien

unter der Leitung von

Univ. Prof. Dipl.-Phys. Dr. rer.nat. Jürgen Fleig
Dipl. Ing. Dr. techn. Alexander Schmid

durch

Ludwig Enzlberger

Matr. Nr. 01525663

Wien, im März 2022

Ludwig Enzlberger

Abstract

Global energy consumption is on the rise and will keep rising in upcoming years induced by technological progress (for example the Internet of Things), but on the other hand further greenhouse gas emissions need to be reduced to mitigate climate change. This raises the question of how both of these goals are to be achieved simultaneously. One possibility consists for example in the harvesting and storage of solar energy by combining solar cells with battery- or fuel cell-technology. This combination of a solar cell and a solid oxide fuel cell (SOFC) is known as a solid oxide photoelectrochemical cell (SOPEC) and should be able to convert sunlight to electrical energy and store it in the form of chemical energy. The obvious problem of this idea is however the fact that typical operating temperature ranges of SOFCs are clearly too high for common, silicon-based solar cells to be able to achieve sufficiently high voltage.

During the course of this work, the properties of $SrTiO_{3-\delta}$ (STO) were examined regarding its applicability for a solar cell that could be combined with an SOFC, as the material is already known to achieve a photovoltage of 1 V even at temperatures above 300 °C. To do this, samples with STO in either thin film or single crystal application were prepared through pulsed laser deposition and photolithography, with Sr-doped $LaCrO_{3-\delta}$ (LSCr) being used as working electrode material. Regarding the counter electrode, Sr-doped $LaMnO_{3+\delta}$ (LSM) was used for thin film samples and porous platinum was used for single crystal samples. The so-prepared cells were operated at temperatures of 300-400 °C as well as atmospheres with varying oxygen content and changes in voltage (open circuit) and current (close circuit) upon illumination with UV light were monitored. Additional analysis on the samples was performed using electrochemical impedance spectroscopy.

As it turned out, STO-based thin film solar cells were unable to achieve photovoltages above 200 mV and deviations from an ideal Sr:Ti-ratio of 1 in the STO-film as well as doping with iron impaired the results even further. The single crystal application of STO on the other hand achieved voltages >1 V and a specific current of ca. 0.8 mA/cm^2 after a long equilibration time. By using synthetic air, this long time equilibration diminished significantly and currents up to 2 mA/cm^2 could be achieved. Also, it could be shown that, unlike in established pn-cells, in all cases the size of the space charge region's resistance is not a suitable indicator to predict the potentially achievable photovoltage.

The single crystal STO-cell prepared in this fashion could possibly be used in combination with e.g. a solid oxide battery to harvest and store solar energy. The exact reason for the inhibition of photocurrent in ambient air remains unclear at the moment and will be subject to further investigation, as well as the question, if and how the photovoltages of STO in thin film solar cells can be improved.

Kurzfassung

Da der weltweite Energiebedarf in den nächsten Jahren durch technologischen Fortschritt (Stichwort: Internet of things) weiter steigen wird, aber zeitgleich CO_2-Ausstoß und der damit verbundene Klimawandel zu unterbinden sind, stellt sich die Frage, wie das bewerkstelligt werden sollte. Eine Möglichkeit besteht beispielsweise in der Nutzung von Sonnenenergie durch Kombination von Solarzellen und Batterie- oder Brennstoffzellentechnik. Eine solche Kombination aus einer Solarzelle und einer Festoxidbrennstoffzelle (SOFC) wird SOPEC (Solid Oxide PhotoElectrochemical Cell) genannt und wäre in der Lage, Sonnenlicht in elektrische Energie umzuwandeln und diese in Form von chemischer Energie zu speichern. Das Problem besteht dabei in der Tatsache, dass übliche Betriebstemperaturen von SOFCs deutlich zu hoch sind, um mit üblichen, siliciumbasierten Solarzellen noch ausreichend hohe Spannungen erzeugen zu können.

Im Zuge dieser Arbeit wurden die Eigenschaften von $SrTiO_{3-\delta}$ (STO) hinsichtlich seiner Eignung für eine solche Solarzelle untersucht, da das Material in der Vergangenheit bereits gezeigt hat, auch bei Temperaturen über 300 °C Spannungen von 1 V zu erreichen. Dazu wurden Proben mittels gepulster Laserdeposition und Photolithographie präpariert, bei denen STO entweder in Dünnschicht- oder Einkristallform zum Einsatz kam und Sr-dotiertes $LaCrO_{3-\delta}$ (LSCr) als Material für die Arbeitselektrode eingesetzt wurde. Gegenelektrode war Sr-dotiertes $LaMnO_{3+\delta}$ (LSM) für Dünnschichtproben und poröses Platin für Einkristallproben. Diese Zellen wurden bei Temperaturen zwischen 300 und 400°C sowie wechselndem Sauerstoffgehalt in der Umgebungsluft betrieben, wobei Änderungen von Spannung (open circuit) und Strom (short circuit) unter UV-Belichtung beobachtet und zusätzlich mittels Impedanzspektroskopie untersucht wurden.

Es zeigte sich, dass STO-basierte Dünnschichtzellen keine Spannung über 200 mV generieren konnten und sowohl eine Abweichung vom idealen Sr:Ti-Verhältnis von 1 in der STO-Schicht, als auch die Dotierung mit Eisen dieses Ergebnis verschlechterte. STO als Einkristall erreichte hingegen Spannungen >1 V und nach längerer Äquilibrierung eine flächenspezifische Stromdichte von 0,8 mA/cm^2. Unter synthetischer Luft fiel diese Äquilibrierungszeit nahezu vollständig weg und der Strom erreichte 2 mA/cm^2. In allen Fällen konnte aber gezeigt werden, dass die Größe des Raumladungswiderstands anders als in etablierten Modellen keine Aussage zur erzeugten Spannung zulässt.

Die so hergestellte STO-Einkristallzelle kann in Verbindung mit beispielsweise einer Festoxid-Batterie eingesetzt werden, um die umgewandelte Energie zu speichern. Woher die Hemmung des Stroms unter Raumluft stammt und ob (und wie) sich die Spannung von Dünnschichtzellen verbessern lässt, werden weitere Untersuchungen zeigen.

Contents

1 Introduction

Starting from the rapid development of industry and technology beginning with the industrial revolution in the 19th century, humanity's influence on it's own prosperity as well as geological and atmospherical processes has massively increased. It has in fact increased so much that in the early 2000s the term "Anthropocene" has been coined to describe our current geological era; an era, where humanity has become the main driving force for the shape and condition of our planet [1]. This has lead to a long list of problems, including (but not limited to) air pollution, extinction of species, overshoot (as in "demand in excess of regeneration") and the change of climate, which has been widely considered one of, if not the greatest challenge in the near future ever since the IPCC's 5th Assessment report [2].
But being the driving force on a global scale also provides humanity with the possibilities to address and fight these issues, while also finding new ways to improve technology and further increase the common standard of living. The general replacement of fossile fuels by "Renewable energies", i.e. the harvesting and storage of abundant energy, has been widely regarded as one of the most important steps in the mitigation of air pollution and climate change because of the omission of pollutants and an overall smaller carbon footprint. Furthermore the eponymous "renewability" is a great way to combat the excessive demand for limited resources. A promising example in this group of technologies is the harvesting of solar energy, which is performed to generate thermal energy through solar thermal energy (STE) panels or electrical energy through photovoltaic (PV) cells, with the latter being the focus of the following work.

When thinking about photovoltaics, cells of crystalline pn-doped silicon come to mind, which are still dominating the market with over 90% of commercially installed solar cells being based on crystalline silicon in 2014 and even among thin film based solar cells, silicon plays an important role [3] [4]. While silicon will surely remain the main compound for solar cells in the following years, given its abundance and relatively low cost, other technologies including the use of organic materials, III/V-semiconductors like GaAs and the already mainstream oriented CdTe- and copper indium gallium selenide (CIGS) PV cells have been thoroughly investigated in recent years [5–8].
A relatively new and still mostly experimental approach to the idea of harvesting solar energy is the use of cheap perovskite-type materials, though these are typically organic-inorganic hybrid materials like methylammonium tin- or lead-halides [9, 10] and fully inorganic oxide-based solutions are commonly less known. Typical uses of solid oxides include junctions of Cu_2O with metals and various other oxides [11–13], although these are not perovskitic materials. Among perovskite oxides, junctions of $SrTiO_3$ (STO) have shown not only interesting UV-induced properties at lower temperatures [14, 15] but also significant voltages upon UV-irradiation at elevated temperatures. Although the mechanism is not yet entirely understood, this is generally attributed to STO showing a combination of photovoltaic (PV) and electrochemical (EC) properties with the latter benefiting from an enhanced oxygen uptake into the material at temperatures of 573 K and above [16–18].
Recent works have shown that junctions of STO with strontium-doped lanthanum chromite ($(La,Sr)CrO_3$/ LSCr) are especially promising due to the high photovoltage of about 1 V that can be generated at the STO/LSCr heterojunction at 350 °C [19, 20], opening the possibility for this material combination to be used in future applications of solar energy harvesting.

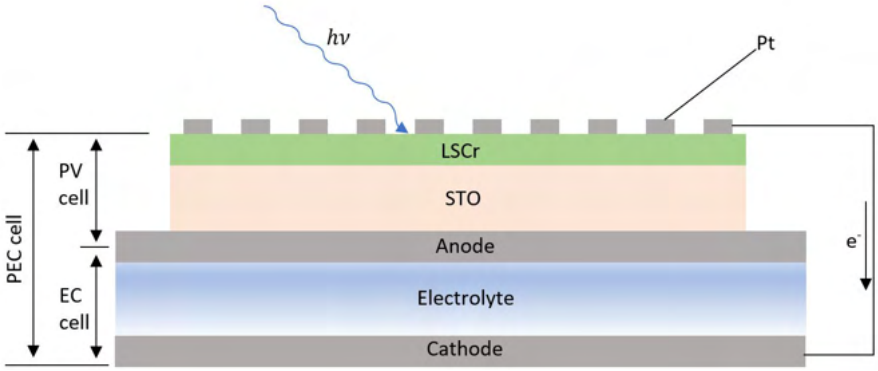

Figure 1.1: Simplified schematic cross-section of a Solid Oxide Photoelectrochemical Cell (SOPEC) with a shared anode following the concept of Brunauer *et al.* [19]

One such application might be a coupling with a Solid Oxide Electrolyzer Cell (SOEC) with a shared anode to create Solid Oxide Photoelectrochemical Cells (SOPECs), as shown in Fig. 1.1, which would be able to harvest solar energy, convert it directly to electrical energy, further to chemical energy by splitting water into hydrogen and oxygen and store it as such. This combination of solar energy harvesting and chemical energy storage would eliminate the problem of solar energy being too unreliable and may prove effective in powering wireless sensor nodes [21], which are nowadays usually powered by common battery technology (NiCd, NiMH, Li-ion) with known downsides such as being high maintenance (batteries need to be replaced) and generally environmentally unfriendly due to the materials used.
Other applications may include usage in high-concentration photovoltaics (see Fig. 1.2), which has seen a massive decline since crystalline silicon has become far cheaper during the course of the last few years [4, 22]. The general functionality of these STO-based cells at elevated temperatures would make this especially cost-efficient since elaborate cooling systems which are currently needed to keep up a sufficient energy conversion efficiency of Si-based solar cells would become obsolete. In space applications, STO solar cells could be used to replace the highly cost intensive GaAs-cells [23, 24], which are currently used because of their higher stability against temperature and radiation compared to common crystalline Si-cells, which show an efficiency decrease of a good 10 % for every 25 K of increased temperature [25].

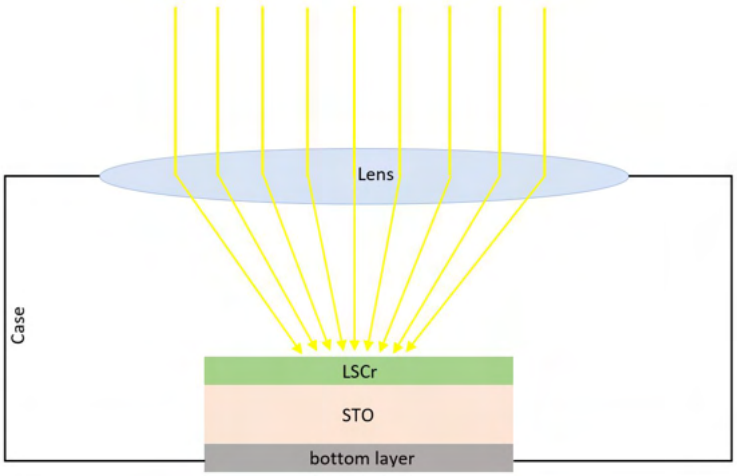

Figure 1.2: General idea of a Concentrator Photovoltaic Cell (CPV) using an LSCr/STO-combination. Today's installments typically use multi-junction solar cells of different semiconductor materials, mostly of the III-V type [26]

For these reasons, STO-based high-temperature PV cells are the topic of the following work, including the already well-researched application of single crystals (SC) and the rather new topic of STO thin-film (TF) solar cells.

To prepare thin films of perovskite materials for electrochemical use, pulsed laser deposition (see Section 2.7) has proven a viable method, making it possible to control the film's composition through variations in temperature, ambient O_2-pressure, laser fluence, distance between target and sample and the composition of the target [27, 28]. This introduces the possibility of researching the effects of cation nonstoichiometry in STO on the generation of photovoltage with relative ease. While the effects of nonstoichiometry on other properties of STO such as conductivity have already been subject to a wide variety of investigations [29–31], its direct effect on photovoltage has not been examined to the best of the author's knowledge. In previous works on Fe-doped STO thin films, these films were grown on Nb-doped STO single crystals and conductivity measurements were performed across plane of the thin films [32]. However, the aim of this work will be to investigate the photovoltages generated by the junctions between (non) stoichiometric STO- or Fe-doped STO (Fe:STO for further reading) and other perovskite thin films (e.g. LSCr or Sr-doped lanthanum manganite (LSM)) through in-plane measurements. There will also be no combination of thin films with single crystalline STO applications, as the films are grown on photovoltaically inactive yttria stabilized zirconia (YSZ) substrates (see 3.1.1).

Additionally, cells based on nominally stoichiometric STO single crystal substrates and perovskite top layers are investigated. Such cells have already demonstrated to generate high photovoltages and early results hinted at a complex time dependency of the photocurrent produced by these single crystal based cells [20], with current steadily increasing over time upon UV irradiation of the cell.
In this work, this behaviour of photocurrent will be systematically investigated through current measurements and impedance spectroscopy to find out if and when an equilibrium current I_{eq} is reached and how this is affected by temperature, oxygen partial pressure and the material used for the working electrode with the aim of explaining the reason behind this "current enhancement".

2 Theoretical Background

2.1 Defects in ionic solids

Since the scope of this work deals with the effects caused by defect chemical phenomena, an introduction on the general behaviour of defects in ionic solids and their role in influencing electrical properties will be given here.
Crystalline solids, as opposed to amorphous materials, are characterized by their lattice-periodic structural buildup. While amorphous solids show repeating units, such as the tetrahedral SiO_4 structure in SiO_2-glass, the arrangement of these units varies greatly throughout the whole material, whereas in crystalline solids the repeating units are arranged in the same way periodically in every spatial direction. The smallest repeating units of crystals are known as "unit cells", being comprised of an atomic basis and the vectors spanning the points of the respective lattice. Generally, the translation symmetry of an n-dimensional lattice is given by the translation vector $\vec{T}$ in Equation (2.1), although for real life applications no dimensions greater than $n = 3$ are needed, leading to Equation (2.2).

$$\vec{T} = \sum_{i=1}^{n} u_i \vec{a}_i, \qquad \text{where } u_i \in \mathbf{Z} \quad \forall i \tag{2.1}$$

$$\vec{T} = u_1\vec{a}_1 + u_2\vec{a}_2 + u_3\vec{a}_3 \tag{2.2}$$

In this depiction, the vectors $\vec{a}_i$ span the parallelepiped of the cell with the smallest possible volume and u_i are integers which leave the cell invariant to translation [33]. The unit cell created in this fashion is called a "primitive cell" and contains only one lattice point (an atom) sitting at the (0,0,0)-corner of each cell. More often than not cells containing additional lattice points are used to describe structures for convenience of calculation or simply to make structures easier to distinguish. These are known as "conventional" cells, whose volume is an integer multiple of the primitive cell since their number of lattice points also has to be an integer multiple of 1 [34]. In Figure 2.1 the connection of the face centered cubic (fcc) conventional cell to its respective primitive cell is shown as an example.

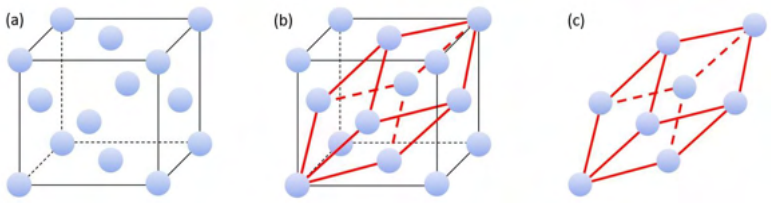

Figure 2.1: "Finding" the primitive cell inside a conventional cell. A conventional fcc cell (a) contains the primitive rhombohedral cell (c) by starting from one lattice point and moving halfway across the cell's surface in every spatial direction (b)

An ideal crystal would consist of unit cells being repeated periodically in every direction ad infinitum without any gaps or overlaps between them. This is, however, not true for real crystals, as there are obviously no crystals that are infinitely large. Real, finite crystals have surfaces that can also be characterized as a layer of "incomplete cells" with some of the bonds of the surface atoms left "dangling" as there are no coordination partners. Since these dangling bonds are thermodynamically unfavorable, the crystal will rearrange its surface atoms and create surface structures that differ from the bulk structure at temperatures above 0 K to keep its Gibbs energy (Equation (2.3)) low. This behaviour is called surface reconstruction [35] and is well known for many materials such as the dimerisation of Si-[100] surfaces [36]. Similar to surfaces, grain boundaries in polycrystalline materials and interfaces in composite materials are also examples of "faults" in crystals and generally behave differently compared to the single crystalline bulk.

$$\Delta G = \Delta H - T\Delta S \tag{2.3}$$

But it is not only the infinite periodicity of theoretical crystals that is commonly infringed in real crystals. Also the idea of unit cells being repeated seamlessly throughout the crystalline solid does not hold true and there are a number of different kinds of deviations from the theoretically fully ordered structure, which are known as "defects" in the crystal. Defects are entropically favoured as they break the crystal's order and will thus always be present in crystals above 0 K with their formation becoming more likely at higher temperature. They are substantial for the properties of crystalline solids and are commonly subdivided by their dimensional expanse, i.e. 0-, 1-, 2- and 3-dimensional defects. As shown in Table 2.1, different types of defects influence different properties of the material with varying degree of severity. While dislocations (1-dimensional defects) are essential for a metal's basic mechanical traits, volume defects are especially interesting considering the hardening of metals or the general mechanical stability of ceramics.

Table 2.1: Different types of defects in crystalline solids, following [37, 38]. Note that only an exemplary selection of physical properties mainly influenced by the respective defects is given.

Geometrical Dimension	Type of Defect	Energy	Physical Properties
0	vacancy, interstitial, antisite	J	diffusion, el. conductivity, F-centers
1	edge, screw	$J\,m^{-1}$	ductility, shear modulus
2	grain boundary, stacking fault	$J\,m^{-2}$	texture, corrosion
3	pores, particles, precipitation	$J\,m^{-3}$	porosity, misc. mechanical properties

2.1.1 Point defects in ionic solids

Notation of defects

Among the different types of defects, point defects in solids are by far the most influential factor for solid state ionics as they are the only defects that facilitate the transport of ions [39]. Thus a short introduction on the different types of zero dimensional defects - including intrinsic and extrinsic electronic and ionic defects - shall be given.
These defects in ionic solids are commonly described in chemical equations in a systematic approach introduced by Kröger and Vink in the mid-50s [40] and has become the international standard during the following decades.
The general idea of Kröger-Vink notation consists of three points:

- The main symbol *M* (Material): This indicates the species of the defect, which can either be an ion or a vacancy. In the case of delocalized electronic defects, this can also be an electron or a hole. While ionic defects are denoted with their respective atomic symbol from the periodic table of elements, vacancies are indicated with a "V". To avoid confusion with the element Vanadium, this is sometimes switched with a lowercase "v", a script "ν" or a simple □-symbol should the need arise [41].
- The subscript *S* (Site): Indicates the lattice site occupied by the defect, again with the element's atomic symbol or a lowercase "i" (to avoid confusion with I for Iodine) if the defect occupies an interstitial site.
- The superscript *C* (Charge): Indicates the difference in charge that arises from the defect relative to the charge at the site in an ideal crystal. A positive charge is denoted by a dot •, a negative charge is denoted by a slash ′ and to show that the defect does not change the charge of the lattice site, an ×-symbol is written.

This is illustrated in Equation (2.4), which shows the example of a vacancy (V) occupying an oxygen-lattice site (subscript O) resulting in two positive charges (••) at this site. Further examples are given in Table 2.2.

$$M_S^C \longrightarrow \mathrm{V}_{\mathrm{O}}^{\bullet\bullet} \tag{2.4}$$

Table 2.2: Various examples of Kröger-Vink Notation

Type of defect	Notation
Cation Vacancy in NaCl	$\mathrm{V}'_{\mathrm{Na}}$
Anion Vacancy in $SrTiO_3$	$\mathrm{V}_{\mathrm{O}}^{\bullet\bullet}$
Cation Interstitial in AgBr	$\mathrm{Ag}_{\mathrm{i}}^{\bullet}$
Ca^{2+} on Na^+-site in NaCl	$\mathrm{Ca}_{\mathrm{Na}}^{\bullet}$
K^+ on Na^+-site in NaCl	$\mathrm{K}_{\mathrm{Na}}^{\times}$
Electron localized on Fe^{3+}	$\mathrm{Fe}'_{\mathrm{Fe}}$
Delocalized hole in the band	$\mathrm{h}^{\bullet}$

Intrinsic defects

Crystallographic defects that are solely based on the material's inherent entropically favored tendency to form them within the pure crystal without the influence of any impurities are known as intrinsic defects. While it is clear from Equation (2.3) that the defects can only exist if the entropic gains ΔS balance or outweigh the formation enthalpy ΔH, there are some conservation rules to be considered for a self-consistent treatment of defect chemistry.

- Conservation of mass: Within whatever given system, atoms/ions can never be created or destroyed, but must be conserved.
- Conservation of charge: Since the totality of the bulk crystal is electrically neutral, charged defects can only occur in pairs that are also electrically neutral. This means that in ionic solids the creation of positively charged defects must lead to equally negatively charged defects and vice versa.
- Conservation of structure: As well as the total charge of the crystal, the lattice site ratios of cations to anions is constant, meaning that the creation of defects has to conserve the stoichiometric composition of the compound and cation and anion sites can only be created or destroyed in electrically neutral combinations [42].

These rules lead to two main types of pair-wise intrinsic defect combinations that appear in ionic compounds:

(a) Frenkel defects (see Equation (2.6)), where the migration of an ion inside the lattice to an interstitial site leads to the formation of a vacancy, hence fulfilling the neutrality of charge. Thus the defect combination of Frenkel defects stems from one and the same ion. Since this is the smaller cation in most cases, the specific case of an anion leaving its lattice site is generally referred to as an "anti-Frenkel" defect.

(b) Schottky defects, where a cation- and an anion-vacancy fulfill the conservation of charge and stoichiometry. While Frenkel defects mainly occur in crystals with large unoccupied vacancies like octahedral sites (Spinels, Fluorites), Schottky defects often occur in lattices that do not offer enough space for an interstitial atom like NaCl-type compounds of alkali- and alkaline earth metals [43].

The formation of intrinsic defects in solids and their contribution to the conductivity of the material has been described in literature [39,44,45] as similar or equivalent to the auto-protolysis of water, which is also essential for electrical and ionic conduction. And it can indeed be easily seen that

$$H_2O + H_2O \rightleftharpoons H_3O^+ + OH^- \tag{2.5}$$

in water shows a significant resemblance to the formation of Frenkel defects like

$$Ag_{Ag}^{\times} + V_i^{\times} \rightleftharpoons Ag_i^{\bullet} + V'_{Ag} \tag{2.6}$$

in AgCl for instance.

This means that analogous to the acid/base-equilibrium in aqueous solutions a law of mass action for the formation of intrinsic defects can be postulated as in Equation (2.7) with A and B being the oppositely charged defect species, n the concentration of species and ΔG, ΔS, ΔH referring to the standard free energy, the local entropy and the enthalpy for the formation of defects [46,47].

$$K(T) = n_A n_B e^{-\Delta G/kT} = n_A n_B e^{\Delta S/k} e^{-\Delta H/kT} \tag{2.7}$$

The dependency of the equilibrium constant K on the temperature T is a logical continuation of the general temperature-dependency of defect formation according to the standard Gibbs free energy change as

$$-\Delta G = kT \ln K(T) \tag{2.8}$$

Extrinsic defects

After considering crystals with only negligible or no impurities at all, we will now take a closer look at the impacts of foreign atoms being introduced into the lattice. These are extrinsic defects and though they are often undesired, the act of deliberately changing a material's properties through the precise introduction of said imperfections is known as doping. A prominent example of increasing a compound's qualities through this technique is the doping of ZrO_2 with Y_2O_3. Following the rule of charge conservation, the lower valence of the Y^{3+} ions taking the site of Zr^{4+} ions leads to the creation of an oxygen vacancy for every 2 Zr^{4+} ions replaced according to Equation (2.9). While this material combination makes the compound suitable for a range of mechanical applications including ceramical knives and thermal barrier coatings for turbines [48], the purposeful creation of these vacancies also enhances the yttria-stabilized zirconia's (YSZ) selective conductivity of oxygen-ions at elevated temperatures and makes it especially viable for electrochemical purposes such as electrolytes for solid oxide fuel cells (SOFCs) or oxygen sensors [49].

$$Y_2O_3 \longrightarrow 2\,Y'_{Zr} + 3\,O_O^{\times} + V_O^{\bullet\bullet} \tag{2.9}$$

Following the analogy of aqueous solutions the effects of dopants may be compared to increasing the concentration of H_3O^+ and OH^- ions in water by adding strong acids or bases respectively and are thus often strong enough to outweigh the contributions of intrinsic defects entirely. Akin to acids being considered donors (of H^+ ions) and bases being considered acceptors according to the Brønsted-concept, dopants in solid state ionics are generally divided into donor and acceptor dopants. But unlike in deformable fluids where the dissolution of cations and anions generally takes place simultaneously this is not the case in solids and only one type of ion (cation or anion) can usually be introduced into the compound [50], meaning that e.g. cationic doping of ZrO_2 is possible with Y_2O_3 but not with YF_3. Conversely, anionic doping of $LaFeO_3$ can be done using $LaCl_3$ but not YCl_3.

In the case of cations, donor dopants show a positive charge relative to the site they inhabit leading to the formation of negatively charged defects to conserve charge neutrality. Conversely, acceptor dopants show a negative charge relative to the site inhabitated and lead to the formation of positively charged defects as shown above in the case for YSZ with anion vacancies being formed upon doping the compound with cations of lower valence.

2.1.2 Non-stoichiometry in metal oxides

Additionally to "classic" defects, where charge neutrality in the crystal is preserved after the creation of one defect through the creation of an additional defect of opposite charge, thus also preserving the cation/anion-ratios that correspond to the stoichiometry of the compound, ionic solids can also show defect formations that infringe their stoichiometric composition. In the instance of Metal Oxides we can differentiate between two cases: Cation nonstoichiometry, where the compound shows a metal deficiency (or surplus) and anion nonstoichiometry or just oxygen nonstoichiometry to be more precise, with the latter being highly dependent on the oxygen partial pressure of the surrounding atmosphere. In any case, the degree of nonstoichiometry is generally denoted by a δ, e.g. $SrTiO_{3-\delta}$. This deficiency δ of course brings in defects, such as oxygen vacancies ($V_O^{\bullet\bullet}$) or metal ions on interstitial sites ($M_i^{\bullet\bullet}$) creating more positive charge. But even though the stoichiometry may be violated, electroneutrality still has to be preserved across the crystal, resulting in the partial reduction (or oxidation) of cations.

For one, this means that the extent of nonstoichiometry is highly dependent on the reducibility of cations, implying that compounds like NiO, FeO or CoO, where the metal is in a M^{2+} state generally show metal deficiencies (since this is the metal's lowest stable oxidation state), whereas SnO_2 or titanates generally show oxygen deficiencies. Compounds of single-valent metals mostly do not show any non-stoichiometric behaviour of relevance at all [39, 51, 52].
But more importantly this means that nonstoichiometry is essential for not only the introduction of ionic defects but for electronic charge carries as well. Similar to how ionic pairs of defects are formed in the compound itself, this behaviour leads to the formation of mobile electrons (e') and holes ($h^{\bullet}$) in the band structure of the solid. Since the stoichiometry of an oxygen-deficient metal oxide $MO_{1-\delta}$ is mainly determined by the equilibrium with the surrounding atmosphere, the formation of defects also depends on the ambient oxygen partial pressure and can be illustrated in the form of a Brouwer diagram (sometimes referred to as Kröger-Vink diagram [52]) as shown in Figure 2.2.

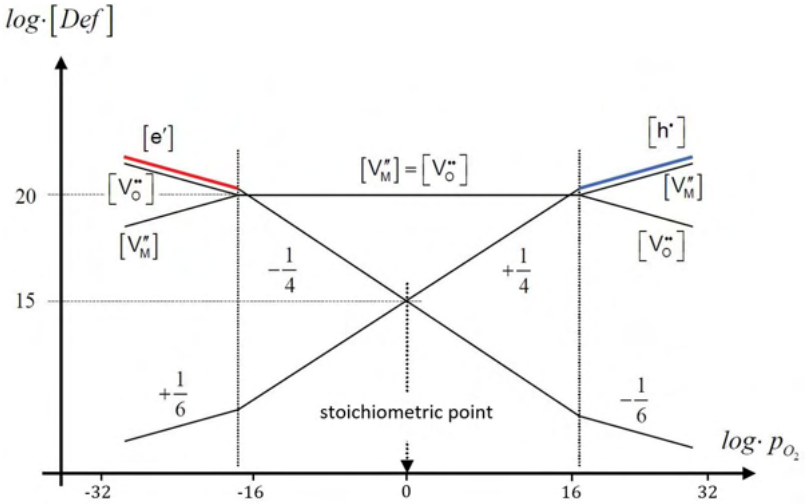

Figure 2.2: Simplified Brouwer diagram of a metal oxide following [53], showing the relation of oxygen partial pressure and defect concentration. The areas of dominating electron- and hole-conductivity have been highlighted in red and blue respectively.

The interaction of the compounds oxygen-nonstoichiometry with the surrounding gas can be written as

$$O_O^{\times} \rightleftharpoons \frac{1}{2} O_2 + V_O^{\bullet\bullet} + 2\,e' \tag{2.10}$$

together with the mass action law

$$K = \frac{[V_O^{\bullet\bullet}] \cdot [e']^2 \cdot p_{O_2}^{1/2}}{[O_O^{\times}]} = K_{Red}^{o} \cdot e^{\frac{-\Delta H_{Red}}{k_B T}} \tag{2.11}$$

Assuming that the activity of standard conditions is 1, one can write the defect mass action constant K_δ as

$$K_\delta = [V_O^{\bullet\bullet}] \cdot [e']^2 \cdot p_{O_2}^{1/2} \tag{2.12}$$

Combining this with the concentration of electrons given by charge neutrality

$$[V_O^{\bullet\bullet}] = 1/2[e'] \tag{2.13}$$

leads to the following relation:

$$K_\delta = 1/2 \cdot [e']^3 \cdot p_{O_2}^{1/2} \tag{2.14}$$

$$[e'] = \sqrt[3]{2\,K_\delta} \cdot p_{O_2}^{-1/6} \tag{2.15}$$

explaining the -1/6 slope of electron formation outside the stoichiometric range in the Brouwer diagram, which is commonly found in the examples of oxygen-deficient compounds mentioned above.
Similarly this can be done for hole-concentration reaching a +1/6 slope starting from Eq. (2.16) and following through to find Eq. (2.17).

$$\frac{1}{2} O_2 \rightleftharpoons O_O^{\times} + V_M'' + 2\,h^{\bullet} \tag{2.16}$$

$$[h^{\bullet}] = \sqrt[3]{2\,K_\delta'} \cdot p_{O_2}^{1/6} \tag{2.17}$$

2.1.3 Charge transport in solids

The transport of charge in ionic solids can either happen through ionic or electronic transport. In most solids, one of the paths is strongly favoured, but there are also mixed electronic and ionic conducting materials (MIECs) with similar ionic and electronic conductivities, including fluorites such as CeO_2 or perovskites like $SrTiO_3$ [54]. Both cases are dependent on both diffusion and the applied electric field strength making the total current density consist of two parts, the field current J_F and the diffusion current J_D according to Equation (2.18) [55].

$$\vec{J}_{tot} = \vec{J}_F + \vec{J}_D = \sigma \cdot \vec{E} - q \cdot D \cdot \vec{\nabla} n \tag{2.18}$$

Here, q denotes the charge of a single charge carrier and n the charge carrier density. As well as the diffusion coefficient D they are contributing to the diffusion current term.

The field current term consists of the electric field strength $\vec{E}$ and the conductivity σ, which in itself is the sum of the contributions of all charge carriers according to Equation (2.19).

$$\sigma_{tot} = \sum \sigma_{ion} + \sigma_e + \sigma_h \tag{2.19}$$

The conductivity contribution σ of a single charge carrier i is given by Equation (2.20) and is proportionally dependent on its charge z, mobility u and concentration c.

$$\sigma_i = |z_i| \cdot e \cdot u_i \cdot c_i \tag{2.20}$$

Ionic conductivity

Ionic conductivity is typically not a constant, smooth motion but instead better described as a "hopping" mechanism, where an ion moves one lattice site at a time. In literature [56, 57], commonly three mechanisms for ion mobility are described, which are also shown in Figure 2.3:

- Ion movement by the **vacancy mechanism** allows an ion to move into an adjacent vacancy. Therefore the ion remains immobile until the vacancy moves up to it, allowing for it to move one lattice site in the given direction. Since every ion only makes a single move in one direction in this case it is convenient do describe the vacancy as the moving species.
- The **interstitial mechanism** describes an interstitial species hopping from one site to the next. This process comes to a temporary halt should the interstitial recombine with a vacancy.
- Finally the **interstitialcy mechanism** describes a variation of the interstitial mechanism with one significant difference: Here, an interstitial ion displaces a normal lattice ion, which then becomes a new interstitial ion. This difference is of special importance in tracer diffusion, where the migrating species can be identified.

This step-wise movement of ions is owed to the fact that ions need to overcome an energy "barrier" to leave their respective lattice site. It is thus helpful to describe the mobility term u_i as an approximated Arrhenius-type function with Δg_b representing the barrier height.

$$u_{ion} = D_0 \cdot \left(\frac{z_i e_0}{k_B T}\right) \cdot e^{\frac{-\Delta g_b}{k_B T}} \tag{2.21}$$

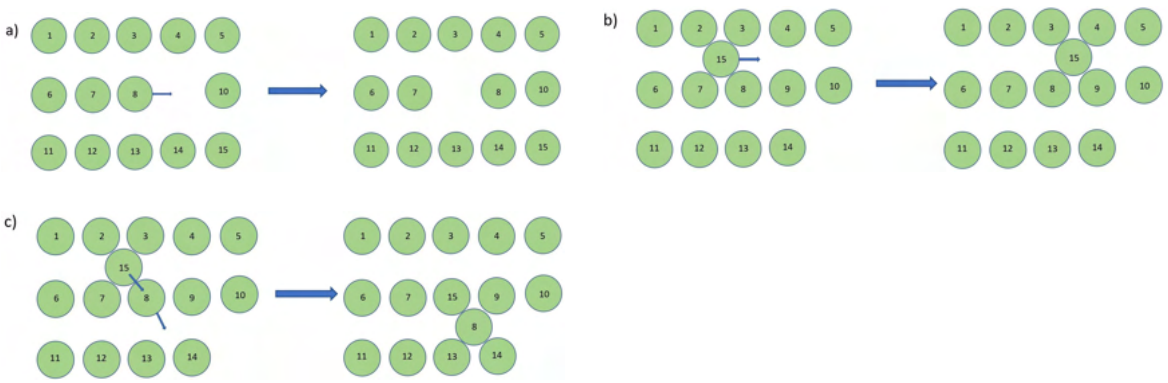

Figure 2.3: Mechanisms of defect "hopping" in crystalline solids: a) the vacancy mechanism, b) the interstitial mechanism, c) the interstitialcy mechanism

The similarity of Equation (2.21) to the classic diffusion coefficient D in solids is obvious and the two are indeed related through the Nernst-Einstein equation

$$u_i = D_i \frac{z_i e_0}{k_B T} \tag{2.22}$$

Electronic conductivity

The conductivity of electronic charge carriers in ionic solids can generally take two forms. To begin with, it is a useful approximation to imagine electrons and holes being localized on cations in the compound. This entails that the neighbouring ions are affected by the additional charge on the respective cation, leading to a distortion of the lattice depending on the type of charge (attraction of cations and repelling of anions in the case of an electron and vice versa in the case of a hole). This concept is known as a "polaron" [53, 58]. If this interaction is weak, the polaron is called a large polaron and the electronic mobility can be described by a band-like structure. In this case the electronic mobility u_{eon} is governed by phonon scattering processes similar to metals and the temperature dependency is given by

$$u_{eon} \sim \frac{1}{T^{3/2}} \tag{2.23}$$

If the polaron interaction is strong, the electrons can not move as freely anymore and a hopping mechanism similar to the one for ionic conduction takes place, where an electron or hole "jumps" from one ion to another. However, some adjustments have to be made from Equation (2.21) to properly describe the mobility of electronic charge carriers. For one, they can only carry a single charge, omitting the z_i. Additionally, the ion that the electron or hole jumps to has to be suitable. An electron positioned on a Ti^{4+} ion (making it a Ti^{3+} ion) has to find another near Ti^{4+} ion that is available. If the total number of occupied sites is denoted by ϕ one can write $(1-\phi)$ to account for available sites for electronic charge carries to go to and state the electronic mobility u_{eon} by hopping as

$$u_{eon} = (1-\phi) \cdot D_0 \cdot \left(\frac{e_0}{k_B T}\right) \cdot e^{\frac{-\Delta g_b}{k_B T}} \tag{2.24}$$

With the concentration of defects also being dependent on temperature, as stated in the beginning, and different types of charge carriers all being present in MIECs, the total conductivity becomes a complex issue.
This is further enhanced by the fact that the conductivity is perturbed when a charge carrier encounters impurities of higher dimensions, such as surfaces or interfaces; either in grain boundaries or through direct contact with another conducting material.

2.1.4 Interfaces and space charges

Charge transport across grain boundaries

With grain boundaries being a type of 2-dimensional defect as discussed above, it is only natural to assume that they present a different chemical environment for charge carriers when compared to the crystalline bulk. If we consider an ionic solid with one predominant mobile defect (say $V_O^{\bullet\bullet}$), the difference in the chemical potential μ for this species between the bulk and the boundary will lead to it accumulating at the point of μ_{min}.

Accordingly, this creates a field current J_F, where in the case of a positively charged grain boundary the electrons will be attracted and create a negatively charged space charge region adjacent to the core, which is the structural grain boundary, as portrayed in Figure 2.4. This again leads to a depletion of oppositely charged defects (in our case oxygen vacancies) inside the space charge region, finally resulting in a strong decrease in conductivity [59, 60]. The full distribution of defects across the space charge region is given by the Poisson equation

$$\frac{d^2\phi}{dx^2} = -\frac{\rho}{\varepsilon\varepsilon_0} \tag{2.25}$$

with ϕ denoting the resulting local potential with respect to the bulk, ρ describing the charge density at a position x away from the core and ε being the relative dielectric constant of the semiconductor (ε_0 = vacuum permittivity) [61]. This general case of electron accumulation and resulting highly resistive grain boundaries has been found and computationally described for many compounds, e.g. crystalline [62] and nanocrystalline [63] $SrTiO_3$, although there are also cases of conductive grain boundaries [64].

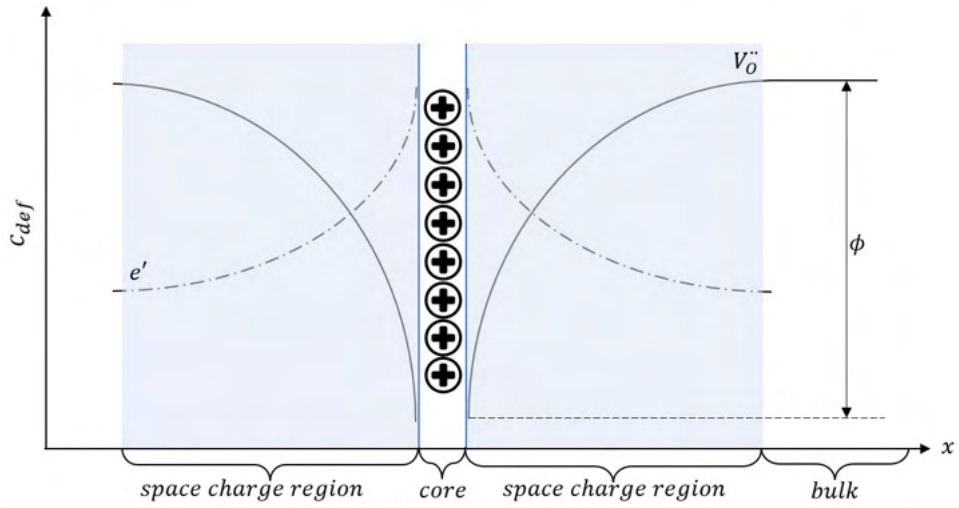

Figure 2.4: Schematic description of the charge carrier distribution around a grain boundary. With the adjacent space charge regions on both sides the electrical grain boundary becomes much larger than the structural one.

Electrode/Electrolyte junctions

While grain boundaries introduce defects inside the electrolyte material, these defects are symmetrical and the charge carriers find the same bulk material on both sides of the interface. The junction between an electrode and an electrolyte, however, introduces the problem that the carriers now face a very different environment after passing through the barrier, which may not have the same conductivity anymore. Depending on the type of electrode, this may either be a metal-semiconductor (M-S) or a semiconductor-semiconductor (S-S) junction. This section will mostly cover the topic of M-S junctions, for S-S junctions see below.
M-S junctions can also be split into two categories: rectifying and non-rectifying. Non-rectifying junctions have little to negligible impediment to the conduction of charge carriers, show a linear behaviour in the I-V curve and are thus called ohmic contacts. Rectifying junctions, on the other hand, show behaviour similar to the space charge layers discussed above.

The significant difference is the asymmetry of the junction shown in Figure 2.5, which is known as a Schottky-barrier [65]. Upon bringing a semiconductor in contact with a metal, the semiconductor's Fermi-level E_F must match that of the metal. This leads to a "band-bending" in the semiconductor's surface region, resulting in the creation of a barrier (Fig. 2.5 b)) Φ_B. In theory, the height of the Schottky-barrier is given by the difference between the metal's work function Φ_M and the electron affinity of the semiconductor χ_S according to the Schottky-Mott rule

$$\Phi_B \approx \Phi_M - \chi_S \tag{2.26}$$

leading to some electrons wandering from the semiconductor's conduction band into the metal's surface and thus creating a depletion zone in the semiconductor [66, 67]. In reality, while the Schottky-Mott approximation correctly predicts the band bending, it has been found that the work function of the metal is often not very important for a prediction of the barrier height. The Fermi-level pinning is in fact owed to electronic states in the semiconductor's band gap induced by the metal upon contact. Due to their high density, the position of these states is relatively stable independent of the metal used [68, 69].

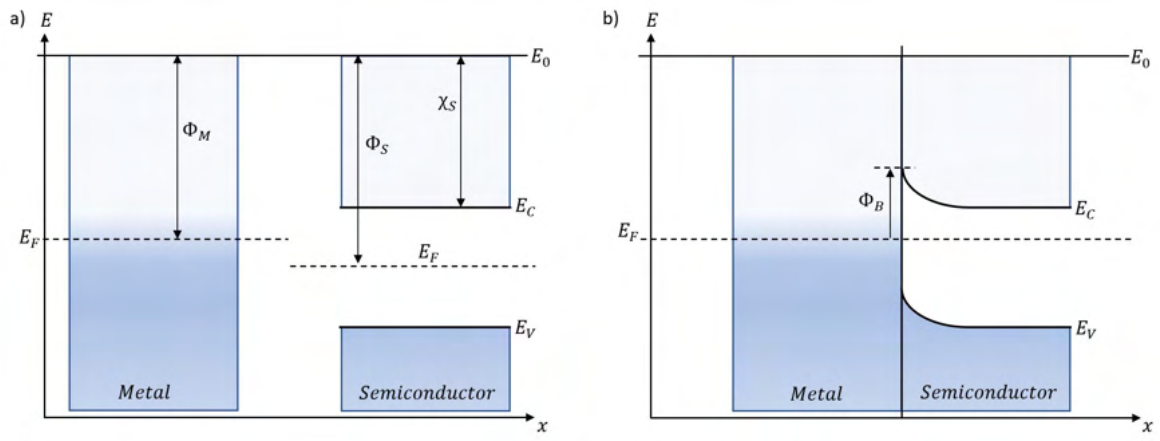

Figure 2.5: Creation of a Schottky barrier Φ_B upon contacting a metal with a semiconductor. a) Metal and semiconductor with a little bit of vacuum space between them. b) Band bending of the semiconductor forming a Schottky barrier at the interface upon contacting the metal. In this case the conduction band of the semiconductor is slightly depleted in e′ and the metal's valence band equally enriched

If a forward bias is applied, electrons from the semiconductor's valence band can be excited into the depletion zone, lowering the barrier height and making carrier flow possible. The application of a reverse bias, on the other hand, leads to the electrons being pulled away from the depletion zone and effectively broadening it. This gives the Schottky-junction its characteristic rectifying properties. To avoid this, semiconductors are commonly precisely doped in a way that minimizes the barrier height and leads to ohmic behaviour. Thus, a Schottky diode typically consists of two metal parts with a semiconductor in between that creates a Schottky barrier with one metal and an ohmic contact with the other [70]. In many ways, Schottky junctions resemble p-n junctions, but the differences will be discussed in the following section.

p-n space charges and photovoltaic application

As stated, p-n junctions act similar to Schottky junctions to the effect that in both cases depletion regions of charge carriers lead to rectifying behaviour. However, unlike Schottky junctions, p-n junctions happen at an S-S interface or to be more precise: At the interface of the same semiconducting material that is partially p- and partially n-doped. A junction of two semiconductors with the same bandgap (including the same material with different doping levels) is known as a "homojunction" [71].

The differing concentrations of electrons on both sides (excess on the n-side and shortfall on the p-side) leads to the formation of a gradient that the system counters by letting electrons diffuse into the p-doped side at the interface as shown in Figure 2.6 a. Accordingly, holes from the p-side will move to the n-doped side, thus creating a diffusion current J_D. This in turn creates an electric field on the interface and a correspondent field current J_F opposing further diffusion of charge carriers. At equilibrium, a steady state $J_F = J_D$ is reached, which means that according to Equation (2.18), no total current remains. With the electrons and holes now having recombined on both sides of the interface, a space charge region remains that is depleted of free charge carriers. Similar to the Schottky-barrier, this depletion region shows rectifying behaviour with the electrons (and holes) only being able to flow if a forward bias, i.e. a voltage whose electric field is opposing the field of the barrier, is applied. A reverse bias would again only lead to broadening of the space charge layer [72].

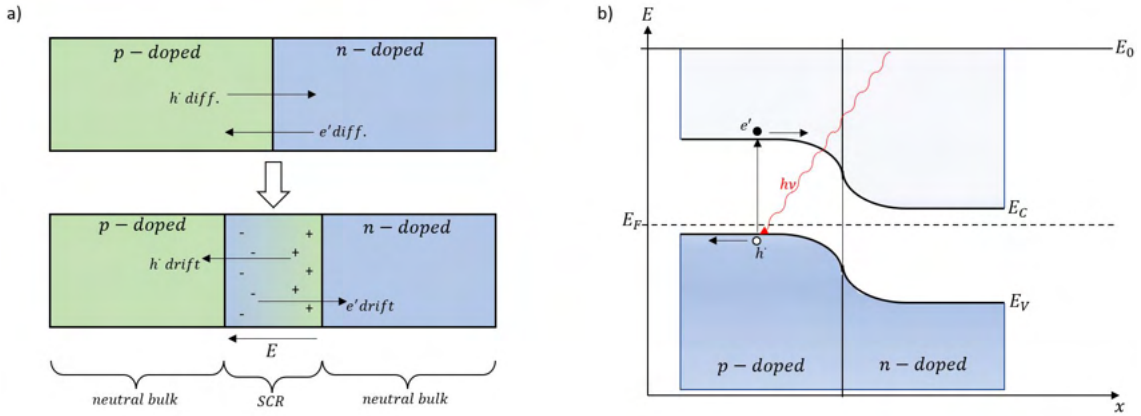

Figure 2.6: a) Creation of a space charge region (SCR) at the interface of a p- and an n-doped semiconductor. E denotes the electric field of the space charge. b) Simplified band structure of a homojunction and photovoltaic effect. A photon excites an electron into the conduction band and creates a hole in the valence band

Aside from the obvious application of p-n junctions in the form of diodes and transistors, this is also relevant for the working principle of classic silicon PV cells in combination with the photovoltaic effect. A photon with an energy greater than the band gap of the semiconductor can be absorbed into the material and excite an electron from the p-doped side of the space charge layer from the valence band to the conduction band. There, it can move freely and is able to overcome the barrier of the depletion zone. The same applies to the hole created by the removing of an electron, leading to the same effect as an applied forward bias and making the space charge layer collapse.

It is common today to engineer solar cells to get preferably wide depletion zones, for example by putting a weakly doped or undoped intrinsic semiconductor region between the n- and the p-region, creating a p-i-n structure, which allows carrier generation deeper inside the material, increasing quantum efficiency and proof voltage [73]. Having the interjected region slightly p-doped raises the efficiency further, since the carrier separation has to happen on the p-doped side of the junction as shown in Figure 2.6 b and broadening this region statistically increases the number of carriers [74].

Heterojunctions

Unlike the now discussed homojunctions, where differently doped variations of the *same* material form an interface, there are also cases where dissimilar semiconductors are brought together. Since they commonly also have different band gaps, this type of junction is called a "heterojunction". Heterojunctions generally show behaviour similar to Schottky- and pn-junctions, but the higher complexity of their interface region allows for greater flexibility in design and enables new functionalities.

There are two ways to classify heterojunctions: For one, the continuity of the band gap at the interface can be used to find two different types; a graded heterojunction with a continuous transition between the band gaps of the compounds over a relatively long distance and an abrupt heterojunction with a discontinuity at the interface and little interdiffusion between the connected semiconductors similar to the barrier in Schottky-junctions [75]. Abrupt junctions can be further classified by the type of mismatch, with ΔE_C and ΔE_V referring to the offsets of the conduction and valence bands respectively, so that $\Delta E_C + \Delta E_V = \Delta E_g$, the difference in bandgap energy. As shown in Figure 2.7 this can either be a nested (or "straddling") type (a), where the energy differences have the same sign (defined to be positive) and electrons and holes are typically both confined in the material with the smaller bandgap, or a staggered type (b) with opposing signs of ΔE_C and ΔE_V, leading to electrons and holes being confined in different layers. This type of heterojunction is closest to pn-junctions in terms of structure and behaviour. Rarely, a misaligned (or "broken") type (c) is found as a special case of (b), where the offset between the bandgaps is larger than at least one of the gaps [76].

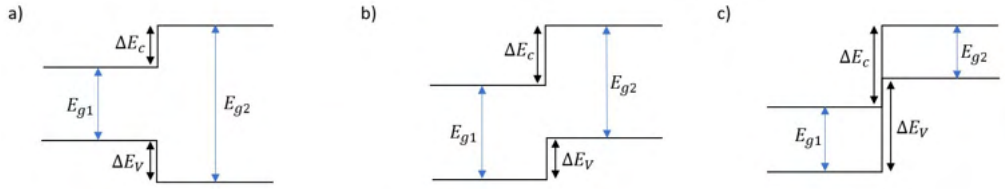

Figure 2.7: The three basic types of abrupt heterojunctions: a) nested, b) staggered and c) misaligned (band bending is neglected in this portrayal)

Abrupt heterojunctions are generally more resistive than graded ones, since the carriers have to overcome the additional "step"-barrier, but it is possible to convert abrupt junctions into graded junctions by appropriate doping if this resistance is undesired [77].

The other way of classification divides heterojunctions by the type of doping the materials in question have undergone. If the type of doping on both sides of the interface is the same, i.e. an *nn*- or a *pp*-heterojunction, the junction is called "isotype". When both sides are doped differently leading to a *pn*-heterojunction, it is called an "anisotype" junction. This leads to materials with isotype junctions being majority-carrier devices that act similar to M-S interfaces and anisotype junctions being minority-carrier devices acting similar to *pn*-homojunctions.

The exact way of charge transport across the interface of both isotype and anisotype heterojunctions has not been fully explained yet, but there have been a number of different approaches that generally focus around the theory of interface states (originated from "dangling bonds" from the lattice mismatch) being relevant for the recombination of charge carriers and the pinning of E_F, similar to the idea of metal-induced gap states in Schottky-barriers. It is also possible that in fact more than one of these approaches is actually true depending on the material combination used in the respective application [78]. To keep this concise, only one approach with only one case (*nn*-isotype and *pn*-anisotype with ($E_{gn} > E_{gp}$) will be discussed for both types in the following. Based on their general similarity to M-S junctions, isotype heterojunctions have been described by *Oldham and Milnes* [79] as a type of a "double Schottky" diode, with the interface acting like an interlaced metal monolayer for both of the semiconducting bulk sides as shown in Figure 2.8 a and the interface states acting as the "metal's" acceptor states. The materials on both sides will give off electrons to these states and when they reach equilibrium, two positively charged depletion regions are formed, which then lead to behaviour analogous to Schottky-barriers.

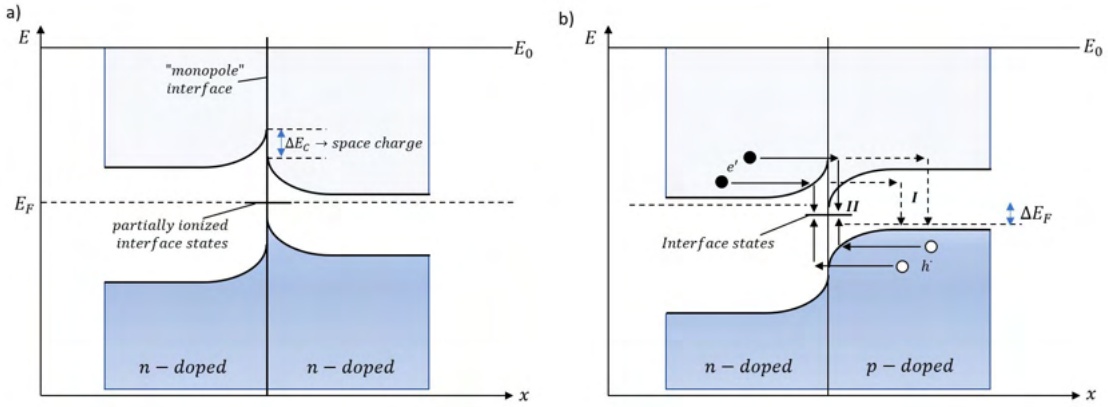

Figure 2.8: a) *nn*-isotype heterojunction: in equilibrium the interfacial "monolayer" is slightly negatively charged and the adjacent SCRs are accordingly positively charged; b) anisotype heterojunction: (I) minority carrier injection and recombination in the bulk (II) transport of e' and $h^{\bullet}$ to and recombination at the interface

At anisotype heterojunctions, the band-bending typically leads to the formation of a "spike" on the n-doped side and a "notch" on the p-doped side. The mechanism of charge transport proposed by *Donnelly and Milnes* [80] sees two different ways of charge transport. Group I describes minority carrier injection into the space charge region, followed by diffusion-recombination in the bulk of the narrow-gap material. Group II, which is supposed to be dominating, shows recombination at the interface, leading to the creation of interface states, which in turn pin the Fermi levels of both materials. ΔE_F corresponds to either the voltage that has to be applied for photoemission or vice versa the voltage generated by the junction upon photoabsorption. Both ways of charge transport can either happen by thermal emission over or tunnelling through the barrier holding back the minority carriers (Figure 2.8 b). With the recombination at the interface also being made up of three processes (transport of electrons, transport of holes, recombination) this results in a complex mechanism as any of the possible steps can be rate-limiting [78]. While analyzing the process may be disadvantageous compared to *pn*-homojunctions due to the complexity, the obvious upside of anisotype heterojunctions is that they allow a wider array of possible materials.

CdS for example shows good properties for photoluminescence or solar cell application if n-doped. But as it can not be p-doped, a CdS-homojunction is out of the question and these properties can only be brought into operation by using CdS in a heterojunction with a different p-type semiconductor [75, 78]. In solar cell technology, heterojunctions are quite common in III-V semiconductor junctions like GaInP/GaAs [81] or AlGaAs/GaAs [82] but they are also relevant for sulfides and oxides in either II-VI semiconductors [83] or perovskite semiconductors [84].

2.2 Metal oxide application in solar cells

The semiconducting properties of various binary and ternary metal oxides (MOs) based on their bandgap energies of $E_g \approx$ 2-4 eV have made them attractive for electronic applications for many years now. The versatility of their properties, together with their chemical stability and suitability for low-cost and scalable manufacturing, have provided them high importance in the field of next-generation photovoltaics (NGPV). Today, the most common research topics of MOs in PV applications are centered around the use of wide gap (>3.1 eV) MOs in transparent conducting oxides (TCOs), and the use of MOs as electron conducting (and sometimes hole-conducting [85]) layers between the light-absorbing material and the electrodes. The case of MOs actually being used as the light harvester in PV cells has received significantly less attention, with the most well-researched materials today being copper oxides like CuO and especially Cu_2O [12, 13, 86].

TCOs play an important role in solar cell technology, as virtually every solar cell needs at least one (semi-)transparent conductive electrode, being on one hand able to let photons into the light absorbing bulk layers and on the other hand provide transport for charge carriers. This means that the materials in question have to show high conductivity for electronic charges and simultaneously high transparency properties, that are contradictory in general. Nowadays, mostly n-type TCOs (meaning the majority carriers are electrons) are in use with tin-doped indium oxide ($Sn:In_2O_3$ or ITO) dominating the market since it reaches resistivities as low as $1\text{-}2{\cdot}10^{-4}\,\Omega$cm. SnO_2 and ZnO show a comparably good metal-oxide orbital overlap and have thus also experienced notable application with the advantage of the much higher abundance of Sn and Zn compared to In [87]. In the fabrication process of PV cells containing thin film layers, TCOs are often used as the substrate material on which the planar or nanostructured films are grown.

Said films are used as transport layers for charge carriers between the photon absorbing species and the electrode in organic, dye-sensitized, or (especially) halide perovskite solar cells. While the absorbing layer (AL) in these types of cells generally already shows high conductivity and good efficiency on its own, the advantages of coupling the charge transport with MOs mainly lie in the field of stability. MOs have shown to not only provide thermal and humidity protection to the AL, but in the case of halide perovskites also increase the stability of the structure [88]. Together with MOs tending to be more cost efficient and easy to fabricate compared to the respective AL, while still providing comparably high carrier conductivity, it is reasonable to use them as a transport layer. This role is most often fulfilled by (mesoporous) anatase TiO_2 in halide perovskite cells but ternary oxides like $SrTiO_3$ reach similar efficiencies, which has been attributed to the similar energy levels of the two compounds [89].

The final main use of MOs in PV application with MOs as the actual AL being responsible for not only the transport but also the generation of charge carriers is known as an all-oxide PV cell. As stated before, mainly binary oxides like cuprous (Cu-O) or sometimes ferric oxides (Fe-O) have been described in literature, with the *p*-type semiconductor Cu_2O being the most notable. Although there have been attempts made at *n*-doping Cu_2O to use it in a homojunction, this has proven difficult and not very efficient even if accomplished, resulting in efficiencies of no more than 2,05 % and maximum open-circuit voltages (U_{OC}) of about 0.5 V [90]. Other attempts including Schottky-junctions with metal electrodes and heterojunctions with different binary and ternary oxides have resulted in a U_{OC} of 0.6 V for Schottky-junctions [86], 0.81 V for ternary oxides (achieved with a $Cu_2O/ZnGa_2O_4$ junction) and a full 1.2 V for binary oxides in a junction with PLD-grown Ga_2O_3, all operating at room temperature [87].

The application of oxidic perovskites (as opposed to methylammonium halide perovskites which are commonly meant when talking about "perovskite solar cells") as absorption layer in solar cells was originally mainly restricted to the generation of photovoltage from domain boundaries of ferroelectric compounds like $BaTiO_3$ or $Pb(Zr,Ti)O_3$ (PZT). With $\approx$ 10 mV to be generated from each domain boundary, this would result in a U_{OC} of well over 15 V, but this is contrasted by small current densities resulting in a general power-conversion efficiency of <1%. The usage of ferroelectric materials with narrow bandgaps (<3 eV) like $BiFeO_3$ (BFO) has shown a U_{OC} of about 0.9 V with a conversion efficiency of nearly 10% (again at room temperature) although this was attributed by the authors to a possible formation of a Schottky-like junction at the BFO/ITO interface with ferroelectric effects only playing a minor role [91]. The idea of oxide-oxide interface depletion layers leading to the generation of photovoltage and photocurrent is thus an interesting one and constitutes the basis for the work at hand, with $SrTiO_3$ acting as the main AL. Following the works of Brunauer *et al.* [19] and Morgenbesser *et al.* [20], other perovskitic oxides likes $(La,Sr)CrO_3$ and $(La,Sr)MnO_3$ are used in combination with STO to form the junctions needed for generating photovoltage. These materials will be discussed in more detail in the following sections 2.3-2.5.

2.3 Strontium titanate (STO)

Strontium titanate, as the name suggests, is a chemical compound of strontium from the group of titanates with the empirical formula $SrTiO_{3-\delta}$.

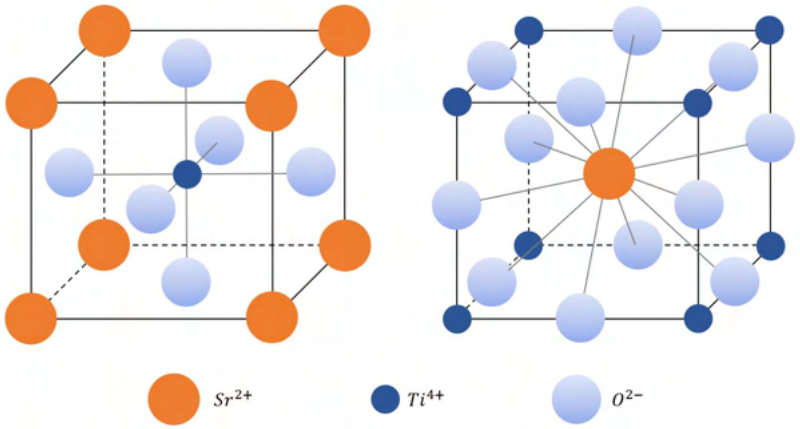

Figure 2.9: The conventional cell of strontium titanate showing the 6-fold coordination of Ti^{4+} (lhs) and the 12-fold coordination of Sr^{2+} (rhs)

STO is an oxide with - at room temperature - a cubic centrosymmetric perovskite structure shown in Figure 2.9 although below 105 K it takes on a tetragonal modification in what is known as an antiferrodistortive phase transition. Here, the central TiO_6-octahedron takes a slight turn around the c-axis with respectively adjacent octahedrons showing an opposing direction of rotation. This distortion leads to the formation of a tetrahedral superstructure in the [001]-direction [92]. However this is in reality a rather small change in the overall lattice, since the rotational angle φ never exceeds a value of 2.1°. This results in a ratio of the lattice constants of the formally cubic cell of c/a = 1.0004. Moreover, the total volume of the cell remains nearly constant, as the tilting of the octahedrons leads to a volume contraction which counteracts the increase of the lattice parameter c [93]. Other interesting properties of STO in the cryogenic regime include the lack of a ferroelectric phase at low temperatures even though STO has a hypothetical Curie-temperature (T_C) of about 35-40K. Instead, due to quantum-mechanical stabilization, the material's paraelectric phase remains stable, making STO a so-called quantum-paraelectric. The ferroelectrical phase is, however, merely suppressed and can be stabilized in a number of different ways including slight doping with Ca (0,002-0,02%), which also leads to dilute superconductivity of the compound below 0,5 K. All of these phenomena are also closely related to the permittivity ε of STO, which does not diverge when approaching 0 K but instead becomes stable at a value of the order of 10^4 [94]. At room temperature, the permittivity is relatively high with a value of ca. 300, which slowly declines at higher temperatures reaching from around 200 at 500 K to 120 at 800 K [95]. While photoluminescence has been reported for STO in the blue and green regime at low temperatures (below 150 K) [96], it is generally encountered as an achromatic, transparent compound which is in line with it's (indirect) bandgap of 3,25 eV, making it a semiconducting material. Impurities change the colour of STO, with Fe-doping giving it a brownish tint and Nb-doped STO being completely black. This colour change can also be seen in its natural counterpart tausonite which is described as red-brown to dark gray [97]. Synthetic crystals of STO are typically grown using either a direct version of the Verneuil-process, adding a mixed powder of $SrCO_3$ and TiO_2 to the flame [98] or a modified, indirect version by first creating a titanyl double oxalate ($SrTiO(C_2O_4)_2$) feed powder from $SrCl_2$, $TiCl_4$ and oxalic acid, which is then fed to the flame [99].

2.3.1 Defect chemistry in STO

The defect chemistry in STO and the subsequent contribution thereof to its electrical properties is well understood, which has earned STO the label of "a model electroceramic" [100]. The main contribution to intrinsic defect formation is of course the material's oxygen nonstoichiometry, leading to the creation of charge carriers in the form of oxygen vacancies $V_O^{\bullet\bullet}$, electrons e' and holes $h^{\bullet}$ upon oxygen atoms being incorporated into or removed from the bulk (see Equations (2.10) through (2.16) in Section 2.1.2).
With the closed-packed character of the structure, the presence of any kind of interstitial atoms seems implausible, which still leaves the possibility of a partial Schottky-type reaction, shown in Equation (2.27) as fundamental for the intrinsic defect chemistry of STO. The SrO-phase created through this reaction can actually be found in the form of so-called Ruddlesden-Popper phases enriched at grain boundaries and possibly acting as a sink and source for Sr-ions [101]. This is, however, only relevant in the initial preparation of STO, as the mobility for Sr-ions below 1500 K is too small for them to make a dynamic contribution to the defect chemistry; their concentration is thus frozen-in [100].

$$Sr_{Sr}^{\times} + O_O^{\times} \rightleftharpoons V_{Sr}'' + V_O^{\bullet\bullet} + SrO \tag{2.27}$$

Stepping down a bit and looking at the intermediate temperature regime (T = 750 K), we find the kinetics of oxygen incorporation (and further oxidation of the oxide) to be the dominating process, which follows the reaction equation

$$\frac{1}{2}O_{2(g)} + V_O^{\bullet\bullet} \rightleftharpoons O_O^{\times} + 2\,h^{\bullet} \tag{2.28}$$

creating two electron holes upon filling up one vacancy. One can easily see that this is just a combination of Equation (2.10) with

$$nil \rightleftharpoons e' + h^{\bullet} \tag{2.29}$$

showing that the respective mass action laws are coupled by band-gap excitation process leading to generation or annihilation of electrons and holes. This excitation of electronic carriers can be viewed analogous to the formation of a Frenkel-pair (Equation (2.6)) in the valence and conduction band [39] with the corresponding mass action law

$$K_e = [e'][h^{\bullet}] = K_e^o e^{\frac{-E_g}{k_b T}} \tag{2.30}$$

Here, $K_e^o = N_V N_C$ is the product of the temperature-dependent weighted density of states (DOS) in the conduction (N_C) and valence band (N_V). Comparing Equation (2.30) to (2.11) and the theoretical analogon for the oxidation reaction (2.28), it can also be further seen that $K_{Ox} \cdot K_{Red} = K_e^2$ and thus $\Delta H_{Ox} + \Delta H_{Red} = 2E_g$ [102].
Lowering the temperature even further (T < 670 K) the concentration of oxygen also starts becoming frozen in and only electronic carriers remain as the main means of charge transport across the compound. With vacancies being immobile and electrons and holes being mobile, it is possible for the vacancies to get ionized through "trapping" of free electrons (or holes) according to Equations (2.31) and (2.32), leading to a decrease in the content of free charge carriers [103].

$$V_O^{\bullet\bullet} + 2\,e' \rightleftharpoons V_O^{\bullet} + e' \rightleftharpoons V_O^{\times} \tag{2.31}$$

$$V_M'' + 2\,h^{\bullet} \rightleftharpoons V_M' + h^{\bullet} \rightleftharpoons V_M^{\times} \tag{2.32}$$

Lastly we have to consider the role of impurities and dopants in the material, which can also tremendously change the electronically conducting properties of STO. This is mostly owed to the perovskite structure ABO_3 of the material, which is able to accommodate a large number of dopants on both the A- and B-site even up to concentrations in the range of percents as long as the Goldschmidt-criterion (Equation (2.33)) for the ratio of the radii on the A-site (r_A) and the B-site (r_B) is fulfilled. While acceptor-doping of STO, e.g. with Fe^{3+} on the Ti^{4+}-site, can be balanced by the compound with relative ease through the formation of oxygen vacancies, donor doping would require oxygen interstitials for charge neutrality which can obviously not be realized as said beforehand. Thus, charge neutrality is partly preserved by cation vacancies with low mobility, making these compounds often not fully equilibrated [104].

$$\frac{r_A + r_O}{\sqrt{2}(r_B + r_O)} \approx 1 \tag{2.33}$$

The substitution of Ti through Fe in Fe-doped STO can now either introduce holes or oxygen vacancies (p-type dopant), whereby vacancy formation typically predominates the process. This is, however, dependent on temperature and oxygen partial pressure, which are both able to shift the equilibrium relation of three-valent and four-valent iron given by Equation (2.34). At low temperature and high $p(O_2)$, where oxygen vacancies get "filled up" and hole conductivity prevails, iron is typically found as Fe^{4+} ($Fe^{\times}_{Ti}$). At lower partial pressures, the conductivity is controlled by oxygen vacancies and iron is present as Fe^{3+} (Fe'_{Ti}), corresponding to undoped STO under strongly reducing conditions, where Ti is only present as Ti^{3+}. It should be noted that although undoped STO in reducing atmosphere has a high number of excess electrons in the conduction band, compensating for $V^{\bullet\bullet}_O$ and thus making it an n-type conductor, the use of an acceptor dopant like Fe still instills p-conducting properties into the material [104].

$$Fe'_{Ti} + h^{\bullet} \rightleftharpoons Fe^{\times}_{Ti} \tag{2.34}$$

This relation is complicated further by electrostatic attraction between Fe'_{Ti} and $V^{\bullet\bullet}_O$, which leads to a significant amount of oxygen vacancies becoming trapped around Fe^{3+} doping sites and thus drastically decreasing the vacancy conductivity. This is although only present in the low-temperature regime and these associates completely dissociate at temperatures above ca. 570 K [100, 104].

Another form of complication arises from the proposed possibility of amphoteric behaviour of Fe-ions, which could also occupy the A-site in the perovskite by taking a two-valent form Fe^{2+}, as has been reported for Mn-doping [105]. Positron-annihilation lifetime spectroscopy (PALS) measurements together with X-ray absorption spectroscopy (XAS) on Fe:STO thin films have shown that Fe also tends to occupy the A-site, being present as both Fe^{2+} and Fe^{3+} independent of oxygen partial pressure [106]. This "antisite defect"-behaviour of iron would thus lead to donor properties. Together with intrinsic Ti_{Sr} antisite defects and a buffer-like equilibrium of Sr-vacancies (V''_{Sr}/V'_{Sr}) this has been suspected by Morgenbesser *et al.* [32] to be the reason for strong Fermi-level pinning in Fe:STO thin films, resulting in "pseudo-intrinsic" behaviour of the conductivity instead of p-type conductivity.

2.3.2 Generation of voltage under UV light

The precise mechanism of how voltage is generated in STO or at STO-interfaces upon UV illumination at elevated temperatures has, to the best of the author's knowledge, not yet been fully explained as of the completion of this work. There have, however, been possible explanations that focus around the idea of there actually being two main contributions to current and voltage: a purely photovoltaic one (PV) and an electrochemical one (EC).

Photovoltage U_{PV}

The photovoltaic part of the total voltage has mainly been attributed to the build-up of highly resistive space charge layers at the interfaces of STO with various electrode materials, which collapse under illumination. It has although never been described as a pn-junction (since two materials are present), but rather a Schottky-like [18, 19] junction or a heterojunction [20], depending on the electrode material used. Applying only a current collector grid or a sputtered metal electrode (thin enough for the light to reach STO) should result in a classical M/S-junction with the expectable electrostatic potential step at the interface. Illumination leads to the creation of electronic charge carriers and together with diffusion in the material creates a potential difference between the working and counter electrode almost instantly. Due to the p-type conductivity of nominally undoped (due to impurities) and acceptor-doped STO, the polarity on the metal is expected to be negative. Quantification of the expected voltage is, however, difficult as oxygen vacancies play a major role in the general defect chemistry of STO and may disturb the equilibrium of electronic charge carriers generated through illumination. Enhanced uptake of oxygen through UV light at elevated temperatures, as reported by Merkle *et al.* [16], and a following decrease in vacancy concentration may thus be detrimental to the photovoltage.
In the case of S/S-heterojunctions, the potential step responsible for space charges and photovoltage is suspected to be a consequence of the Fermi-level difference of the materials in question [20], which is in line with the explanation of anisotype heterojunctions presented in Section 2.1.4.

Battery voltage U_{bat}

Unlike the emerging of photovoltage for which a specialized interface is required, the battery voltage has been attributed to the intrinsic affinity of STO to incorporate oxygen into the bulk upon UV light illumination by Walch *et al.* [18]. It is described that carrier generation in the material according to Equation (2.35) significantly changes the concentration of electrons in the nominally hole-conducting STO. This leads to a reduction of ambient oxygen at the STO surface, since the participation of CB electrons catalyzes the rate limiting step of the respective reaction, effectively making STO an electrolyte for O^{2-}-ions. This Nernstian behaviour now for one happens on a larger timescale than the photovoltage (as oxygen has to be incorporated over time to "charge" the material) and also shows opposing polarity as electrons are now subtracted from the working electrode.

$$nil + h\nu \rightleftharpoons e'_{CB} + h^{\bullet}_{VB} \tag{2.35}$$

The complete model, shown in Figure 2.10, thus shows an immediate "jump" of the voltage to $U_{PV,max}$ upon UV illumination, which is then reduced by the build-up of U_{bat} and its own decrease following the stoichiometry change. Switching the light off again instantly collapses the photovoltage and only $U_{bat,max}$ remains, which then starts to slowly decline as the oxygen is removed again. If both photovoltaic and electrochemical battery voltage are similarly strong, this results in a very low total voltage.

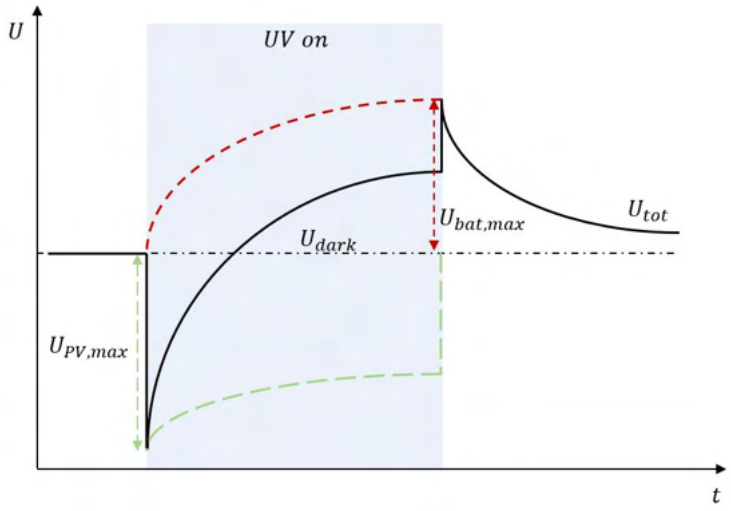

Figure 2.10: Time/Voltage graph depicting the expected course of total voltage U_{tot} with contributions of U_{PV} (green) and U_{bat} (red)

2.3.3 Self-enhancement effect of photocurrent

The self enhancing effect of the STO's photocurrent has only recently been discovered [20] and will be further investigated during the course of this work. It was found that STO single crystals with an LSCr working electrode in short-circuit chronoamperometry show constantly increasing current, which could be divided into three sections: 1) An initial set-off of about 2 μA, followed by 2) a strong increase for ca. 1000 s up to 0.2 mA and finally 3) a seemingly linear, albeit slower long-time increase of the total current, which did not show any signs of stopping even after 17 h of illumination, as shown in Figure 2.11.

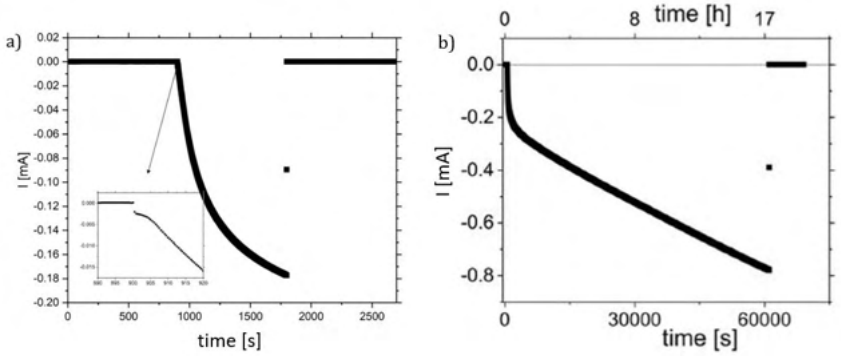

Figure 2.11: Self-enhancing photocurrent of the sample during UV-illumination (modified following [20]); a) General idea of the steadily rising current with small offset at the beginning and b) long time measurement for 17 h

This was speculated by the authors to be a result of stoichiometry polarization, where the internally generated photovoltage of about 1 V dropped not only at the external load but also at the internal resistance of STO. With ions being blocked at one or both electrodes this leads to a oxygen vacancy depletion at the positive electrode and a respective accumulation at the negative one, which is generally associated with resistance degradation and thus higher currents.

2.4 Strontium-doped lanthanum chromite (LSCr)

Lanthanum chromite ($LaCrO_3$/LCrO) is, like STO, a perovskite oxide material with the general formula ABO_3, but unlike STO, in $LaCrO_3$ both the A- and B-metal ion have a formal valence of +III (3:3 perovskite) and the general structure shows an orthorhombic distortion, which changes to a rhombohedral distortion when heated above 280 °C [107]. It is, like STO, an intrinsic p-conducting material, although its conducting properties are almost entirely electronical with the ionic rail being severely inhibited: up to 1250 K the ionic contribution to charge transport never exceeds 0.05% [108]. Both the rhombohedral distortion and the p-type conductivity of the compound can be promoted by doping $LaCrO_3$ with alkaline earth metals with Ca^{2+} and Sr^{2+} being by far the most favoured choices (through the introduction of CaO and SrO, respectively). Doping is generally done at already high levels of $0.10 \leq x \leq 0.25$ in an $La_{1-x}R_xCrO_3$ system, but there have also been reports of 40% Sr- and 30% Ca-substitution [109]. The increase in conductivity is universally attributed to an increase in holes following the substitution of La^{3+} (Equation (2.36)) and the subsequent formation of Cr^{4+} ions to preserve charge neutrality leading to a small polaron hopping mechanism between Cr^{3+} and Cr^{4+} [107, 109, 110].

$$SrO \longrightarrow Sr'_{La} + h^{\bullet} \tag{2.36}$$

The conductivity is further dependent on oxygen partial pressure, as with decreasing $p(O_2)$ the compound begins excorporating oxygen from the bulk ($(La,Sr)CrO_{3-\delta}$), leading to the creation of oxygen vacancies. This in turn heavily impedes the formation of holes, since charge neutrality in the Cr^{3+}/Cr^{4+}-equilibrium is now preserved automatically (Equation (2.37)). With oxygen vacancies being highly immobile and, as stated before, having close to no contribution to charge transport, the conductivity strongly decreases under reducing conditions [109].

$$O_O^{\times} + 2\,Cr_{Cr}^{\bullet} \rightleftharpoons \frac{1}{2}O_2 + V_O^{\bullet\bullet} + 2\,Cr_{Cr}^{\times} \tag{2.37}$$

Although there have been reports of LSCr being used in catalysis [111], its electrical properties are still the main interest of most research, including interconnection in SOFC technology [109] and recently semitransparent electrodes in solar cell technology [19, 20].

2.4.1 Interaction with STO

One of the earliest published studies showing interaction between LSCr and STO dates back to 1981 and describes small photocurrents that are induced in $LaCrO_3/SrTiO_3$-single crystals by visible light. This is however not done by bringing these materials in contact but actually by doping STO with La and Cr, thus creating a solid solution of $LaCrO_3$ in $SrTiO_3$ [112]. Further interest in the combination of these materials focused on their stability and the reliability of their conductivity at high temperatures [113]. Bringing photoactivity and high-temperature conductivity together, both materials seem predestined for application in high-temperature solar cell technology.

While the LSCr/STO-junction has already proven to show stable photovoltage of ≈ 1 V, only recently a theoretical study on the materials' synergy was published [114]. Calculating activation energies for defect formation, it was found that unsurprisingly "Schottky"-type defects are the most favourable type of intrinsic defect for both materials. However it was also found that the formation of oxygen Frenkel defects is strongly favoured around the interface when compared to the bulk, offering the possibility of oxygen ion migration at the interface, which is especially interesting considering the otherwise nearly inexistent defect mobility in LCrO/LSCr.
With both materials being *p*-type conductors and the junction having been described as Schottky-like, this hints at the existence of a *pp*-isotype heterojunction at the interface.

2.5 Strontium-doped lanthanum manganite (LSM)

Lanthanum manganite ($LaMnO_3$/LMO) is generally a compound that is very similar to lanthanum chromite, with both being (3:3)-perovskites with an orthorhombic lattice distortion and antiferromagnetic behaviour at standard conditions and both being often doped with alkaline earth metals to introduce a +III/+IV equilibrium on the B-site. So, just like $LaCrO_3$ is typically encountered as (La,Sr)CrO_3, $LaMnO_3$ is mostly applied in the form of (La,Sr)MnO_3 (LSM). Unlike its chromite counterpart, LMO shows significant amounts of La-vacancies even at room temperature, resulting in a relative surplus of oxygen ($LaMnO_{3+\delta}$) for one, but also already introducing Mn^{4+} states to preserve charge neutrality in the undoped compound, leading to Jahn-Teller distortion of the MnO_6 octahedron. These Mn^{4+} states, however, represent deep trapped holes with little to no mobility, which thus do not notably contribute to an increase in conductivity.
Doping with Sr reduces the concentration of La-vacancies and also promotes the generation of holes with higher mobility according to Equation (2.36), leading to an overall increase in conductivity. Doping also strongly influences the structural and magnetic properties of the material, which can show an orthorhombic, cubic or hexagonal/rhombohedral lattice as well as para- and ferromagnetism (in a "half-metal" state [115]) with varying Curie-temperatures (T_C) all depending on the x in $La_{1-x}Sr_xMnO_3$ [116].
These highly tunable electrical, magnetic and structural properties together with the compounds' stability at high temperatures have made LSM a popular material for research on SOFCs [117], catalysis [118, 119], gas sensors [120] and also solar cells [20]. In this work, its application was mainly chosen because of its general similarity to LSCr and the relative ease of using it in PLD-processes to create thin film electrodes, requiring considerably lower temperatures than LSCr, as shown in Table 3.2 (see Section 3.1).

2.6 Electrochemical Impedance Spectroscopy (EIS)

Impedance spectroscopy has today become one of the most powerful tools for analysis and characterization in electrochemistry and solid state ionics. The ability to identify individual contributions to a full electrochemical process or system in a non-destructive way has proven highly useful and together with the relative simplicity of the method in terms of instrumentation, EIS allows for a broad spectrum of applications ranging from the characterization of corrosion mechanisms over clarification of reaction kinetics to identification of unknown species present during the process of interest. The most notable downside of the method is, however, the rather tenuous visualization of data, making the interpretation of measurements comparatively demanding. Impedance spectroscopy in general is a highly complex topic and only basic aspects of the method for applications in solid state ionics will be discussed here.

2.6.1 Principle of EIS

As stated before, one of the main advantages of EIS over conventional two-point DC measurements is the ability to separate individual contributions to the total conductivity (or resistivity) of an EC system instead of measuring averages. This is achieved by frequency-dependent measurements of the system's impedance, i.e. its opposition to alternating current. In alternating current, voltage and current are not constant anymore but instead are time-dependent and follow a sinusoidal behaviour, which is described in Equations (2.38) and (2.39) with U_0 and I_0 denoting the respective amplitude and ω and φ describing angular frequency and phase shift. Ohm's law (Equation (2.40)) is thus not sufficient anymore in describing the system's resistance R, which is therefore replaced by the impedance Z.

$$U(\omega, t) = U_0 \cdot e^{i\omega t} \tag{2.38}$$

$$I(\omega, t) = I_0 \cdot e^{i(\omega t - \varphi)} \tag{2.39}$$

$$R = \frac{U}{I} \tag{2.40}$$

The impedance $Z(\omega)$ can be expressed in the form of Equation (2.41) with Z_0 denoting the ratio of the amplitudes of voltage and current, respectively. We can now see that it is possible to describe the impedance in a modified version of Ohm's law, that is composed of the general resistance and the reactance, an exponential factor revolving around the phase shift φ. Using Euler's identity, one can easily see that the impedance can be written in the form of a complex number, consisting of a real and an imaginary part, as shown in Equation (2.42).

$$Z(\omega) = \frac{U(\omega, t)}{I(\omega, t)} = \frac{U_0 \cdot e^{i\omega t}}{I_0 \cdot e^{i(\omega t - \varphi)}} = Z_0 \cdot e^{i\varphi} \tag{2.41}$$

$$Z(\omega) = Z_0 \cdot e^{i\varphi} = Z_0(cos(\varphi) + i \cdot sin(\varphi)) \tag{2.42}$$

This expression can be simplified for idealized circuit elements with constant phase shifts. Current flowing through an ideal resistor shows no phase shift, thus simplifying the expression in Equation (2.41) to that of a simple and frequency independent resistance R, given by Equation (2.43). When considering the other extreme case with the phase shift reaching its maximum value at 90 °, the real part of Equation (2.42) reaches 0 and only the imaginary part is of relevance. Here, two cases can be discerned: If φ is at -90 °, the current *leads* the voltage by $\frac{\pi}{2}$, leading to an ideal capacitor's behaviour as expressed in Equation (2.44). At +90 °, the current *lags* the voltage which leads to an ideal inductor given by Equation (2.45).

$$Z_R(\omega) = R \tag{2.43}$$

$$Z_C(\omega) = \frac{1}{i \cdot \omega \cdot C} \tag{2.44}$$

$$Z_L(\omega) = i \cdot \omega \cdot L \tag{2.45}$$

When connecting two of these basic circuit elements in series, the total resulting impedance Z_{1-2} can simply be calculated through Equation (2.46). The case of parallel connections $Z_{1\|2}$ is given by Equation (2.47), which is often used to describe real, homogeneous materials. This stems from the idea that these materials exhibit ohmic and capacitive behaviour, making it reasonable to describe them as a parallel RC-feature, as shown via Equation (2.48) [121]. More complex materials can be described through various combinations of serial and parallel features creating an equivalent circuit model.

$$Z_{1-2} = Z_1 + Z_2 \tag{2.46}$$

$$Z_{1\|2} = \left(\frac{1}{Z_1} + \frac{1}{Z_2}\right)^{-1} \tag{2.47}$$

$$Z_{RC} = \left(\frac{1}{Z_R} + \frac{1}{Z_C}\right)^{-1} = \frac{R}{1 + i\omega RC} \tag{2.48}$$

Lastly, it is common that real systems do not exactly behave like ideal circuit elements and the angular phase shift is not always at either 0 or 90 °. To account for said cases, constant phase elements (CPE) are used to describe non-ideal capacitors, using two parameters p and T. The impedance of a CPE is given by Equation (2.49), where p describes the non-ideality in a range of 0 to 1 and T corresponds to the capacitance C. Looking at Equation (2.50), which describes the effective capacitance of a CPE, one can derive that a p-value of 0 describes an ideal resistor, while a value of 1 describes an ideal capacitor with the capacitance T [122].

$$Z_{CPE} = \frac{1}{(i\omega)^p \cdot T} \tag{2.49}$$

$$C_{eff} = \left(R^{1-p} \cdot T\right)^{1/p} \tag{2.50}$$

2.6.2 Visualization and analysis of EIS

The two most common ways of visualizing impedance spectra are Bode plots and Nyquist plots, which contain the same information, but emphasize different aspects. The Bode diagram consists of two curves and plots the absolute value of the impedance $|Z|$ (sometimes referred to as "magnitude") and the phase shift φ on the y-axis against the AC frequency ω on the x-axis in a logarithmic depiction. These types of plots are of little importance compared to Nyquist diagrams for the work at hand and will not be elaborated further.

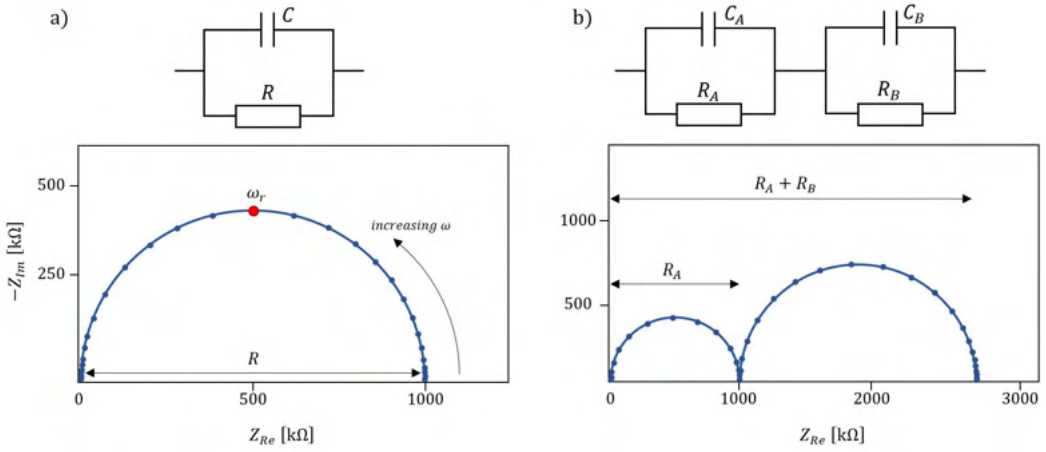

Figure 2.12: Nyquist plots and corresponding equivalent circuit models of a) one RC feature and b) two RC features in serial connection

The Nyquist diagram plots data according to Equation (2.42) in the form of a complex impedance plane, with the real part on the x-axis (denoted as Z_{Re} or Z') and the (negative) imaginary part on the y-axis (Z_{Im} or Z''). Measurements are typically performed from high to low frequency ranges (MHz $\longrightarrow$ mHz), which corresponds to the plotting in Nyquist diagrams, where an increase on the real axis shows a decrease in frequency. In these types of plots, ideal circuit elements take very distinct shapes, making it relatively easy to identify them. While an ideal resistor would just appear as a discrete point on the real axis, an ideal capacitor would look like a straight line on the imaginary axis. Thus, an ideal RC-feature appears as a perfect semicircle in the diagram, with its diameter corresponding to its resistance, as depicted in Figure 2.12 (a) [123]. At high frequencies, Z_C becomes small (see Equation (2.44)) and the current is mostly transported via the capacitor, while at low frequencies, the resistive path is favoured as the frequency dependency becomes negligibly small. The semicircular form can therefore be explained as a vertical capacitive feature, that gets "bent" down with decreasing frequency while the resistor gains the upper hand. The frequency ω at which the currents via resistor and capacitor are equal, has to be logically in the middle of the semicircle where the imaginary part reaches its maximum. This is known as the relaxation frequency (or *characteristic frequency*) ω_r of an RC feature and is given by

$$\omega_r = \frac{1}{RC} \tag{2.51}$$

This is also the main parameter that allows distinct separation of serial RC features and thus makes it possible to attribute conductivity contributions to the total conductivity of a material to the respective species. Features with very similar relaxation frequencies typically "merge" together and can not be separated clearly from each other.

To correctly attribute a feature to the source of its contribution (i.e. bulk vs grain boundary), some further considerations have to be taken. Both the resistance and the capacitance of a species are dependent on an intrinsic material parameter and the material's geometry, as shown in Equations (2.52) and (2.53), with d and A denoting thickness and area of the species, σ_i its specific conductivity and ε_i its relative permittivity. Combining these with Equation (2.51) we find through Equation (2.54) that the relaxation frequency is independent of geometry and is also an intrinsic and specific parameter, which is high for elements with high conductivity and low for elements with high permittivity [39].

$$R_i = \frac{1}{\sigma_i} \cdot \frac{d}{A} \tag{2.52}$$

$$C_i = \varepsilon_i \cdot \frac{A}{d} \tag{2.53}$$

$$\omega_{r,i} = \frac{\sigma_i}{\varepsilon_i} \tag{2.54}$$

To identify a feature, it is thus necessary to either know the respective conductivities and permittivities or to calculate them from e.g. Equations (2.52) and (2.53). Vice versa, it is of course possible to derive geometrical parameters, like the thickness of space charge regions from these measurements, if the other parameters are already known [122]. In some cases, it is also possible to derive the source of a feature from a variation in scaling, e.g. the geometrical capacitance would change after a change in volume, while chemical capacitance would not.
In real experimental studies, this can often become very complicated and lead to a number of assumptions and deliberations and the necessity to operate by exclusion principle to be able to correctly derive the nature of each individual feature.

2.7 Pulsed Laser Deposition (PLD)

Today, vapor deposition methods are a standard tool for the growth of thin films. They are commonly divided into physical (PVD) and chemical (CVD) vapour deposition methods. The general difference between the two consists in the way the film is brought onto the surface. While in CVD processes, volatile precursors are introduced into the gas phase, which adsorb on the substrate's surface, where they react and thus form the desired material, in PVD processes, the desired material is already present in a condensed phase, but is then brought into the gas phase through a physical process and finally recondenses at the substrate's surface [124]. Pulsed Laser Deposition (PLD) is among the most used PVD methods and considered the most effective technique for the growth of crystalline oxides [28]. The setup consists of a vacuum chamber in which the condensed phase (the "target") and the substrate are placed as depicted in Figure 2.13. Through a window in the chamber, a pulsed laser beam strikes the target to ablate material into the gas phase. At high laser fluences, the vaporization is no longer dependent on the vapor pressures of the ionic species, allowing stoichiometric ablation and recondensation of the target material [124]. To ensure an evenly distributed erosion of the target, the target holder is rotating and placed in a way that the laser preferably does not strike the center of the target. During the course of this work, a KrF-laser was used to grow STO, LSCr and LSM thin films on different substrates.
To achieve proper films suited for the desired application, it is also necessary to control the temperature and atmosphere inside the chamber. Adjustment of oxygen partial pressure makes it possible to regulate the oxygen (non-)stoichiometry within the films and govern the morphology of films, while heating of the sample holder also mainly contributes to film morphology.

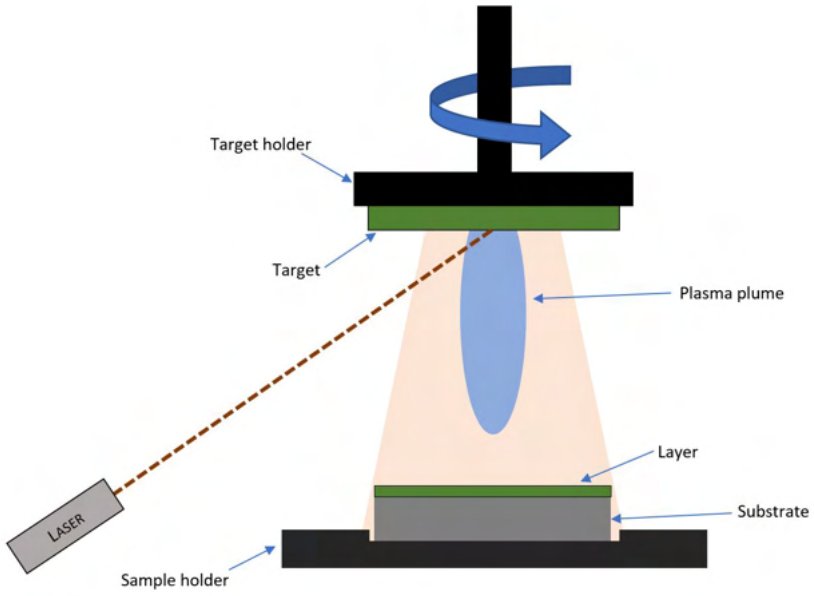

Figure 2.13: PLD operational principle; the general construction can also be upside down with the substrate being placed above the target

3 Experimental

3.1 Sample preparation

3.1.1 STO thin film samples (TF)

The main goal of the investigation of $SrTiO_{3-\delta}$ thin film based PV cells were the effects of cation non-stoichiometry on photovoltages. Thus a variety of samples was prepared in generally the same fashion but with different dopings and compensations in the STO electrolyte materials. All samples were created via PLD, using a one-side polished YSZ 10x10x0.5 mm single crystal from CrysTek Germany as a substrate with the electrolyte material as well as the electrode materials (LSCr, LSM) all being deposited on the polished side of the substrate (see Figure 3.1). Additionally, samples with symmetrical electrodes (LSCr/LSCr and LSM/LSM) were prepared for reference.

Table 3.1 shows every combination of doping and compensation used as the STO ablation targets in this test series by having the respective slot marked with the sample's respective denotation. For example, the sample with an Sr-compensation of 5% and an Fe-doping of 2% has a chemical formula of $Sr_{1.05}Ti_{0.98}Fe_{0.02}O_{3-\delta}$ and will be referred to as "STO 5/2". Samples without iron doping will just be named "STO 5" or "STO 10". This nomenclature refers to the chemical composition of the targets used for PLD and may be quite different from the compositions of the resulting thin films.

Table 3.1: Overview on STO combinations used for thin films

Fe-doping [%]	Sr-compensation [%]				
	0	3	5	7	10
0	0		5	7	10
2	0/2	3/2	5/2	7/2	
5			5/5		

All targets including the ones for the electrode materials have been prepared beforehand with the exception of STO 7, which was prepared during this work from $SrCO_3$ and TiO_2 by grinding them together in EtOH, evaporating the solvent, pressing the powder in a uniaxial press at 6 kN and sintering the pellet for 5 h at 1250 °C. The so produced $SrTiO_3$ was again grinded up, pressed at 6 kN and sintered for 12 h at 1350 °C under reducing H_2-atmosphere. The preparation of every other STO target was done in the same fashion, while the LSCr- and LSM-targets were prepared using Pechini's method.

The parameters for the PLD process can be seen in Table 3.2. The Target-sample distance was 6 cm in all instances and the energy of the laser was set to 380 mJ, which corresponds to ca. 90 mJ inside the chamber. The thickness of the film shown in Table 3.2 is the desired thickness and may not fully represent the actual thickness of the thin film on the samples. Since the different variations of STO shown in Table 3.1 were assumed to behave similar to each other in terms of layer growth under PLD conditions, the parameters were kept the same for every material and are generally denoted as "STO".

Table 3.2: PLD Parameters for every material

Material	Temperature (°C)	Pressure (mbar)	Pulses	Frequency (Hz)	Thickness (nm)
STO	650	$1.5 \cdot 10^{-1}$	54 000	10	650
LSCr	700	$1.5 \cdot 10^{-2}$	4 500	5	100
LSM	550	$4 \cdot 10^{-2}$	9 000	5	200

Additionally, one sample (STO 7/2) was prepared with a Pt current collector grid on top of the electrodes with a thickness of 100 nm, a strip width of 15 μm and a mesh size of 35 μm. This was done in two steps using lift-off photolithography and magnetron sputtering. For lithography, the sample was coated with a photoresist (N-1430 MicroResist Technology) using a spin coater (SCC-200 KLM). The polymer on the sample was dried and subsequently cross-linked using UV light, before bathing the sample in developer solution and rinsing it with distilled water. In a second step, additional photoresist was added with a brush to the regions on the sample that were not covered with electrode material to avoid short circuits across the collector grid. This was again dried and cross-linked. The parameters for lithography and sputtering can be found in Table 3.3. Figure 3.1 schematically shows a cross-section of the general structure of the thin film samples.

Table 3.3: Parameters for application of collector grids on thin film samples

Photolithography		Sputtering	
photoresist	100 μl	material	Platinum
spincoater speed	75 rps	sputter time	162 s
drying	2 min at 106 °C	Ar pressure	$2 \cdot 10^{-2}$ mbar
UV exposure time	60 s	sputter current	100 mA
developing time	60 s	thickness	100 nm

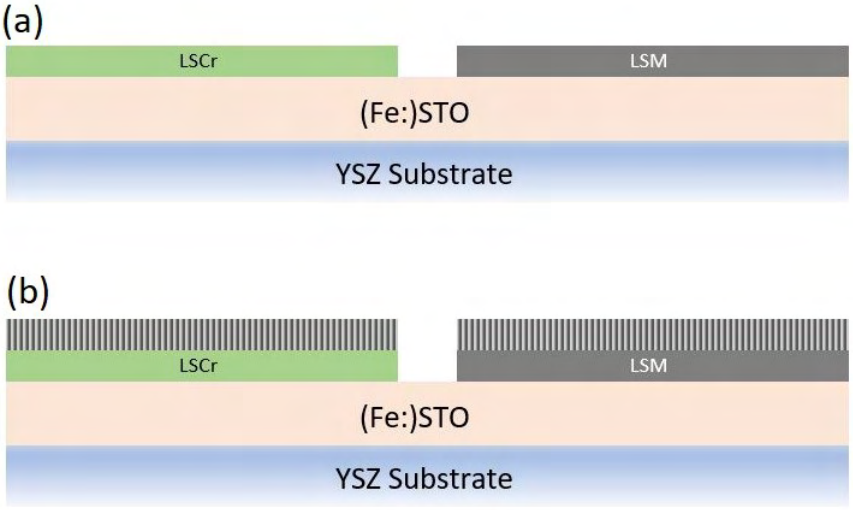

Figure 3.1: Cross-section of thin film samples (a) general setup (b) with collector grids on top of the electrodes

3.1.2 Samples with single crystal STO application (SC)

Following the procedure described by Morgenbesser *et al.* [20], samples were created from $SrTiO_{3-\delta}$ [100] 10x10x0.5 mm single crystal substrates (CrysTek Germany). These were furnished with a thin film of LSCr, LSM or gold as working electrode on one side of the substrate and a porous layer of Pt as counter electrode on the other side (see Figure 3.2).
A total of 9 samples were prepared, 7 of which with LSCr, which will be denoted as SC-LSCr 1 to 7 and one sample each with LSM and Au, respectively, denoted as SC-LSM and SC-Au.

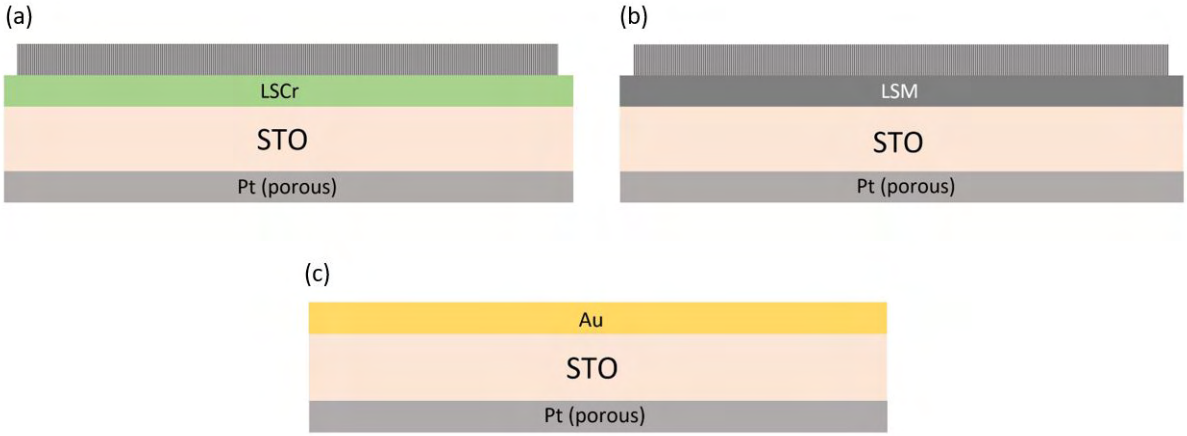

Figure 3.2: Different types of samples with STO single crystal application with (a) LSCr, (b) LSM and (c) gold as working electrode (not to scale)

While the Au-working electrode of sample (c) was sputtered according to Table 3.5, LSCr and LSM electrodes were applied by PLD using parameters described in Table 3.4. While LSCr was prepared in the same fashion as on the thin film samples, LSM had to be a lot thinner as it was now used as a working electrode and with a thickness of 200 nm the much stronger UV absorption of LSM compared to LSCr would have already been too strong to measure significant photovoltages.

Table 3.4: PLD parameters for the working electrodes on SC samples

Material	Temperature (°C)	Pressure (mbar)	Pulses	Frequency (Hz)	Thickness (nm)
LSCr	700	$1.5 \cdot 10^{-2}$	4 500	5	100
LSM	550	$4 \cdot 10^{-2}$	1 500	5	50

After deposition of LSM and LSCr a current collector grid was prepared in generally the same way as on the thin film samples using lift-off photolithography and magnetron sputtering but with differing parameters according to Tables 3.5 and 3.6. Since the platinum showed significantly worse adhesion on the electrode materials grown on STO-100 single crystals than on the materials grown on the STO thin film on the YSZ-100 substrate (see 3.1.1), the parameters had to be adjusted. Additionally it was necessary to first sputter a layer of 5 nm of titanium on the samples before applying the platinum to further increase the adhesion of the grid.

Table 3.5: Parameters for sputtering

material	Ti	Pt	Au
sputter time	56	162	14 s
Ar pressure	$7 \cdot 10^{-3}$ mbar	$2 \cdot 10^{-2}$ mbar	$2 \cdot 10^{-2}$ mbar
sputter current	100 mA	100 mA	100 mA
thickness	5 nm	100 nm	15 nm

Table 3.6: Parameters for lithography for on SC-LSCr and SC-LSM samples

photoresist	150 μl
spincoater speed	100 rps
drying	2 min at 106 °C
UV exposure time	80 s
developing time	70 s

In two instances, both with LSCr as working electrode, the electrode material's surface had to be roughened via ion beam etching using an ion gun (KDC-40 Sidewinder, BeamTec Germany) following the parameters shown in Table 3.7 before photolithography to enhance the adhesion to Ti and make the current collector grid stick to the electrode.

The porous Pt counter electrode was added by brushing a terpineol based Pt paste on the sample and drying for 10-15 min at 115-130 °C. The first LSCr sample was initially prepared with a Pt-YSZ paste, although this was replaced with a pure Pt electrode after annealing the sample once, as the sample did not show the desired behaviour (see Section 4.3.3). This also led to the decision to prepare all subsequent samples with pure Pt instead of Pt-YSZ.

Table 3.7: Parameters for ion beam etching

etching time	30 s
Ar pressure	$9.4 \cdot 10^{-4}$ mbar
plasma current	20 mA
beam voltage	500 V
accel. voltage	100 V

3.1.3 Profilometry

After preparation, the samples were investigated through profilometry using a Bruker DekTak XT stylus profilometer. These results are described in more detail in Section 4.1.1.
Five measurements were performed on each TF sample at random spots located along the "valley" between the electrodes (see Figure 3.1 a) with every measurement starting on LSM, moving across the valley and ending on LSCr. Both sides were then averaged and compared to the STO in between, which served as a referential baseline.

3.2 Description of the measuring apparatus

All samples were measured throughout the whole course of this work in the same setup consisting of two main parts: The measuring apparatus on which the samples were mounted and a tube furnace. Both parts consist of a number of different elements themselves, which are listed below with the enumeration referring to Figure 3.3:

(A) A tube of fused silica was used as the housing for the other elements

(B) The counter electrode contact consisting of a small Pt sheet in the front wrapped tightly around the tip of the base for same-side electrode samples (TF samples) and a larger Pt sheet at the back used for measurements in across-plane sample geometry with working and counter electrode on opposite sides of the sample (SC samples)

(C) The working electrode contact similar to the front part of the counter electrode

(D) Platinum wires in silica tubes for electrical wiring

(E) A type S thermocouple also in a fused silica housing running alongside the electrical wiring and placed close to the sample

(F) Connections for the electrical wires

(G) Connection for the thermocouple

(H) Gas in- and outlet for atmosphere-dependent measurements

(I) The tube furnace

(J) Shielding meshes to avoid electrical disturbances

(K) The housing of the 350 nm UV lamp used to illuminate the samples

(L) A quartz waveguide to guarantee direct illumination

(M) Mounted rails for easy access to the measuring apparatus

All samples were placed in the apparatus with tweezers after moving the furnace to the left using the rail mounting.
The SC samples were wedged between the working electrode contact sheet and the counter electrode contact sheet. Contacting the front side of the samples with the frontal sheet for the counter electrode had to be strictly avoided to not create a short circuit.
The TF samples had to be adjusted after the initial placement so that they were wedged between the front and back plate on both sides. Contact of the sample and the back Pt sheet was not an issue as the sample's backside should not be electrically conducting. The contacting of all samples is shown in Figure 3.4.

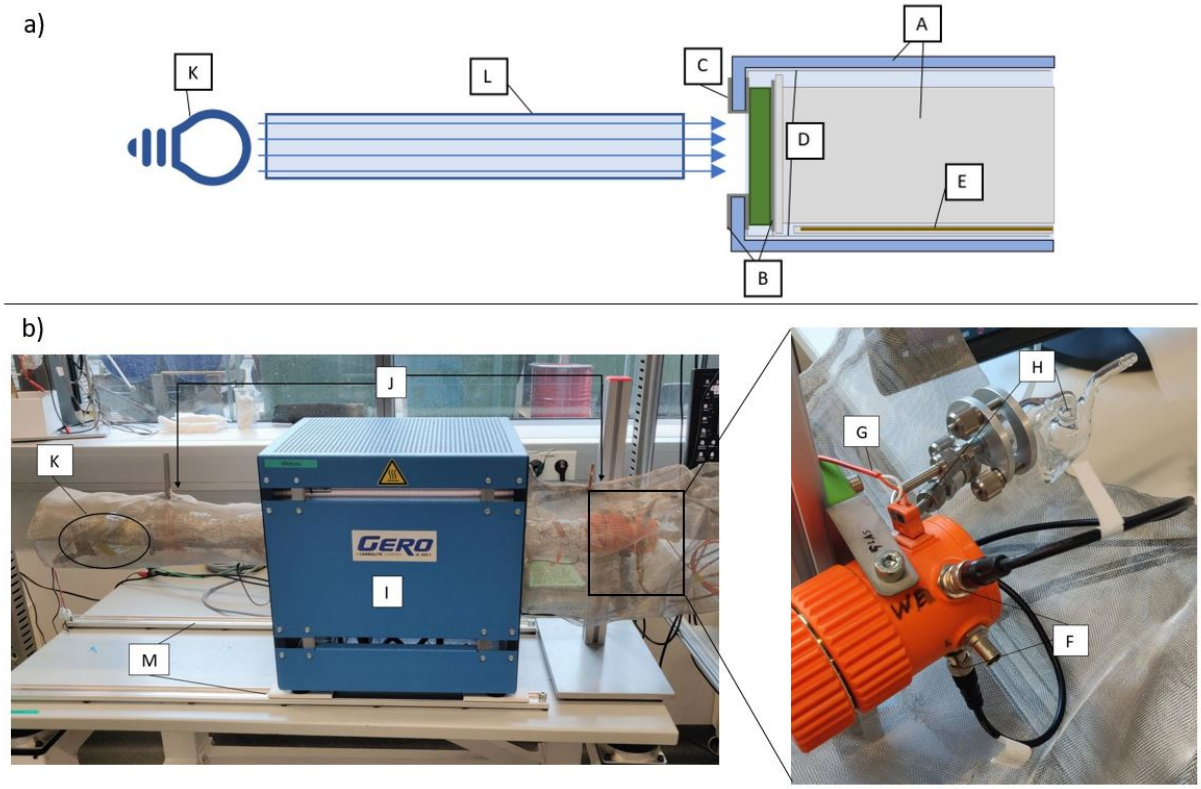

Figure 3.3: Detailed schematic of the sample (in green) built into the measuring apparatus (a) and the tube furnace with annotations (b)

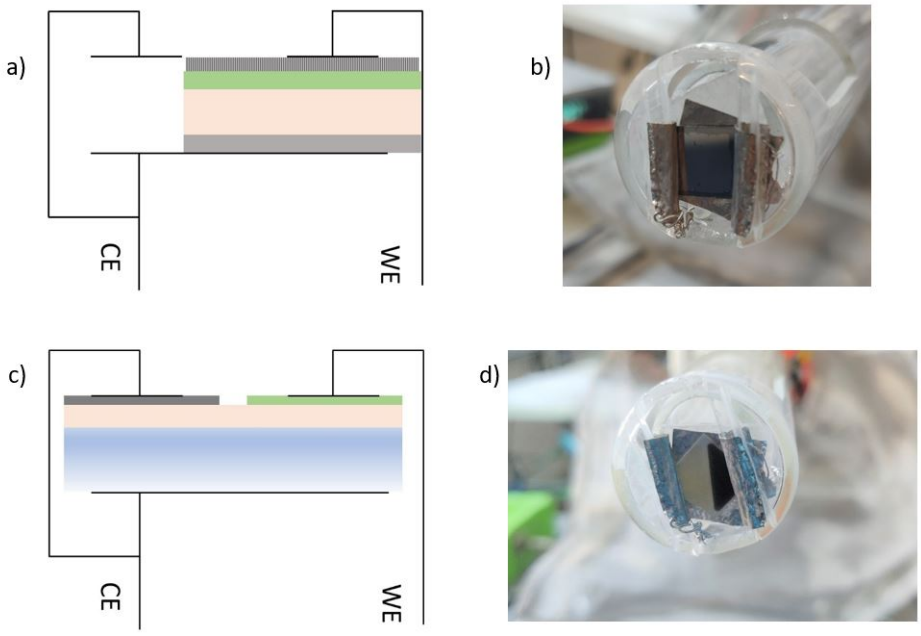

Figure 3.4: Schematic cross-sections of the SC- (a) and TF-samples (c) contacted in the apparatus with WE and CE denoting Working Electrode and Counter Electrode contacting; actual samples SC-LSCr 3 (b) and STO 10 (d) built into the measuring apparatus are shown next to the respective schematic

3.3 Measurements

The measurements of all samples generally consisted of three parts:

- Photovoltage: The PV measurements were performed using a Keithley Dmm2000 (Keithley Instruments, USA) and measuring in an open circuit condition with the sample as source. The measurements were done in cycles, starting with the sample not being illuminated and switching the UV-lamp described in section 3.2 on and off in equal intervals. The duration of these intervals and number of cycles were varied for different types of samples and will be denoted in the respective sections.

- Electrical photo-current: Current measurements were conducted in the same fashion as voltage measurements using the same Keithley Dmm2000 apparatus and switching the UV-lamp on and off in certain intervals. This was, however, performed as a short circuit measurement and the illumination intervals were again equal for TF samples but varied for SC samples.

- Impedance spectroscopy: A Novocontrol Alpha A High Frequency Impedance Analyzer was used to investigate the samples in a 4-terminal sensing layout. In all cases, a voltage of 20 mV was applied but the frequency range was varied between TF and SC samples, with the TF samples being measured from 1 MHz to 1 mHz and the SC samples being measured from 1 MHz to 100 mHz. With 10 points being measured for every decade in all cases, this lead to one full spectrum being recorded for the SC samples in about 8 min and ca. 4 h for a spectrum of a TF sample.
  Akin to the measurements of photo-voltage and -current, light cycles were applied such, that at least two full spectra could be recorded every time the UV lamp was turned on or shut off, resulting in intervals of 30 min for SC samples and 12 h for TF samples.

3.3.1 Electrolyte material dependent experiments of TF samples

As the main interest in thin film applications of STO was the effects of cation non-stoichiometry, all experiments were carried out in ambient air at a constant temperature of 350 °C. As described in the previous section, all samples were placed in the apparatus according to Figure 3.4.
For photo-voltage measurements, illumination intervals of 2 h were chosen since there was typically a strong time dependency on voltage (see Results). These cycles were repeated 6 times, to investigate reproducibility and account for long-time drifting of the sample's baseline voltage, resulting in a total duration of 24 h per sample.
Current measurements were also conducted in intervals of 2 h, although these were only repeated in 5 cycles (a total of 20 h), since most of the samples did not generate enough photo-voltage for any significant current to be measured (see Results) and long-time equilibration was never an issue.
Impedance spectroscopy was performed as described above and was typically the last measurement for every sample.

3.3.2 First set of single crystal experiments

The main point of interest considering the SC-samples was the behaviour of the chronoamperometrical enhancement reported in earlier works. To study this, four samples with the same composition were made as described above which are denoted as SC-LSCr 1 through 4.
These samples were at all times analyzed in a cycle that consisted of

1. Impedance spectroscopy
2. Measurement of photovoltage
3. Measurement of current enhancement
4. Impedance spectroscopy
5. Measurement of photovoltage

in this order.

To study the effects of the apparently permanent current enhancement on impedance and photovoltages, these measurements were always performed before and after the amperometrical measurement. Since the SC-samples showed only minor battery effects and thus tended to reach an equilibrium voltage much faster than the TF samples while also not showing any long-time drifting, the illumination intervals for voltage measurements were set to 20 min and only two illumination cycles were performed for each voltage measurement.
As stated above, Impedance spectroscopy could also be performed at a much faster rate as there was no need for measuring frequencies below 100 mHz. Two illumination cycles were also conducted here for studying changes in resistance after illumination and for the sake of reproducibility.
These time savings were however completely cancelled out by the measurements of electrical current, which were performed in cycles with 1 h of no illumination and 12 of illumination. Turning the UV lamp off and on again in certain intervals was done to see if the changes in current were permanent.

3.3.3 Electrode material dependent experiments on SC-samples

Two samples with different working electrodes, SC-LSM and SC-Au were created to study the influence of the electrode material on the samples' behaviour concerning photo-voltage and especially photo-current. These were supposed to be analyzed in the same way as the SC-LSCr samples, but since SC-Au initially showed very low photo-voltage, measurements of current and subsequent analysis were omitted for this sample (see Section 4.3.4).

3.3.4 Annealing and temperature dependent experiments on SC-samples

In an attempt to "reset" the permanent changes observed in the SC-LSCr samples they were annealed at 600 °C (ramping of 5 °C per minute) for various durations and then analyzed again. The exact times for annealing can be found in Table 3.8.

Table 3.8: Annealing times for every sample

Sample	Annealing cycle	Annealing time (h)
SC-LSCr 1	1	48
SC-LSCr 2	1	36
SC-LSCr 3	1	12
	2	36
	3	24
SC-LSCr 4	1	36
SC-LSM	1	48

SC-LSCr 3 was the main sample of interest in this case and the only sample that was used to study the effects of repeated annealing. In the following work, the different states of the sample will be denoted as "pristine", "12 h annealed", "two times annealed" and "three times annealed". SC-LSCr 4 was only analyzed once to find an equilibrium current I_{eq}, but was not tested again after annealing, since the collector grid seemed to show severe signs of corrosion/degradation (see Section 4.1.2).
Temperature-dependent measurements were conducted after annealing for each sample except for SC-LSCr 4 by performing the same measuring cycle described in subsection 3.3.2 at 300 and 400 °C. SC-LSM was the only sample with temperature dependent measurements in its pristine state as well as in the annealed state.
This leads to three factors of temporary or permanent change to the samples' behaviour:

- before/during/after illumination
- before/after enhancement
- before/after annealing

3.3.5 p(O_2)-dependent experiments of SC-samples

Since the chronoamperometrical current enhancement was suspected to be tied to oxygen vacancy diffusion in the electrolyte material and/or integration and removal of oxygen from the material, three more SC-LSCr samples were prepared to study the effect of oxygen partial pressure on the samples. An overview of these experiments can be seen in Table 3.9.

Table 3.9: Gas mixtures used for analysis on samples

Sample	oxygen/nitrogen ratio (%)
SC-LSCr 5	1:99
SC-LSCr 6	100:0
SC-LSCr 7	20:80

These samples had to be freshly prepared to give a good comparison to other pristine samples since annealing did not fully reset the changes of the chronoamperometrical enhancement but instead also irreversibly altered the samples' behaviour.

4 Results and discussion

4.1 Sample preparation

4.1.1 TF samples

Since the preparation of TF samples was mainly based on experience values as similarly produced samples have been described previously (e.g. by *Morgenbesser et al.* [20] [32]), there was no greater focus on the compositional analysis of the films on the samples prepared during the course of this work. However, samples were checked by optical microscopy and profilometry to give insight on the overall quality of preparation.

STO 7 Target

The preparation of the STO7 target was successful and produced a porous pellet as depicted in Figure 4.1. It can clearly be seen that unlike stoichiometric STO, which would turn black in reducing atmosphere due to the high number of electrons in the conduction band [104], the increased Sr-content in the target seemed to counteract this phenomenon as the target was still white after the sintering process with only a slight yellowish tint at the surface.

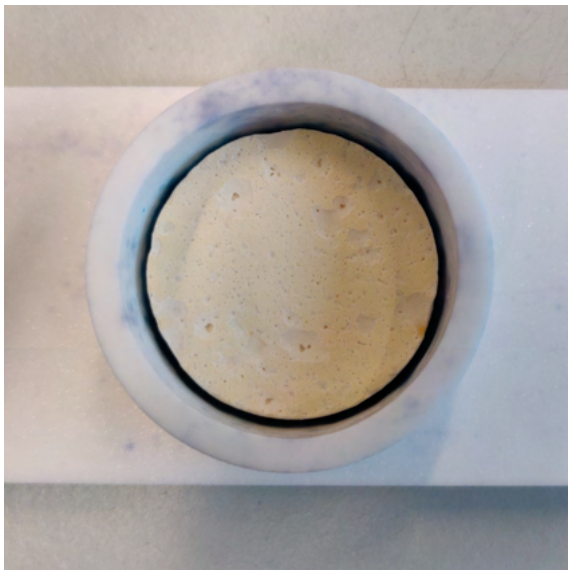

Figure 4.1: The target used for preparation of STO 7 films, shown directly after the second sintering process

Optical investigation of samples

In Figure 4.2 an overview of the different types of TF samples is given. As the samples did not notably differ in appearance, 4.2 a) shows only one representative sample (STO 5), with the lighter coloured electrode being LSCr and the dark coloured electrode being LSM. In Fig 4.2 b), the STO 7/2 sample can be seen with the current collector grids on top of the electrodes. The samples with symmetrical electrodes, which were prepared to provide further insight to impedance spectroscopic measurements (see Section 4.2.1), shown in c) with LSCr/LSCr on the left and LSM/LSM on the right. Some of the samples showed a permanent darkening of the STO layer after UV illumination, with the symmetrical LSCr/LSCr sample of STO 7/2 being the most notable example (shown in Figure 4.2 d) next to a similar sample with undoped STO and no change of colour). This is in line with the observations of *Viernstein et al.* [17] regarding high-temperature photochromism of Fe:STO.

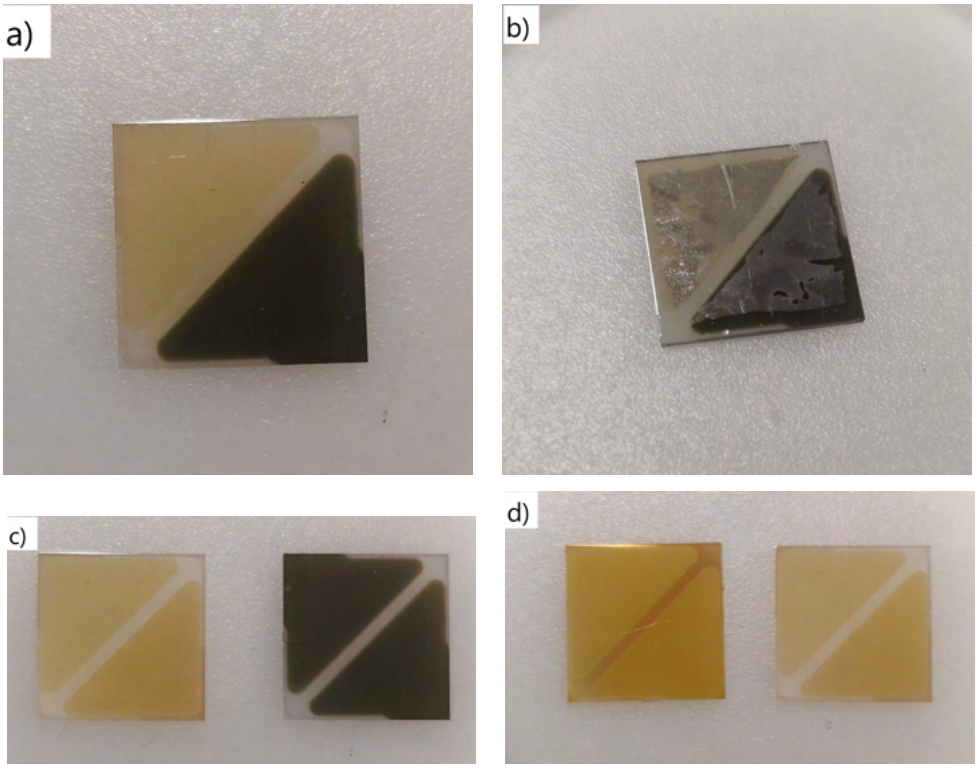

Figure 4.2: Overview on TF samples: a) standard setup without current collector grid, b) with current collector grid, c) symmetrical samples for EIS and d) observed photochromism in Fe:STO

Figure 4.3 shows microscopic images of the STO 7/2 sample already furnished with the current collector grids. Although the grids show noticeable gaps, where the sputtered metal would not fully stick to the surface and some supposedly blank sites (especially on the left side) that could not be fully cleared by washing with EtOH, the preparation described in section 3.1.1 generally worked out as intended, as the grids only cover the electrodes with no contact between them. Distance measurements showed that the space between the electrodes has a width of ca. 750 μm and a length of about 1 cm. The distinct difference in colouring of the electrodes can not be seen anymore under the microscope due to iridescent interference.

Remarkably, the grids showed an unusually high roughness which can also clearly be seen in Figure 4.3 especially when compared to the grids on SC samples in Section 4.1.2. This is attributed to being a consequential effect of the thin films' roughness, as they were not grown epitaxially on the substrate. Distance measurements have shown that the mesh size of the grids corresponds closely to the 15 μm/35 μm relation of the mask used for photolithography.

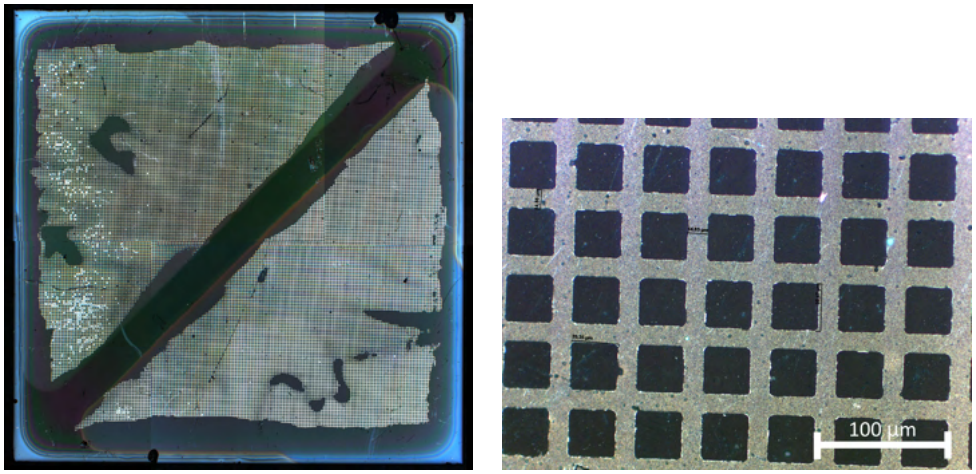

Figure 4.3: Microscope image of STO 7/2 with current collector grids. lhs: Overview on the samples; rhs: detailed view of the grid; note the roughness of the Pt surface

Profilometry

Profilometric measurements were performed to validate to what extent the thickness of films assumed from experience values corresponds to the actual film thickness on the samples. Two test samples were used as a representative of the full measurement series: STO 5 to represent undoped samples and the corresponding STO 5/2 to represent samples with Fe doping. The measurements were performed in a straight line across the "valley" between the electrodes as this was for one considered the shortest path for measuring both electrodes at once and also expected to show the steepest and thus most definite edges.

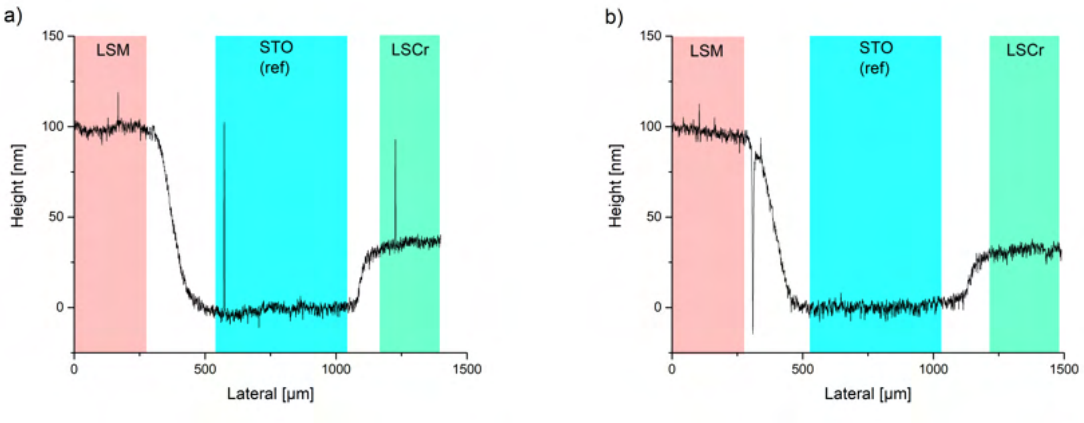

Figure 4.4: Height profiles of electrode films on a) STO 5 and b) STO 5/2. Sudden spikes are caused by dust particles on the surface, sudden notches are caused by small pores

Figure 4.4 shows one measurement of each sample with the areas highlighted that were used to determine the average height along the measured line.
Interestingly enough, the thickness of both electrodes was grossly overestimated when choosing the respective parameters for PLD (see Table 3.2), with LSM reaching an average thickness of around 102±7 nm and LSCr no more than 42±7 nm (Table 4.1) on both samples, as opposed to the expected 200 nm for LSM and 100 nm for LSCr. While this seems odd and especially the results for LSCr are less than half of the planned sample preparation, this misconception should still not be a heavy impediment on the expectable results for photovoltage as this is mostly defined by the thickness of the space charge layer which should be in the range of 10 to 20 nm [20, 32].
On the other hand, the LSCr layer being more or less half as thick as the LSM layer corresponds very well with the number of laser pulses used during the PLD process (4500 for LSCr and 9000 for LSM; Table 3.2).

	STO 5		STO 5/2	
	LSM (nm)	LSCr (nm)	LSM (nm)	LSCr (nm)
	100	41	97	36
	95	48	100	35
	109	45	108	42
	101	38	101	39
	107	38	98	36
Average	102.4	41.4	100.8	37.6

Table 4.1: Measured thickness of LSM- and LSCr-films across the samples' centre "valley"

One additional measurement was performed on both samples starting from the lower left corner of each sample (when looking at the sample like in Figure 4.2 a)) measuring about 2 mm along the "valley" to determine the thickness of the STO layer. Although no clear baseline could be found, the measurements showed height profiles of 520 and 600 nm, meaning that the full film should be slightly thicker. Unlike the electrodes this would closely match the assumed thickness of 650 nm.

4.1.2 SC samples

As with the TF samples, all of the SC samples were fabricated in the same fashion and thus optically nearly indistinguishable. Thus, only one sample is shown as an example in Figure 4.5. As described before, the adhesion of the grid was significantly weaker here compared to the STO 7/2 sample, requiring the use of Ti as a base layer and in some instances even a roughening of the electrode layer. This overall smoothness of the surface also lead to very smooth platinum grids (Figure 4.5) as opposed to the rough grid on the TF sample.

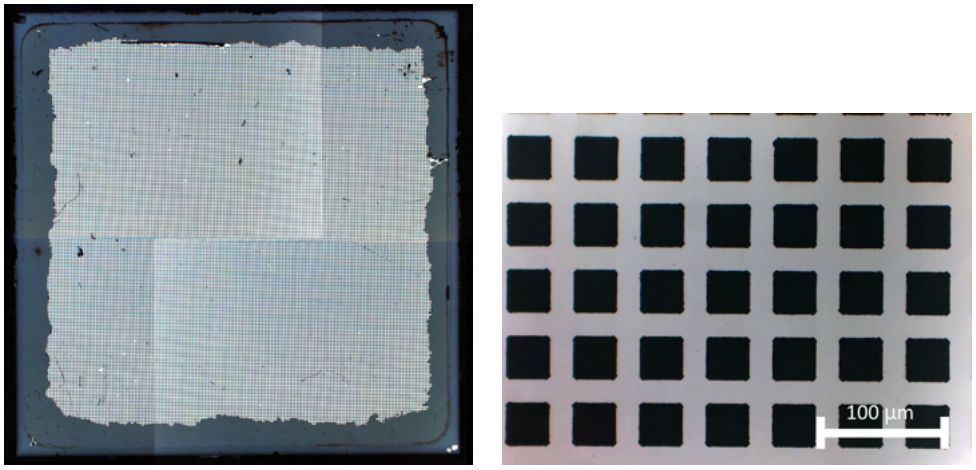

Figure 4.5: lhs: Full view of a representative sample (SC-LSCr 3) under the microscope with the current collector grid clearly visible. Inconsistencies in the picture are owed to manual stitching of four images as the whole sample could not be captured by the camera. rhs: Detailed view of the current collector grid (SC-LSCr 1)

With the grids sticking to the electrode layer to varying degrees it is obvious that they will also cover areas of varying size. This was measured manually by microscopy for each sample individually and is represented in Table 4.2. With the samples' surface being exactly 1 cm^2, the values shown there directly correspond to the percentage of surface covered, e.g. SC-LSCr 1 had 77.8 % of its surface covered by the grid. Generally speaking, all samples showed a coverage of around 70 %. It should be noted that of these 70 %, only $\approx$ 50 % were covered with Pt braces, leaving the other half of free surface in between.

Sample	Size of current collector grid (cm^2)
SC-LSCr 1	0.778
SC-LSCr 2	0.660
SC-LSCr 3	0.719
SC-LSCr 4	0.676
SC-LSCr 5	0.703
SC-LSCr 6	0.709
SC-LSCr 7	0.747
SC-LSM	0.674

Table 4.2: Size of the surface area covered by the collector grid for each individual sample

Effects of annealing on grid morphology

Two of the samples, SC-LSCr 4 and SC-LSM, showed significant macroscopical darkening of large areas of the collector grid following the annealing process described in Section 3.3.4, which is shown in Figure 4.6 a) and b) respectively. While this initially led to the decision to not use SC-LSCr 4 for further measurements of voltage, current or impedance spectroscopy, SC-LSM actually did not show any changes in behaviour that were not to be expected (see Section 4.3.4), indicating a negligible impact of the changes in morphology.
The detailed view of SC-LSCr 4 in Figure 4.6 c) shows the reason for the macroscopic darkening being what appears to be a large amount of pores and precipitations in the platinum, which formed during the annealing process. Contrary to this, SC-LSCr 3 did only show a very slight slight change in colour (Fig. 4.6 d)), which was not visible macroscopically even after multiple annealing processes for a total time of 72 h. Still, a cumulated emergence of pores could be noticed, indicating that the same process takes place in every sample but at a varying rate.

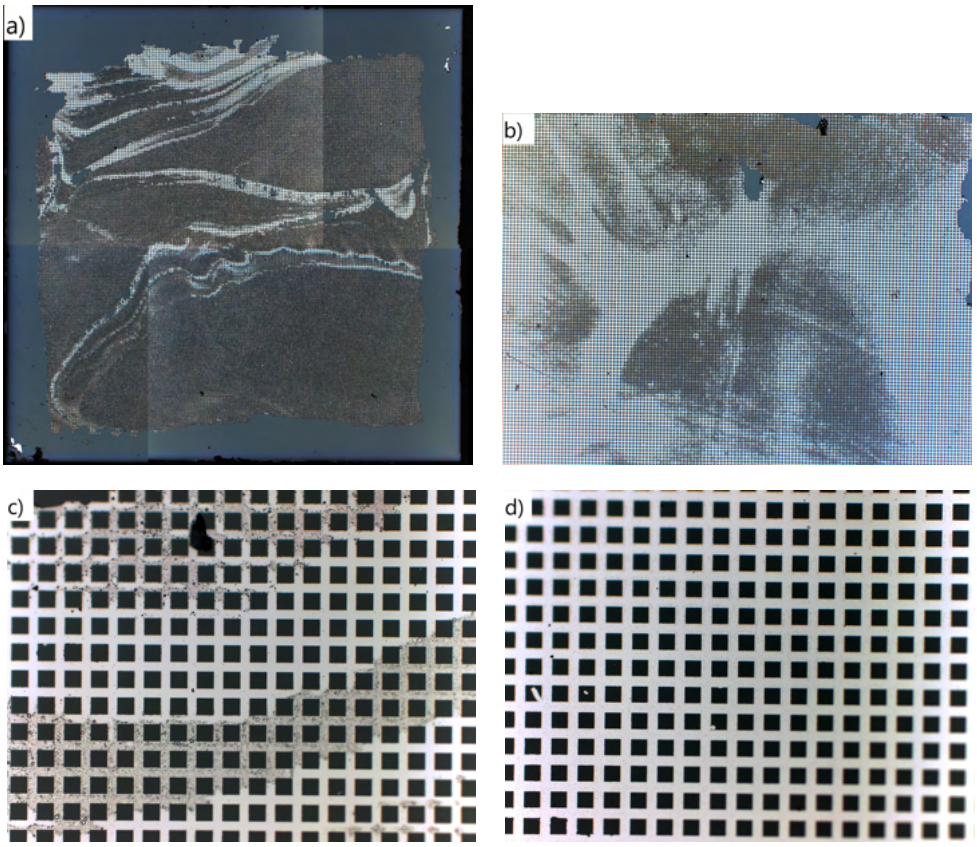

Figure 4.6: Optical degradation of current collector grids: a) SC-LSCr 4 after annealing, b) SC-LSM after annealing, c) SC-LSCr 4 after annealing (detail), d) SC-LSCr 3 after annealing (detail)

4.2 STO composition dependent measurements on TF samples

As stated above, the samples with thin film application were only tested at ca. 350°C and lab air. The only variation performed between measurements was the change of STO composition on different samples according to Table 3.1. Since previous works on the same PLD apparatus have shown that the usage of targets with an excess of 7 & Sr yields films with a stoichiometric ratio Sr/(Ti+Fe) of 1 (see Figure 4.7), this composition will be referred to as "stoichiometric". Accordingly, compositions of higher Sr-content will be considered overstoichiometric and those of lower Sr-content understoichiometric. Consequently, it will be assumed that the sample created from the undoped STO 7 target shows an Sr/Ti-ratio of 1 with the nomenclature following the same scheme as the doped samples.

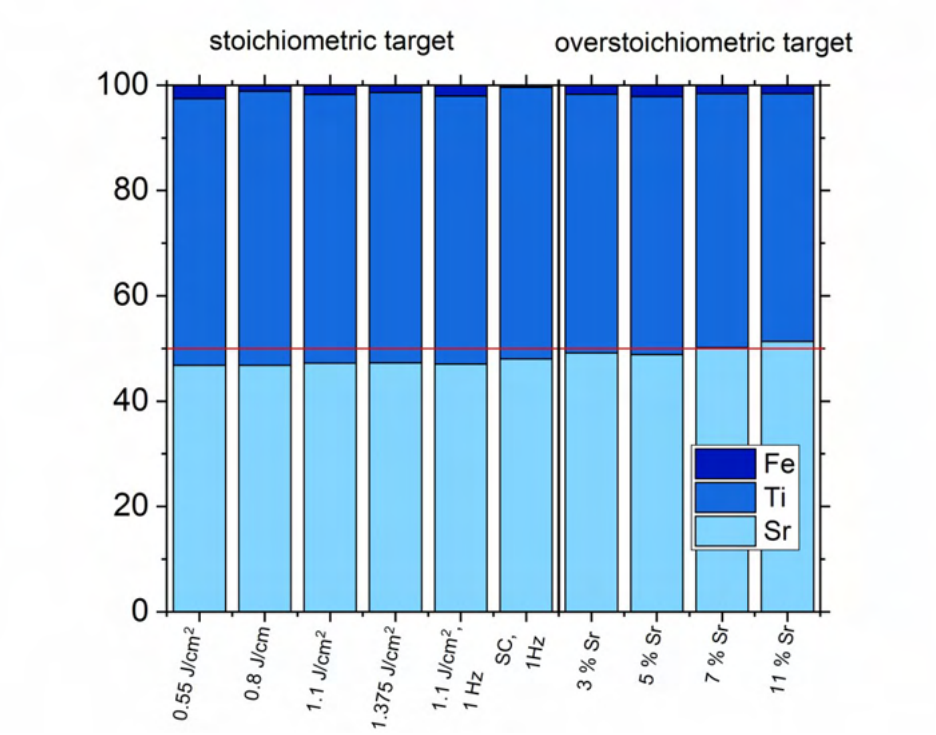

Figure 4.7: Results of ICP-OES (Inductively Coupled Plasma - Optical Emission Spectroscopy) measurements of stoichiometry in Fe:STO thin films. A compensation of 7 % excess Sr in the target leads to a stoichiometric composition in the films; reproduced from [32]

4.2.1 Impedance spectroscopy

Impedance spectroscopy was performed as described in Section 3.3 from 1 MHz to 1 mHz on every sample. Consistent with previously reported data [19,20,102] the spectra of unilluminated samples always showed three distinct features, which will be denoted as high-, mid- and low-frequency feature for further notice. With the exact transmission line for this sample geometry being highly complex, it was decided to instead fit the spectra with an equivalent circuit of three serial RC-elements (Fig. 4.8), which generally turned out to sufficiently image the measured spectra without running the risk of needlessly overparametrizing the system.

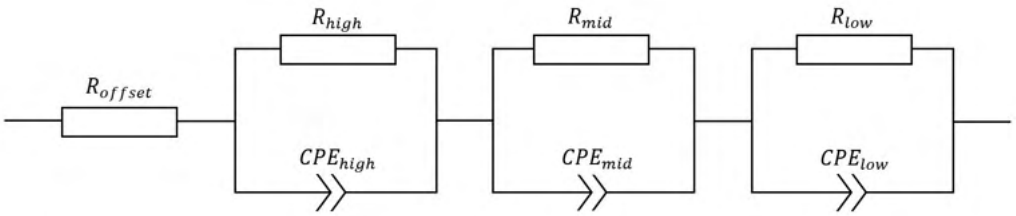

Figure 4.8: Simplified model of the transmission line in the samples used for measurements. High, mid and low refer to the relative frequency range of the respective features.

To account for non-ideal capacitive behaviour, Constant Phase Elements were used in the fit instead of ideal capacitors. Additionally, another resistor was added in series (R_{offset}) of the transmission line to account for possible offsets (e.g. due to wiring), although the value of this was typically negligibly small.

Undoped samples

While EIS measurements of undoped STO TF samples did show the expected three features in the spectra it is immediately obvious when looking at Figure 4.9 that while these features tended to show a smaller resistance upon UV illumination, they never fully collapsed. The mid-frequency feature did although show a sizeable relative reduction of resistance in most cases and actually seemed to vanish entirely in the case of STO10 (Fig. 4.9 d).
Correctly attributing the features to their respective causes proved difficult for a number of reasons and was mostly based on assumptions. As the measurements were performed in-plane and thus the sample geometry was inherently different to conventional cells with electrodes on opposite sides of the sample, the current path was not exactly clear. To identify the feature related to the bulk conductivity of STO it was thus assumed that the current flowing through the sample would take the shortest possible path, i.e. only the "strip" between the LSCr- and the LSM-electrode would be the "active" part of the STO. This strip was measured to be ca. 1 cm long, 750 μm wide (see Section 4.1.1) and assumed to be 650 nm thick since profilometry could not provide more insight on the exact thickness of the STO thin films. After calculating the capacitance C of the features from the given data through Equation (2.50) the sample was regarded to behave like a simple plate capacitor with the STO bridge as its dielectric. Through the commonly known relation

$$C = \varepsilon_0 \cdot \varepsilon_r \cdot \frac{A}{d} \tag{4.1}$$

$$\varepsilon_r = \frac{C}{\varepsilon_0} \cdot \frac{d}{A} \tag{4.2}$$

the permittivity ε_r was calculated for each feature with the vacuum permittivity ε_0 rounded to $8,85 \cdot 10^{-14} \frac{F}{cm}$, the dielectric's thickness d being the strip width, and the area of the "plates" being $A = 650\,nm \cdot 1\,cm = 6,5 \cdot 10^{-5}\,cm^2$.
This led to typical permittivity values of $1.1 \cdot 10^5$ to $1.5 \cdot 10^5$ for the high frequency feature, which appears to be too high for bulk STO at 350 °C by a factor of about 10^3, according to literature [95,125]. This discrepancy was however attributed to stray capacitance from an interaction with the underlying YSZ substrate and the high frequency feature was nonetheless initially treated as representing the bulk STO.

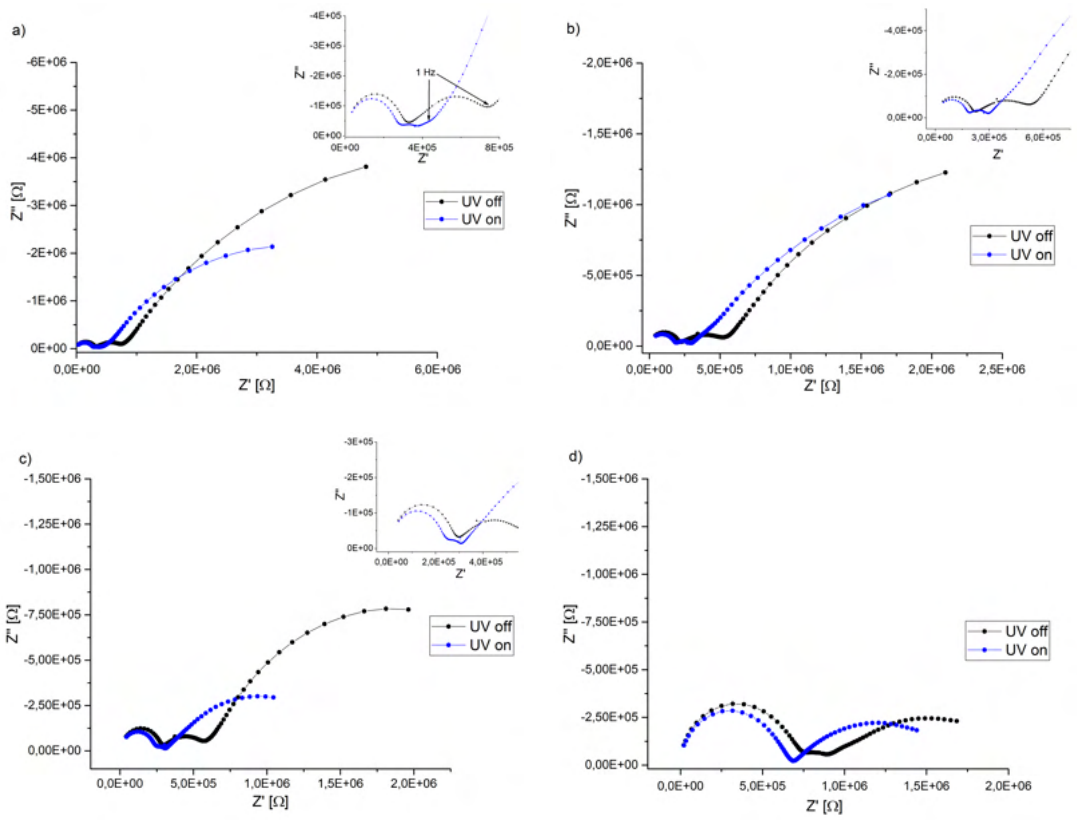

Figure 4.9: Impedance spectra of undoped STO TF samples: a) STO, b) STO 5, c) STO 7, d) STO 10; detailed views of the smaller high- and mid-frequency features are shown in the top right corner of each diagram where necessary. Note the significant difference in axis scaling between uncompensated STO and samples with compensation

The conductivity of the high frequency feature was calculated through Equation (2.52) in the form of

$$\sigma = \frac{1}{R} \cdot \frac{d}{A} \tag{4.3}$$

with the same assumptions for d and A as before and will be treated later in this section in more detail.

The MF and LF features, although not (fully) collapsing under UV illumination, were considered to derive from space charges at the electrode/electrolyte (STO) interface, as has been described before [19, 20]. While the MF feature, as stated above, did clearly become smaller upon illumination in all cases, the LF feature only decreased in size in two of the four instances, STO 0 and STO 7. Though being only mildly and unsteadily affected by UV light, the LF feature seemed on the other hand to show a significant dependency on the amount of Sr-compensation, declining steadily while the compensation increased, as shown in Figure 4.9.

Comparison to symmetrical samples

To gain additional insight on the nature of the MF and LF feature, samples with a symmetrical electrode layout (i.e. both electrodes being the same material) were exemplary prepared on the basis of STO 0. Figure 4.10 shows the direct comparison of the STO 0 sample with its counterparts that feature only LSCr- and only LSM-electrodes.
When looking at Figure 4.10, it can be seen directly that both LSCr (b) and LSM (c) form space charges with the underlying STO, but they visibly behave in a different manner. Not only do the HF feature and especially the LF feature of LSCr show a far greater resistance than the respective features in the LSM sample, they also seem to be only mildly affected by UV illumination while the MF and LF features of LSM show a clear decline in resistance with the MF feature nearly fully collapsing.
Comparison to the standard undoped STO sample shows pretty much a combined effect of the two control samples. Initially a situation similar to the LSCr sample can be observed with a HF and MF feature of similar resistance and a much larger LF feature. Unlike the symmetrical LSCr sample, these MF and LF features do notably decline under UV illumination, although not to the same extent as on the LSM sample.

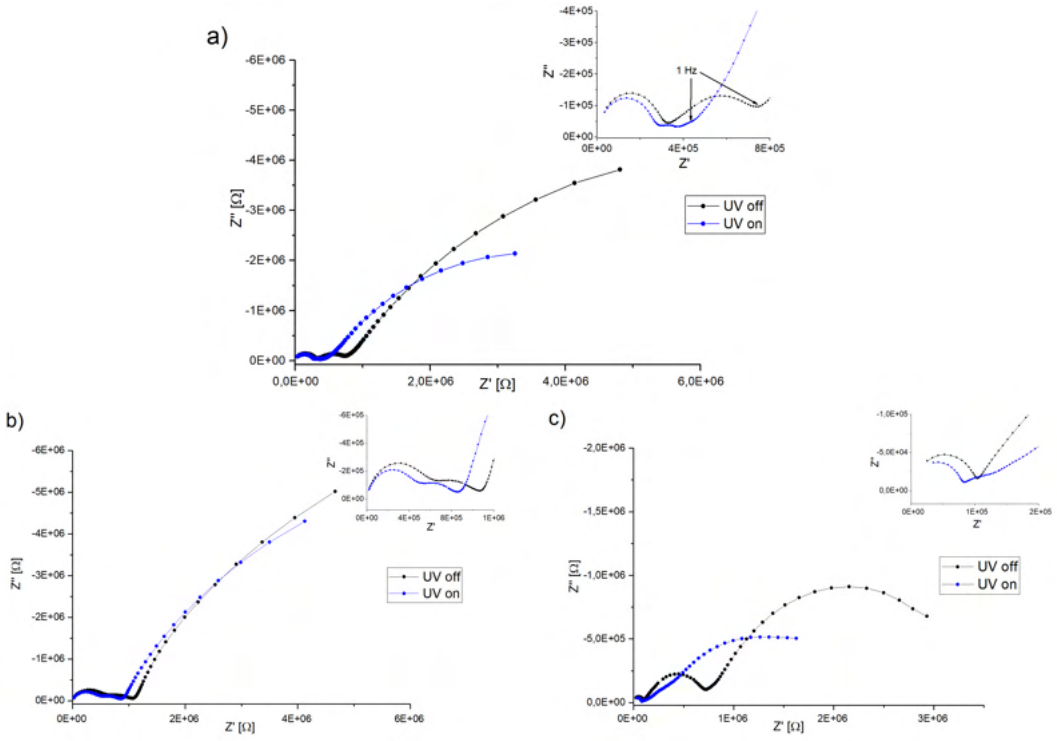

Figure 4.10: Spectra of EIS measurements of reference samples with symmetrical electrode setup. All samples feature undoped and uncompensated STO as the main layer: a) asymmetric STO sample with LSCr/LSM electrodes, b) sample with symmetrical LSCr/LSCr electrodes, c) sample with symmetrical LSM/LSM electrodes

When comparing the resistance values shown in Table 4.3 and Figure 4.11, it can be seen that the value of the HF feature of STO 0 very precisely represents the midpoint between the respective value of the control samples. A similar observation can be made for the LF feature of STO 0, that is about 3 times as high as the respective feature on STO LSM and about a third of the LF feature of STO LSCr. The MF feature on the other hand does not show such a relation, reaching the highest value for STO LSM and the lowest for STO 0. This might be owed to sample deviation though, as the values for all three samples are relatively similar. And while the resistance of the HF feature of STO 0 is still placed between STO LSCr and STO LSM (although not directly in the middle) no comparisons can be made for the MF and LF feature as no clear values could be calculated for STO LSM.

Table 4.3: Resistance values for every feature of the samples shown in Figure 4.10. No values are given for the MF and LF feature of the STO LSM sample under illumination as they could not be clearly separated

	dark			illuminated		
	R_{HF} (Ω)	R_{MF} (Ω)	R_{LF} (Ω)	R_{HF} (Ω)	R_{MF} (Ω)	R_{LF} (Ω)
LSCr/LSM	$3.03 \cdot 10^5$	$5.13 \cdot 10^5$	$1.19 \cdot 10^7$	$2.35 \cdot 10^5$	$2.61 \cdot 10^5$	$9.49 \cdot 10^6$
LSCr/LSCr	$5.04 \cdot 10^5$	$6.04 \cdot 10^5$	$3.11 \cdot 10^7$	$4.06 \cdot 10^5$	$4.89 \cdot 10^5$	$2.85 \cdot 10^7$
LSM/LSM	$1.02 \cdot 10^5$	$6.75 \cdot 10^5$	$3.79 \cdot 10^6$	$6.25 \cdot 10^4$	–	–

While the original intention behind creating these control samples was the idea of possibly getting a clear separation of the MF and LF feature and being able to attribute one feature to each electrode, it seems more reasonable to assume that all features actually represent a combined effect of both of the electrodes' interaction with the base STO. Since the HF range is always 1 MHz to 10 kHz, the MF range is 10 kHz to 1 Hz and the LF range is 1 Hz to 1 mHz, the different contributions can not be separated due to their relaxation frequencies being too similar. This results in three superimposed features with combined characteristics being displayed instead of six individual ones.

Generally speaking, it appears that both LSCr and LSM create space charge regions upon contact with STO, although this region is considerably larger in the LSCr/STO combination compared to the LSM/STO combination, as can be seen in Figure 4.10 and again in Figure 4.11 c). Also, the HF feature does not solely consist of bulk STO, but is clearly influenced by the choice of electrode material, which is again shown through the comparison of resistance values in Figure 4.11 a).

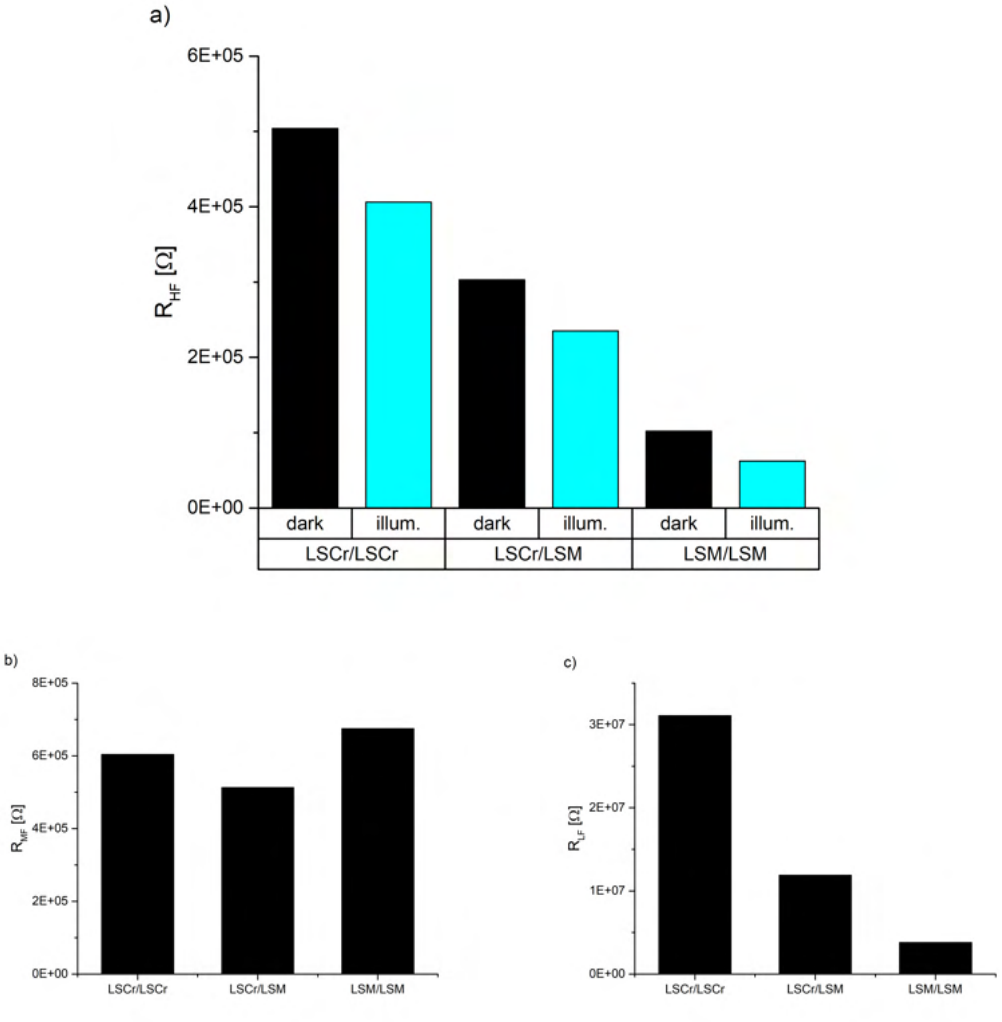

Figure 4.11: Comparison of resistances of the HF (a), MF (b) and LF (c) feature of all three samples. Only the values of the dark spectra are shown for b) and c) as the MF- and LF-feature of LSM/LSM could not be separated under illumination

It should also be noted that when converting R_{HF} of the LSCr/LSM sample to an effective conductivity σ_{eff} through Equation (4.3), it can be seen that this results in a conductivity of about $4 \cdot 10^{-3}$ S/cm, which is unusually high for STO and should be lower by about two to three orders of magnitude, as even polycrystalline STO does not show nearly this conductivity below 500 °C [32].

Thus, it seems reasonable to imagine further contributions to this feature and generally discard the idea of it representing the STO's bulk conductivity. This is shown in the form of a suggested transmission line of current flowing through the sample in Figure 4.12. The electronic conductivity contributions of the electrode materials discussed above are in this case shown in the form of resistances and the full current path is expected to behave in an "across-plane/in-plane/across-plane" fashion with the YSZ substrate being very well part of the full transmission line.

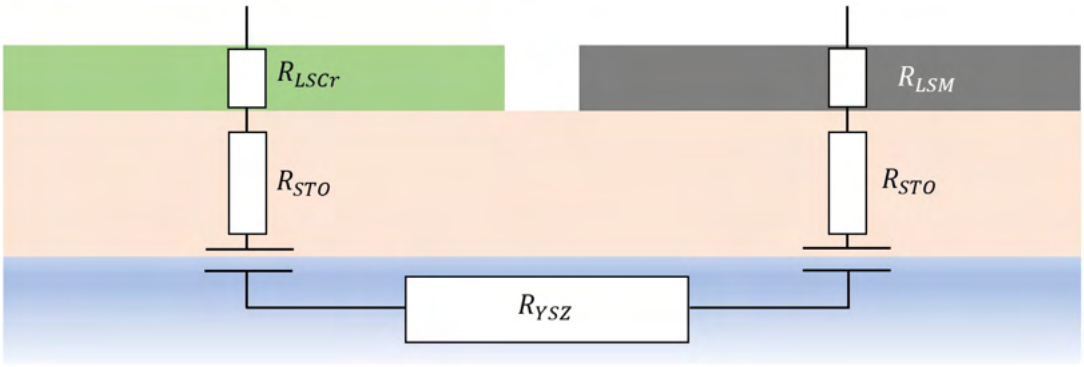

Figure 4.12: Simplified transmission line of TF samples with "across-plane/in-plane/across-plane" current path

Considering this "double across-plane" path for the STO thin film and assuming that on average 0.5 cm^2 of the STO is actually actively conducting current, one can find the across-plane conductivity as

$$\sigma_{eff} = \frac{1}{2R} \cdot \frac{d}{A} = \frac{1}{2 \cdot 3 \cdot 10^5} \cdot \frac{6.5 \cdot 10^{-5}}{0.5} \approx 2.2 \cdot 10^{-10} S/cm \tag{4.4}$$

This value is very much in line with the "pseudo-intrinsic" conductivity for (Fe:)STO at 350 °C found by Morgenbesser *et al.* [32] and discussed above in Section 2.3.1.
Furthermore, considering the contribution of the YSZ substrate, one can find the single crystalline conductivity of YSZ at 350 °C to be ca. $2 \cdot 10^{-5}$ S/cm [126], and thus the resistance of the Substrate to be

$$R_{YSZ} = \frac{1}{\sigma} \cdot \frac{d}{A} = \frac{1}{2 \cdot 10^{-5}} \cdot \frac{0.5}{0.05 \cdot 1} = 500\, k\Omega \tag{4.5}$$

which closely matches the resistance of the HF feature of the LSCr/LSCr sample (Table 4.3) and is clearly similar to the resistance of the of the LSCr/LSM sample.

This means that besides the contributions of the electrodes' electronic conductivity, the HF feature might actually show the substrate's resistance and possibly also the pseudo-intrinsic conductivity of the STO itself. Unlike initially assumed, it would thus be incorrect to attribute this feature to STO alone and as a result it will still be named "HF feature" for further reading.

Samples with Fe-doping

The interpretation of the impedance spectra of Fe:STO was generally done in the same fashion as described for the undoped samples, although these spectra were often notably less insightful. While STO 0/2 did show results very similar to the STO 0 sample, as can be seen in Figure 4.13 a), higher amounts of Sr-compensation led to increased problems. This started with the HF range becoming much larger and spanning nearly the entire range from 1 MHz down to 1 Hz (see Fig. 4.13 c) as an example), resulting in a situation where the LF feature could not be sufficiently resolved anymore since frequency ranges well below 1 mHz would be required to measure the main part of the feature (see Fig. 4.13 b) and d). Additional problems arised e.g. in the case of STO 5/2 (Fig. 4.13 b) and STO 3/2 (not displayed), where discontinuities appeared in the spectra, making a clean fit of the data impossible.

This leaves only a small fraction of usable data for Fe:STO, which is in most cases too little to sufficiently support any statements about trends or influences on other properties. It can although be seen in Fig. 4.13 c) that STO 7/2 shows a spectrum similar to STO 10 in Fig. 4.9 d) indicating a generally similar trend with increasing Sr-compensation.

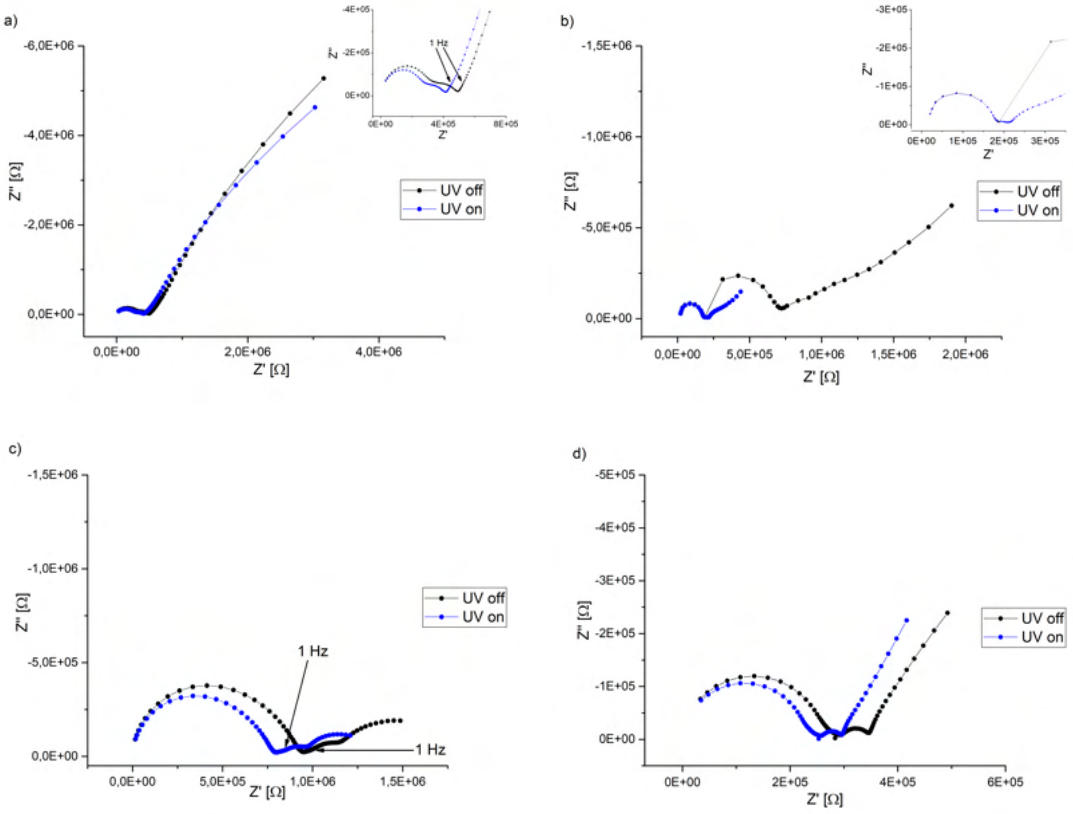

Figure 4.13: Impedance spectra of doped Fe:STO TF samples: a) STO 0/2, b) STO 5/2, c) STO 7/2, d) STO 5/5; detailed views of the smaller high- and mid-frequency features are shown in the top right corner of each diagram where necessary

Influence of Sr-compensation

When comparing the resistance R of the HF feature in the undoped samples to their degree of Sr-compensation, one can see in Figure 4.14 a) that it initially slightly declines, but then rises rather steadily above 5 % compensation, with STO 7 reaching similar values to STO 0 and STO 10 clearly situated above. Illuminating the sample slightly lowers the resistance in all cases except STO 10, where no notable changes in resistance can be observed.

When comparing this to the doped samples in Figure 4.14 b), a similar trend can be observed with the resistance initially dropping but then drastically increasing again. Unlike the undoped samples, here the additional decrease in resistance through illumination does not show any dependency on the degree of compensation. As stated above, the overall values for resistance tend to be quite low and would rather fit to the single crystalline bulk YSZ being measured in plane rather than the actual STO thin film.
This again raises the question - together with the uncommonly high permittivity, which is also off by about 3 orders of magnitude, and the influence of electrode material - to what extent the HF feature truly represents the STO itself. Therefore it should at least be assumed that there is a significant contribution of the underlying YSZ substrate.

The features of lower frequencies on the other hand seem to show generally opposite behaviour. Both the resistances of the MF and LF feature (Fig. 4.14 c) and d) clearly decrease with increasing degree of compensation. But just like the HF feature, both the MF and LF decrease in resistance upon illumination with the MF feature showing the strongest relative decrease. This is most notable in the case of STO 10, where the MF feature became too small to be evaluated upon the sample being illuminated, while the LF feature, similar to the HF feature, did not show any perceptible difference.

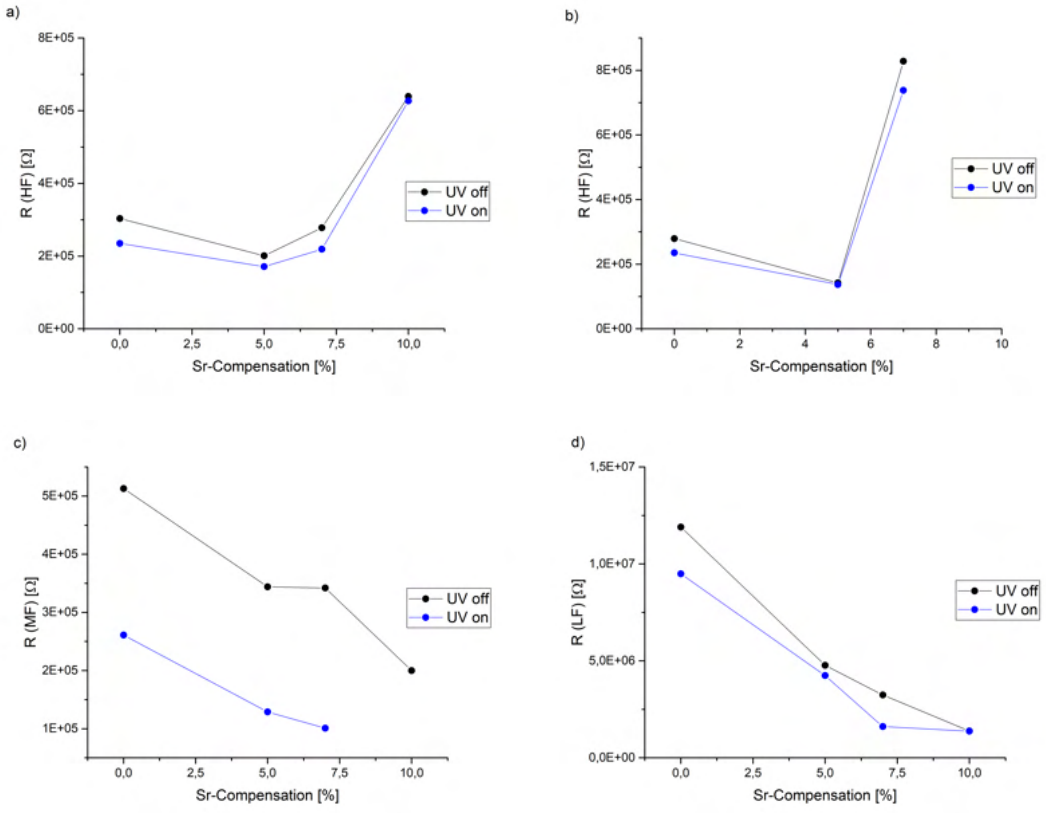

Figure 4.14: Effects of Sr-compensation on the conductivity σ of the STO feature in a) undoped STO and b) Fe-doped STO and on the resistance R of c) the middle frequency and d) the low frequency feature of undoped STO

4.2.2 Voltage measurements

Accurate measurements of photovoltage proved difficult as the samples often took a long time (>20 h) to reach an equilibrium state that could serve as the baseline voltage U_{dark}.
The samples using undoped STO were commonly less affected by this problem although it can be seen in Figure 4.15 that in both of these cases either the upper or lower boundary takes a long time to adjust. Typically, besides the desired photovoltage there also was some electrochemical battery voltage to be observed (see Section 2.3.2), which showed opposing polarity and ultimately led to a decrease of total voltage U_{tot}. This can clearly be seen in the beginning cycles of Fig. 4.15 b) and the final cycles of Fig. 4.15 a).

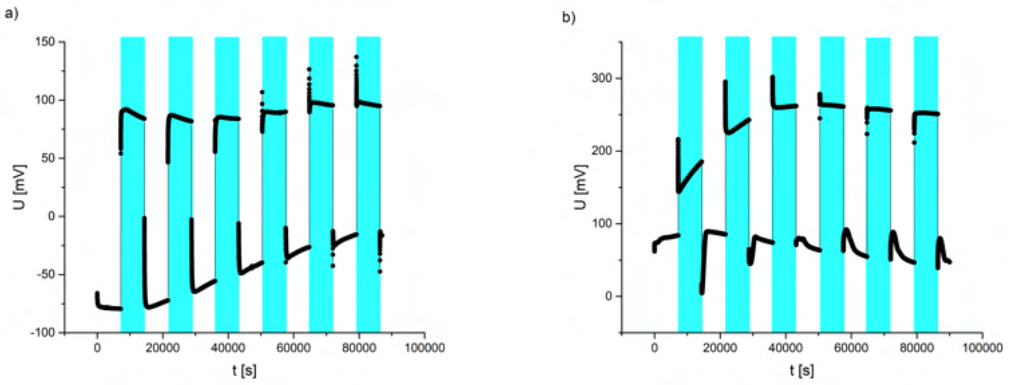

Figure 4.15: Exemplary voltage measurements of two samples with undoped STO as base material; a) STO 0 and b) STO 7; Sections with illumination are marked in blue

As has already been the case for EIS measurements, the samples with Fe doping proved to be significantly more erratic in the generation of voltage than the undoped samples across the board. They showed overall smaller photovoltages, but on the other hand larger battery voltages and more significant drifting of the baseline. This is shown in Figure 4.16 for STO 0/2 (a) and STO 3/2 (b), where especially in the first cycles the drift is so strong that it is notably distorting the voltage measured. It also clearly shows the battery voltage initially (b) or completely (a) outweighing the photovoltage, which results in nearly no total voltage that could be used for potential applications.

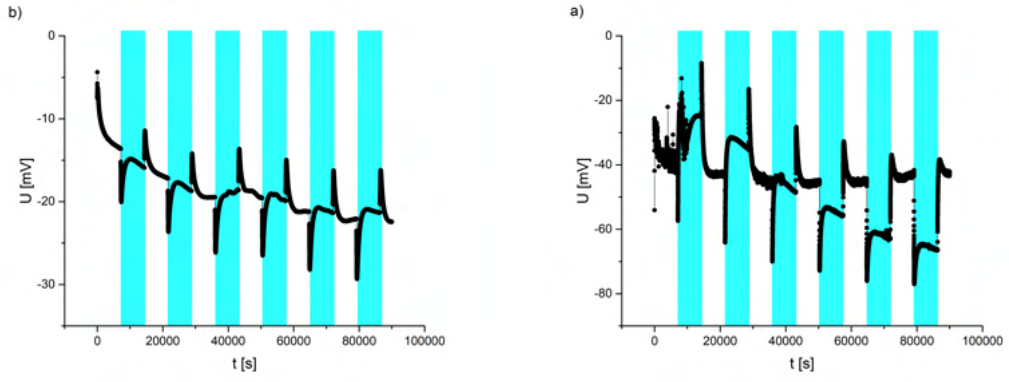

Figure 4.16: Exemplary voltage measurements of samples with doped Fe:STO as base material; a) STO 0/2 and b) STO 3/2; Sections with illumination are marked in blue

Effects of compensation

Comparing the achievable voltage of each sample to its respective degree of Sr-compensation it can be seen in Figure 4.17 a) that in the case of undoped samples, no clear trend can be made out for either photo- or battery voltage. There are however some interesting conclusions to be drawn:
First, the sample achieving the highest photovoltage also showed the least amount of interfering battery voltage, resulting in a total voltage of about 200 mV (see Fig. 4.15 b) which was notably the highest of the entire measurement series. This was achieved by the sample STO 7, which has a stoichiometric Sr:Ti-ratio of 1 in the thin film. This indicates that cation non-stoichiometry might be detrimental to generating photovoltage and ideal stoichiometry should be preserved when trying to maximize open circuit voltage. A similar, though slightly lower voltage was achieved by the uncompensated STO 0, which also matches the similarity of the resistance/conductivity of these samples' HF feature shown in Figure 4.14 a).
Secondly, while the samples with understoichiometric (Sr-deficiency) and stoichiometric thin film composition showed a positive polarity in the generated photovoltage, the overstoichiometric (Sr-surplus) sample STO 10 led to a sudden change in polarity, indicating that the lack of Sr-vacancies may be the reason for this behaviour.

When comparing this to the samples with 2 % Fe-doping in Figure 4.17 b) there is also no clear trend to be made out, but these samples clearly show opposing behaviour to the undoped samples. As long as the thin film composition is understoichiometric, the polarity of the photovoltage stays negative, but upon reaching ideal stoichiometry, the polarity changes. This is again a similarity between the STO 10 and the STO 7/2 sample.
As was the case with undoped samples, the sample created from the target with 7 % excess strontium again achieved the highest photovoltage by far, although a stronger battery voltage could be observed here and the overall voltage was notably smaller, clearly staying below the 100 mV mark. This further strengthens the assumption that ideal stoichiometry in the film should be preserved if high photovoltages are desired.

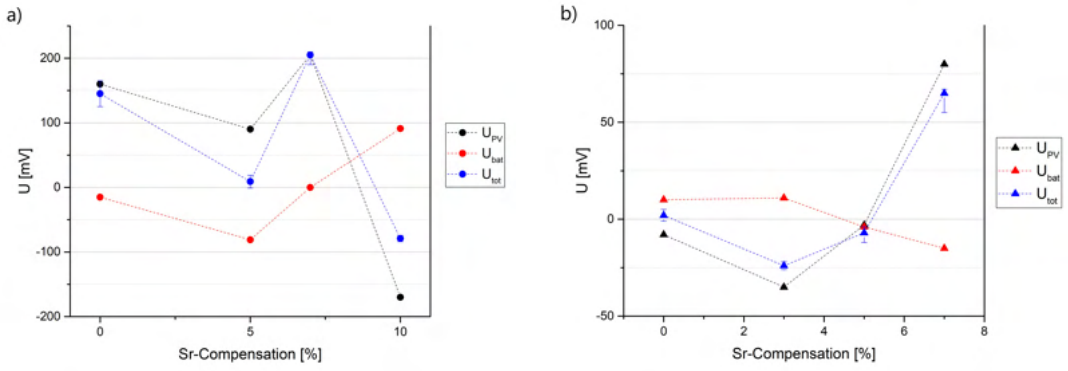

Figure 4.17: Comparison of voltages achieved by every sample and their relation to the degree of Sr-compensation; a) samples with undoped STO, b) Fe:STO samples with 2 % Fe-doping

Effects of doping

While some definite distinctions between generally doped and undoped samples have already been made, there were also tests to see a clear influence of the amount of Fe-doping on the achievable photovoltage. To do this, three samples with the same Sr-compensation (5 %) and varying amounts of Fe-doping were compared in Figure 4.18.
However, throughout the entire measurement series the samples with 5 % Sr-compensation in the target tended to show the most unreliable behaviour together with the lowest photovoltage of both the undoped and doped samples. In Figure 4.18 it can easily be seen that STO 5/5 continues this trend with again rather low photovoltage and a total voltage close to 0 V. While this means that no statements can be made concerning the influence of the amount of Fe-doping, it further fortifies the assumption that Fe-doping generally decreases the achievable photovoltage rather than increasing it.

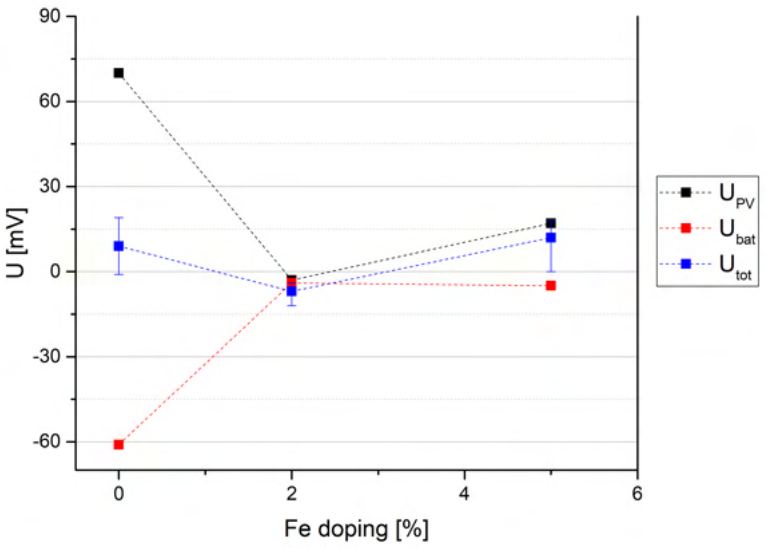

Figure 4.18: Voltage generated by samples with 5 % Sr-compensation in the target in relation to the amount of Fe-doping

4.2.3 Current measurements

Current measurements on TF samples were mostly performed for reasons of completeness as no high values were to be expected from in plane measurements. And indeed only those samples, that achieved >100 mV of photovoltage, produced a measurable current. These are shown in Figure 4.19 a) though c). None of the other samples was able to produce photocurrent beyond noise, which is shown exemplary in Figure 4.19 d) for STO 7/2.
Still, even the measurable current from STO 0, STO 7 and STO 10 was extremely small with initial peaks of about 0.2-0.3 μA followed by a decline down to ca. 0.1 μA for STO 7 and STO 10 and even less in the case of STO 0. In all cases, it can be seen that even without illumination, a dark current I_{dark} of about 0.15 μA superimposes the measurement, which leads to an absolute $|I|_{light}$-value of nearly 0 in the case of STO 10 although it clearly achieved some photocurrent.

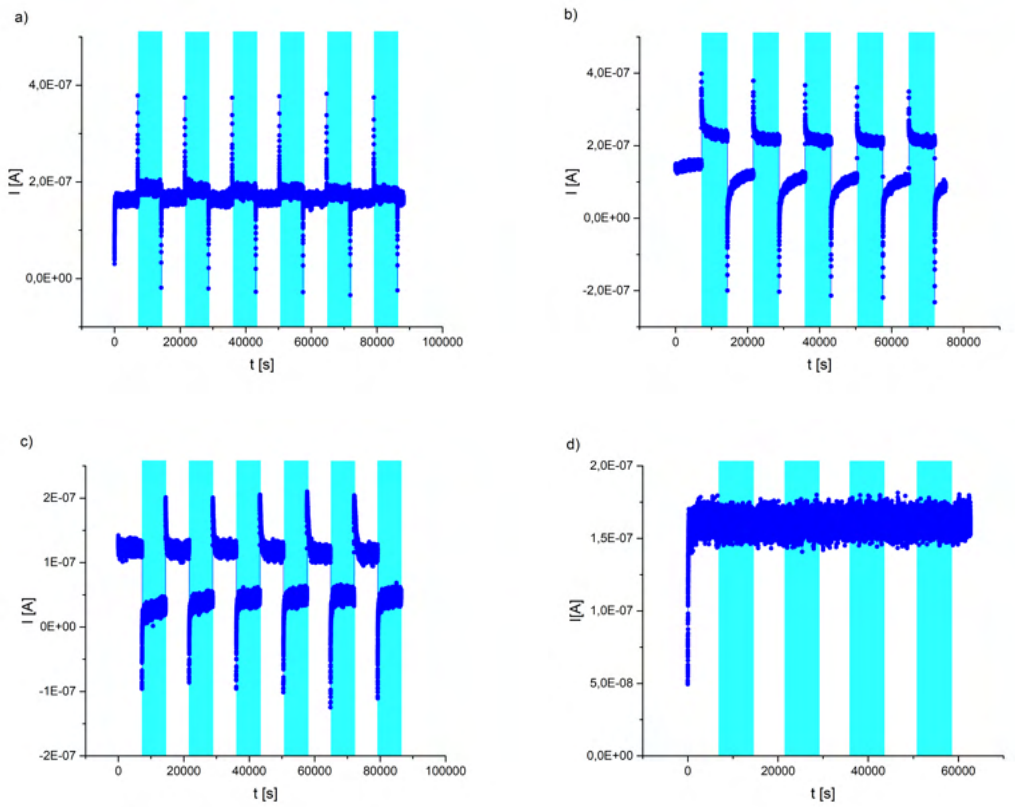

Figure 4.19: Results of current measurements: a) STO 0, b) STO 7, c) STO 10, d) STO 7/2; Sections with UV light illumination are marked blue

4.2.4 Effects of current collector grids

To study the effects of applying current collector grids, the sample STO 7/2 was chosen since it already showed the most consistent voltage profile out of all the samples in question, which can be seen in Figure 4.20. Also, unlike the undoped samples that generated notable photovoltage, it showed no discernible current beyond noise, making it easy to see if this change would actually enhance the photocurrent in the sample.
When comparing the impedance spectra in Figure 4.20 before (a) and after (b) applying the grids, one can see that this application leads to the HF feature slightly declining in resistance while the other features increase in resistance and also merge together. This further indicates that the HF feature consists not only of bulk STO, but is also influenced by the electronic conductivity of the electrodes. It also appears that a fourth feature becomes visible as the merged part after the HF feature starts off with a small "shoulder" before showing two more flattened features.
The changes in photovoltage were probably the most significant ones. While the voltage profile of the sample after application of the grids (Fig. 4.20 d) showed an even more consistent behaviour, the overall voltage that could be achieved dropped from ca. 80 mV to 40 mV. This could probably be explained by the fact that applying a collector grid on the surface effectively reduces the area of the electrode that can be illuminated and thus also reduces the voltage that can be generated by the sample. Interestingly enough, the overall polarity of the sample changes and it takes a lot longer for the sample to reach "full" voltage. This may indicate that predominantly electrochemical battery voltage is measured here instead of the desired photovoltage.

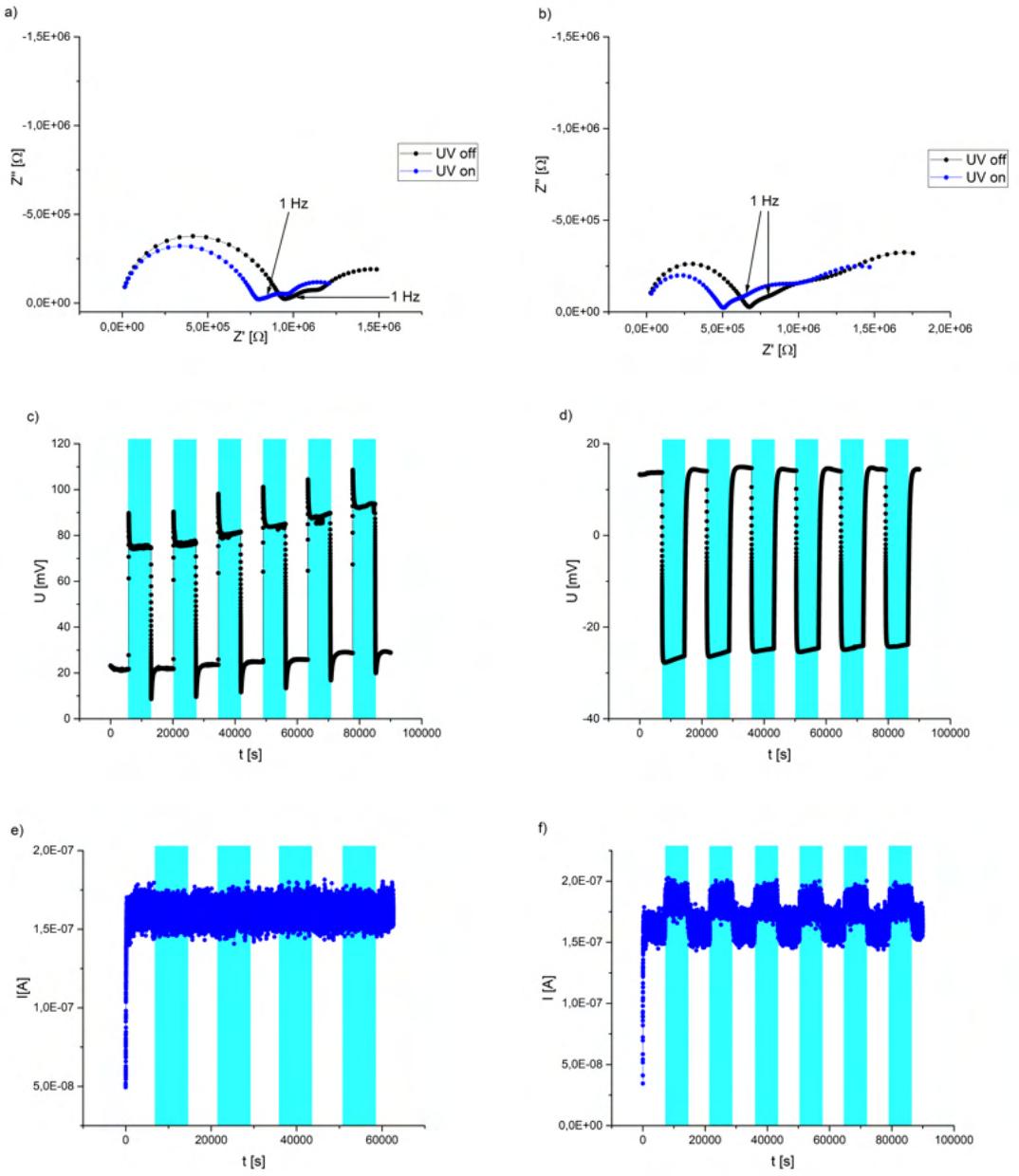

Figure 4.20: Difference in voltage, current and EIS measurement on the same sample with and without current collector grid. The measurements on the left hand side (a, c, e) correspond to the sample without the collector grid and the measurements on the right hand side (b, d, f) correspond to the sample with the collector grid. The sections with the UV light being turned on is marked with blue in c) through f)

Lastly, concerning the achievable current it can be seen by comparing Fig. 4.20 (e) and (f) that applying a collector grid does indeed lead to a measurable current, although this is extremely small with only about 50 nA.

All things considered, it can be said that the application of current collector grids does indeed change the cell's behaviour, but this change is negligible in the case of photocurrent and not beneficial in the case of photovoltage.

4.3 Investigations of SC samples

Unlike the TF samples, this series of measurements does not include variations of the stoichiometric composition, as all of the samples are based on the same undoped and nominally stoichiometric STO [100] single crystals. Instead, the investigation was mainly focused on the influence of different materials for working electrodes, temperature and oxygen partial pressure on the achievable photovoltage and photocurrent. The main focus of the entire measurement series was the investigation of the samples' seemingly self-enhancing behaviour concerning the generation of photocurrent.
Up to Section 4.3.6 all measurements shown were conducted at 350 °C and in lab air.

4.3.1 Initial voltage of SC-LSCr samples

As stated in section 3.1.2 four initial samples with LSCr were created to verify reproducibility and sample variability of the results. By looking at Figure 4.21 one can indeed see that all measurements of photovoltage are very reproducible. It is also immediately obvious that the SC samples performed remarkably better than the TF samples in this respect, as all of the samples already showed a stable baseline dark voltage from the beginning with only negligible drifts, e.g. in the case of LSCr-2 (Fig. 4.21 b). This is paired with a stable photovoltage of approximately 1 V (with no counteracting battery voltage) compared to a maximum of 200 mV for STO and 80 mV for Fe:STO TF samples, which in any case never reached the time stability of SC samples.

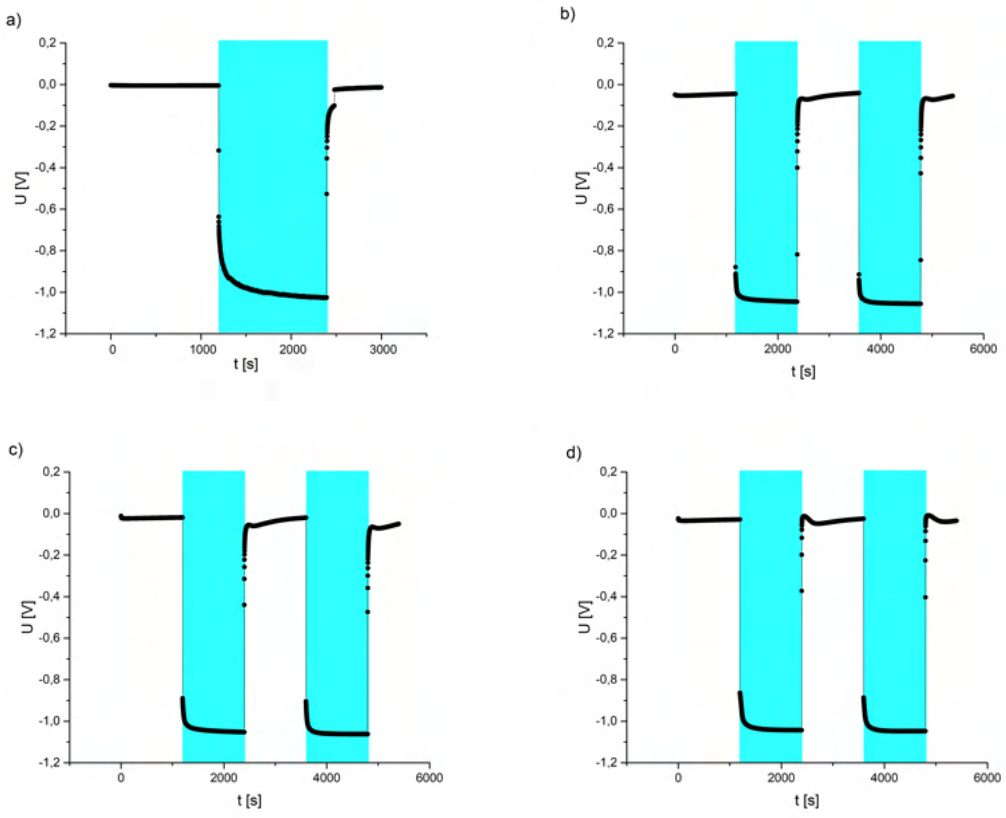

Figure 4.21: Initial measurements of photovoltage for the first series of SC samples with LSCr as working electrode material; a) LSCr-1, b) LSCr-2, c) LSCr-3, d) LSCr-4; Sections with UV illumination marked in blue

Furthermore, when comparing the timescale it typically only takes the SC samples 3-5 minutes after the start of the UV illumination to reach a steady voltage whereas many of the TF samples did not show any stable voltage even after 2 hours of illumination. The only SC sample taking longer to reach a steady state and also showing no immediate "drop" to 0.8-0.9 V upon illumination but rather 0.6 V was LSCr-1 (Fig. 4.21 a). This was most decidedly owed to the sample being initially equipped with a Pt-YSZ counter electrode, which led to overall worse behaviour, although the impediments on the samples' voltage properties in particular were relatively minor.

4.3.2 EIS results of pristine SC-LSCr samples

Considering EIS measurements there are again three distinct features to be seen in Figure 4.22 a) in any case, when measuring the pristine samples in lab air at 350 °C and without any illumination. It can also be seen that the samples LSCr-2 to 4 again showed very similar behaviour with especially LSCr-3 and 4 producing nearly the exact same spectrum and LSCr-2 only slightly diverging. The spectrum for LSCr-1 is not shown as the Pt-YSZ counter electrode led to a heavily distorted spectrum.

With the values for ε_r and σ calculated for the HF feature in Table 4.4, it can be seen that in the case of SC samples, this is in agreement with literature for permittivity [20, 95, 102] and conductivity [127] of bulk STO at 350 °C. It is thus clear that the HF feature of SC samples represents the STO and further indicates that this is not the case for TF samples.

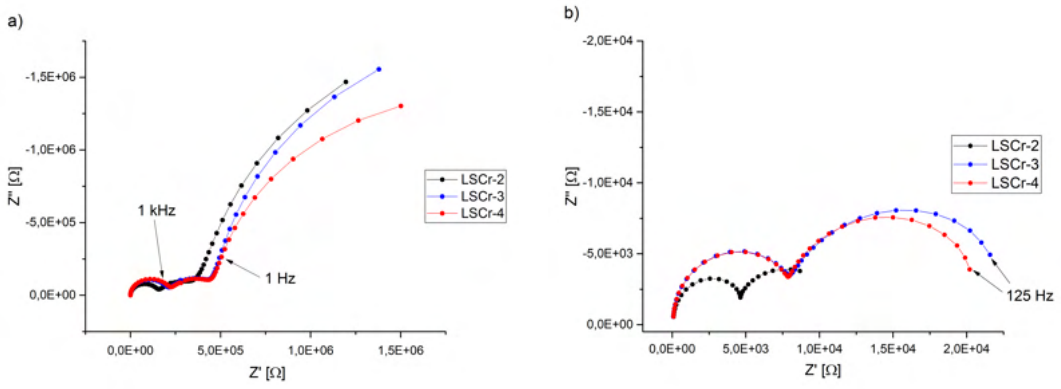

Figure 4.22: Impedance spectroscopy of initial samples; a) dark, b) illuminated; LSCr-1 is not shown since the measurement did not produce a physically meaningful spectrum

The spectra of the initial pristine samples during UV illumination are shown in Figure 4.22 b) and we can see again very similar spectra of LSCr-3 and 4 and LSCr-2 showing overall lower resistance. Unlike the TF samples, here a complete collapse of the LF feature can be seen with the measurements not producing any more physically meaningful data but instead only erratic "jumping" of measurement values below a frequency of 125 Hz. Also the resistance of the first two features sees a clear decrease by a factor of approximately 20.

Table 4.4: Permittivity and conductivity values for the HF STO feature and resistance values for the MF and LF feature in Fig. 4.22 a), all measured at 350 °C

		STO	MF	LF
	ε_r	σ (S/cm)	R (Ω)	R (Ω)
LSCr-2	183	$3.43 \cdot 10^{-6}$	$2.43 \cdot 10^{5}$	$4.73 \cdot 10^{6}$
LSCr-3	165	$2.53 \cdot 10^{-6}$	$2.79 \cdot 10^{5}$	$4.21 \cdot 10^{6}$
LSCr-4	173	$2.73 \cdot 10^{-6}$	$2.71 \cdot 10^{5}$	$3.05 \cdot 10^{6}$
Literature	≈ 170	$7.8 \cdot 10^{-6}$ (400°C)	-	-

4.3.3 Influence of current enhancement

To discuss the overall influence of the current enhancement on the cells, it is obviously necessary to first discuss the current enhancement itself. Figure 4.23 shows the results of the current measurements of the pristine samples LSCr-1 through 4. Here, it became immediately obvious that the Pt-YSZ counter electrode of LSCr-1 (a) did not show the desired behaviour, as there was indeed some enhancement to be seen, but even after 60 h this was still in the sub-μA range. But since the changes in the sample leading to higher currents seemed to be permanent, as they remained even after switching the UV lamp off and back on again after 1 h, even changing the material of the counter electrode afterwards would not make it possible to get another current measurement or impedance spectrum of the "pristine" LSCr-1 sample.

The other three samples on the other hand did work as intended and showed results similar to each other. After an initially strong increase to about 0.17 mA for LSCr-2 (b) and 0.08 mA for LSCr-3 (c) and LSCr-4 (d) respectively, the current started to further increase at a close to constant rate. Because of the significant time investment for these measurements, only one sample - LSCr-4 - was measured until I_{eq} was reached, which was at around 0.77 mA and took a full 12 cycles or 7 days to reach. It is thus not certain that the other samples would reach the same I_{eq}, although it will be assumed that at least LSCr-3 would take an overall similar course, as not only the initial increase was very similar between these two samples but they also reached a value of about 0.6 mA after 5 cycles. This is also in line with what has already been described by *Morgenbesser et al.* [20]
LSCr-2 instead showed a clearly faster increase in photocurrent, achieving nearly 0.7 mA after just 3 cycles. Still, it remains unclear if this would also lead to a higher I_{eq} or if the same I_{eq} would just be achieved faster. This difference might be linked to the bulk conductivity of the STO, which was calculated from impedance data to be similar for LSCr-3 and 4, but somewhat higher for LSCr-2, as has already been shown in Table 4.4.

It should be noted that all values given for photocurrent mentioned in this work and shown across all graphs depicting current measurement represent the actual current measured. Since the samples' base surface area is 1 cm^2, the area specific current density would technically have the same value, but as there was always a part of the sample clamped behind the electrode contact, the actual surface illuminated is smaller and thus the current density might be higher by about 15-20 %. The actual difference can although not be clearly evaluated, as the samples had to be placed manually into the measurement apparatus, which is of course always incident to irregularity.

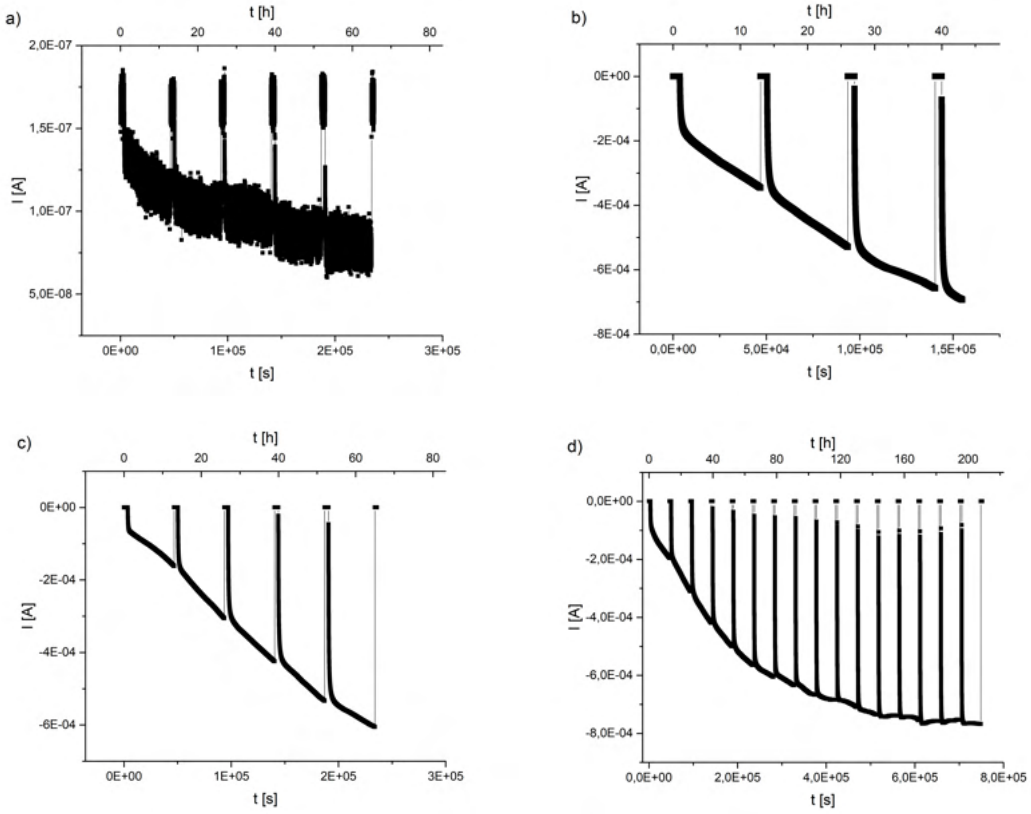

Figure 4.23: Initial measurements of photocurrent for the first series of SC samples with LSCr as working electrode material; a) LSCr-1, b) LSCr-2, c) LSCr-3, d) LSCr-4

Influence on Photovoltage

As explained in Section 3.3.2, following the current measurement additional measurements of photovoltage and impedance spectroscopy were performed to see possible changes induced in the samples by lasting effects of current enhancement. The results of voltage measurements are shown in Figure 4.24 and it can immediately be seen, that the enhancement of photocurrent seems to also have led to an enhancement in photovoltage.

First, the samples LSCr-2 through 4 show an overall "sharpened" behaviour, reaching the equilibrium voltage faster under illumination and especially after turning the UV lamp off again. Additionally, the initial offset in dark voltage seems to be gone entirely and the voltage achieved under illumination is clearly enhanced, resulting in an overall gain in photovoltage of >100 mV in every sample (shown in Table 4.5). Interestingly enough, this voltage enhancement does seem to be a discrete change unlike the current enhancement, which happens continually over time. Even though the current for LSCr-2, 3 and 4 was measured for significantly different times, the change in photovoltage shows no dependency on how long the current enhancement was measured or if I_{eq} was reached. After the enhancement, the differences in behaviour between the three samples are negligible, indicating that probably relatively early during the current enhancement the samples reach a new state of voltage equilibrium with modified interfacial properties leading to overall higher voltages.

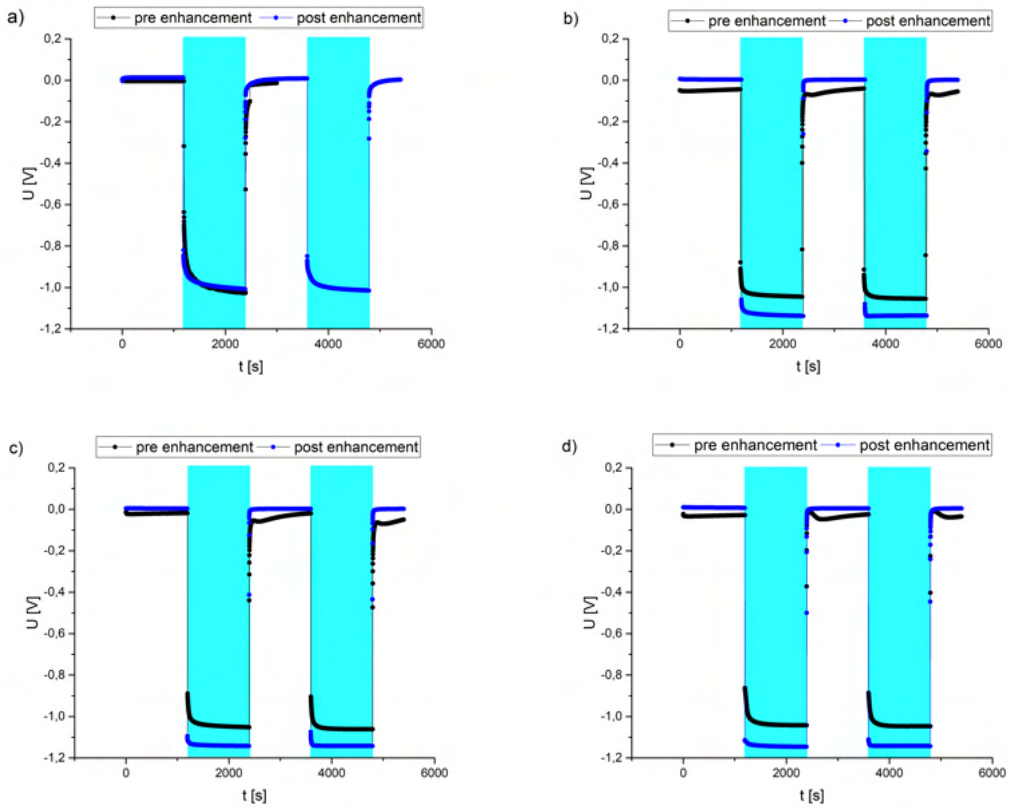

Figure 4.24: Measurements of photovoltage for the first series of SC samples before (black) and after (blue) current enhancement; a) LSCr-1, b) LSCr-2, c) LSCr-3, d) LSCr-4; Sections with UV illumination marked in blue

The only sample not showing a gain in photovoltage but instead a loss (which is negligible and most decidedly owed to measurement uncertainty) is again LSCr-1, although the spectrum still shows higher acuity with faster equilibration for U_{light} and U_{dark} and a direct "drop" to 0.8 V instead of 0.6 V. This difference is clearly a consequence of the counter electrode, but it is unclear if the gain in photovoltage is dependent on reaching a certain "threshold current", which LSCr-1 could have achieved after a massively longer current measurement or if this would have never been possible with a the initial counter electrode.

Table 4.5: Comparison of photovoltage U_{PV} before and after current enhancement; Gain/loss is shown as ΔU

	U_{PV} pre (V)	U_{PV} post (V)	ΔU (mV)
LSCr-1	1.021	1.018	-3
LSCr-2	1.011	1.135	124
LSCr-3	1.038	1.142	104
LSCr-4	1.013	1.142	129

Post illumination EIS measurements

The lasting changes on the sample from current enhancement are also reflected in impedance spectroscopy. While there are still three features to be seen in Figure 4.25 a), the resistances are clearly decreased compared to the initial results before enhancement (shown in Figure 4.22 a) and the MF feature does not show a semicircular appearance anymore.

While the decrease in resistance for LSCr-2 and 3 is about one order of magnitude for both the STO feature and the LF feature (no convincing fit could be found for the MF feature), LSCr-4 clearly differs in this case, with both features showing clearly higher resistances than the other two samples. Here, the overall resistance seems to have only dropped to about one fourth of the initial resistance, which seems counterintuitive, considering LSCr-4 being the sample with by far the longest measurement for current enhancement and the only sample which achieved an equilibrium current I_{eq}.

Nonetheless, the most interesting observation here is in combination with the results for photovoltage: While the resistance of every feature in every sample decreased significantly, the photovoltage actually increased by >100 mV. This means that independent of which feature actually describes the space charge region, the resistance of the space charge region is no clear indication to predict photovoltage, as would be the case in classical pn-junctions (the thicker the depletion zone, the higher the SC resistance and thus the higher the achievable photovoltage).

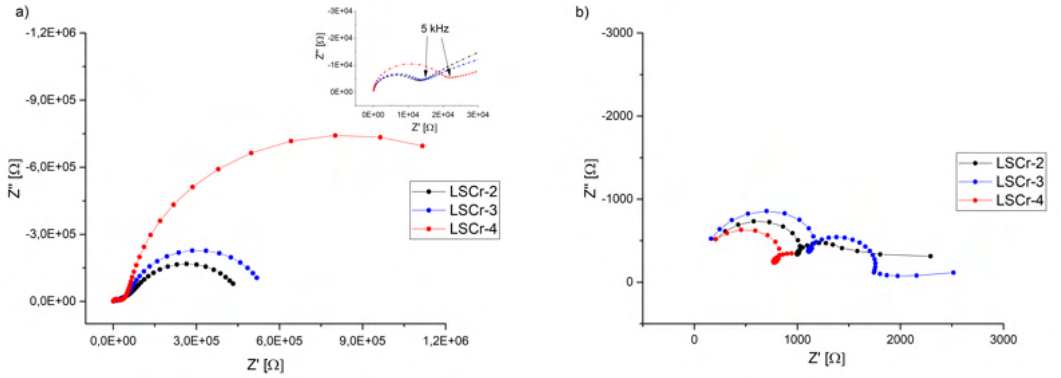

Figure 4.25: Impedance spectroscopy of initial samples after current enhancement; a) dark, b) illuminated

When turning on the UV illumination, as initially, only two features with very low resistances of <1 kΩ could be observed, which is most clearly shown for LSCr-3 in Fig. 4.25 b). Here, the second feature is only partially visible for LSCr-2 and not pictured for LSCr-4 as the EIS measurement was often unable to clearly capture it and would instead produce spectra of no physical meaning. The reason behind this is not fully known but may be linked to the sample undergoing changes on the timescale of the measurement. When performing EIS on the samples, a small but constant AC voltage is applied to the sample, inducing a current. As soon as the UV light is switched on, the current in the sample starts to steadily and rapidly rise as shown before in Figure 4.23 and in more detail in Figure 4.26.
Since every measurement typically takes 8-10 minutes and the whole cycle only lasts for 30 minutes before the light is switched off again, all of the measurements are performed during a section where the current in the sample is steadily rising and the resistance is dropping accordingly (see Fig. 4.26), meaning that the impedance is changing constantly while being measured.

This may have only little effect on measurements in the HF range, where the measurement of a single data point takes only about a second, but can clearly impede results when moving to the MF or LF range, where the measurement of a single data point takes a few minutes.

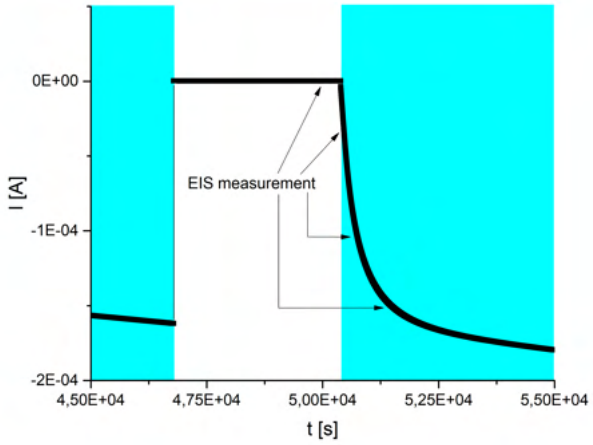

Figure 4.26: Exemplary cutout of the current enhancement in LSCr-3. Since this effect probably also takes place during EIS, measurements performed on the "slope" would be affected by constant changes of resistance; Sections with UV illumination marked in blue

Lastly, while the samples immediately switched from the "dark" to the "light" spectra (Fig. 4.25 a and b) upon being illuminated, this did not happen in the converse case. When the lamp was switched off again, the samples only gradually "recovered" to their initial state, which was most notable in LSCr-4 (see Fig. 4.27). For this reason, the samples were not illuminated for at least 2 hours before EIS measurements, to make sure that the spectra would actually represent the samples' "equilibrium" state.

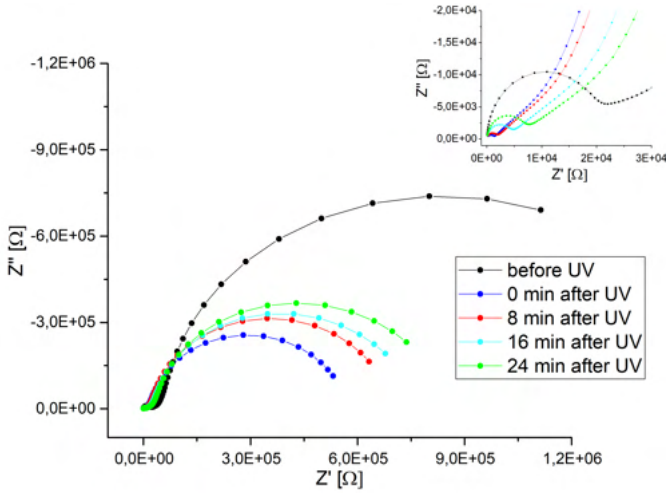

Figure 4.27: Gradual "recovery" of resistance in LSCr-4 after UV light has been switched off again

4.3.4 Electrode material dependent measurements

As stated in Section 3.1.2, additional electrode materials were tested in the samples SC-LSM and SC-Au, since very thin films (10 nm) of Au on STO single crystals have been described to generate significant photovoltage of ca. 1 V [20] and LSM is for one generally similar to LSCr and has also shown during experiments on TF samples to create a photoactive space charge region with STO (Fig. 4.10).

LSM

To start off with, SC-LSM did indeed behave similar to the SC-LSCr samples in every aspect, although there are some interesting differences to be seen. Current measurement was performed in the same way as with SC-LSCr samples, but the intervals, where the sample was illuminated, were extended from 12 h to 18 h to maybe achieve an equilibrium faster, as the sample would not need to "adjust" as often if there were less 1 h interceptions.

As it turned out an equilibrium current I_{eq} was reached after about 90 h, which is considerably faster than LSCr-4 taking around 160 h respectively. Additionally it can be seen in Figure 4.28 that already the initial strong increase achieved ca. 0.4 mA compared to only 0.1 mA for LSCr-3 and 4 and 0.2 mA for LSCr-2. This tendency to higher currents of LSM is also reflected in the I_{eq} value of 1.03 mA compared to 0.77 mA for LSCr-4.

All things considered, LSM seems like the initially better choice for current applications as the maximal achievable current is higher than with LSCr and it can be achieved faster.

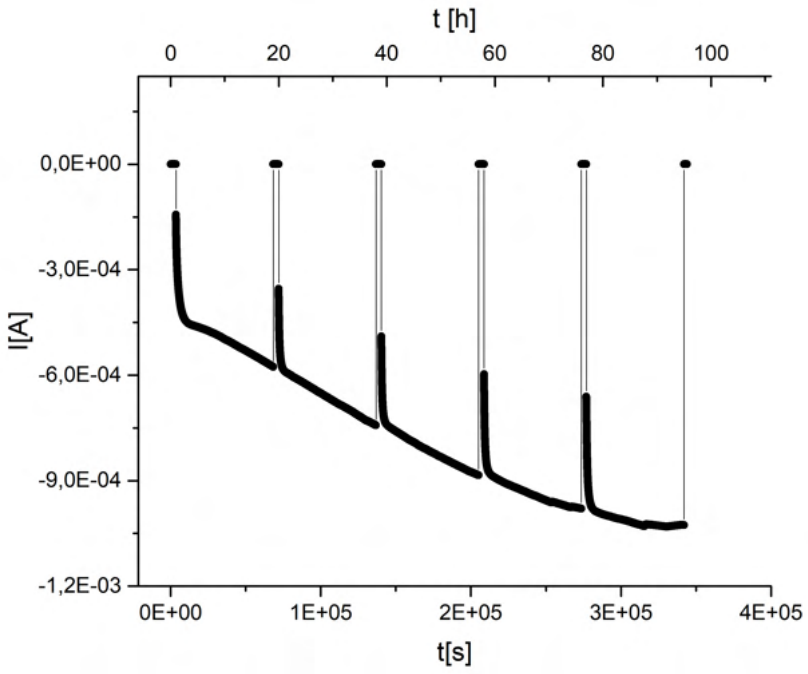

Figure 4.28: Measurement of current enhancement for pristine SC-LSM; illumination intervals were changed from 12 to 18 h

Impedance spectroscopy on the pristine SC-LSM sample in Figure 4.29 a) appears to only show two features: a rather small HF feature of ca 5 kΩ followed by a comparably large LF feature, although with about 1.8 MΩ this is still smaller than the LF features of the LSCr samples (see Table 4.4). With a permittivity of ε_r = 182 and a conductivity of $\sigma = 8.87 \cdot 10^{-6}$ the smaller HF feature again can be clearly attributed to the bulk STO, which leaves the larger feature to represent the space charge region. As with the LSCr samples after current enhancement, here the resistance also "recovers" very slowly after the sample has been illuminated.
Considering illumination, the sample also shows only two features when the UV light is turned on (Fig. 4.29 b), but unlike the SC-LSCr samples here it was possible to always measure the entire spectrum from 1 MHz to 100 mHz, although the last data point of relevance is again at 125 Hz. What can also be seen is a time dependency on especially the HF feature which gradually fades out as the measurement continues. This would make sense when furthermore treating this as attributed to STO as the current enhancement continues and thus the resistance in the STO continually decreases.

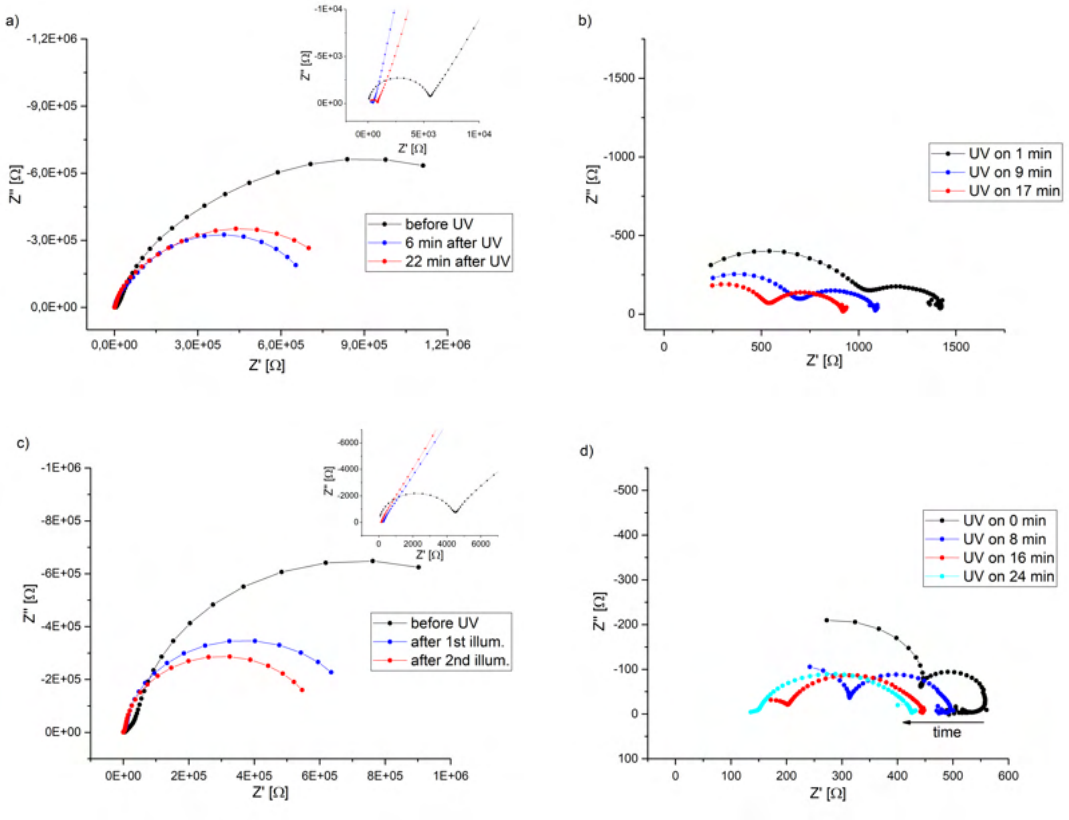

Figure 4.29: Impedance spectra for SC-LSM: a) UV off, before current enhancement, b) UV on, before current enhancement, c) UV off, after current enhancement, d) UV on, after current enhancement

The current enhancement seems to have a lasting effect on the sample similar to LSCr albeit to a smaller extent, as the LF feature indeed decreases in resistance but not tremendously (Fig. 4.29 c). Interestingly, now the MF feature becomes slightly more visible again, indicating that it had also been measured before, but was almost merged completely to the "shoulder" of the LF feature. The resistance recovery after turning off the UV light becomes so slow that repeated illumination in a cycle of 30 min further decreases the resistance as it can not build up fast enough again.

Finally, in Fig. 4.29 d) the spectra of the illuminated sample after current enhancement can be seen, showing again only two features with very small resistances <500 Ω. Here an even more distinct "vanishing" of the STO feature can be observed, which seems to be completely gone after 24 min of illumination.

Figure 4.30 shows the photovoltage generated by the LSM sample before and after current enhancement. Similar to the effects of the enhancement on impedance spectra, a lasting effect akin to SC-LSCr samples can be seen, albeit to a smaller extent. The voltage profile after enhancement seems sharpened and higher photovoltage can be achieved, but this is only very minor compared to the gain of >100 mV in SC-LSCr samples and the complete extinction of battery effects upon switching the light off again and returning to the U_{dark} baseline. Lastly it should be noted that while LSM seems preferable to LSCr in terms of photocurrent, the photovoltage lags behind with only about 0.8 V of maximum voltage can be achieved compared to over 1.1 V when LSCr is used as working electrode.

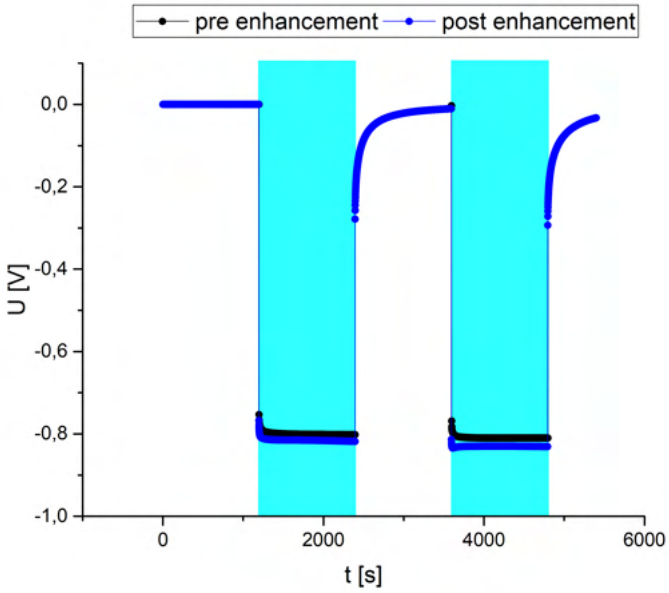

Figure 4.30: Photovoltage of SC-LSM before and after current enhancement; Sections with UV illumination marked in blue

Au

While LSM showed promising results and was still used later on for temperature- and annealing-dependent measurements (see Section 4.3.6), unfortunately the same can not be said for the sample using sputtered gold as working electrode.

It can easily be seen in Figure 4.31 a) that the sample seemed to only produce very minor photovoltage in the range of single-digit millivolts followed by opposing battery voltage of about 50 mV, ultimately making this a far cry from the reported 1 V of photovoltage despite the same preparation process. This result also did not change after removing the electrodes on both sides by washing them off in EtOH and preparing the sample again in the same fashion.

The sample's impedance spectra are depicted in Figure 4.31 b) and show two features with massive resistances between 10 and 100 MΩ without illumination. While they do clearly decrease under illumination, no feature completely collapses (similarly to TF samples) and the HF feature's resistance - albeit minor in comparison - still shows a value of nearly 1 MΩ,
The very minor photovoltage measured on the sample led to the decision that no significant current could be expected and no following measurements would be performed on SC-Au, as the sample clearly did not meet the expectations.

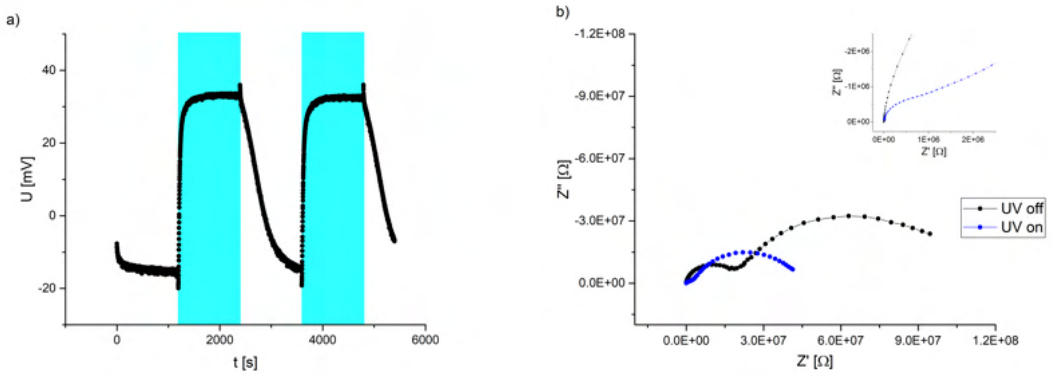

Figure 4.31: a) Voltage measurement of SC-Au, sections with UV illumination marked in blue; b) Impedance spectra of SC-Au with and without UV illumination

The sample also showed a distinct change in colour across the entire illuminated surface, which can be seen in Figure 4.32. While the part of the sample that was clamped behind the WE contact as shown in Figure 3.4 is still typically golden, the illuminated part is significantly darkened and appears more green, indicating that some kind of reaction seems to takes place which leads to an irreversible degradation of the sample. This also happened both times the sample was prepared and measured.

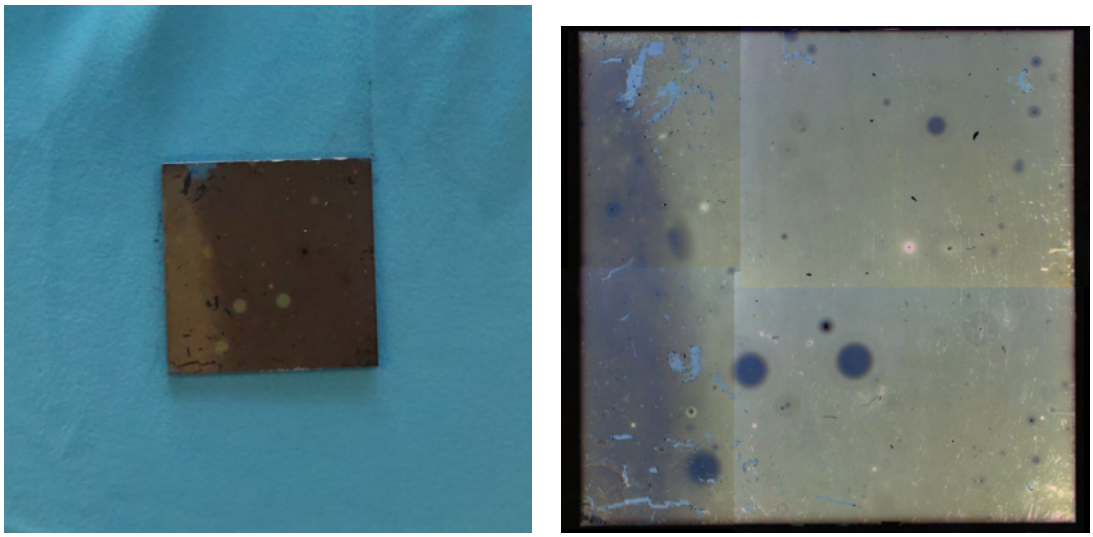

Figure 4.32: Normal camera picture (lhs) and microscopic image (rhs) of the SC-Au sample after measurements were performed

4.3.5 The role of stoichiometry polarization

Stoichiometry polarization, i.e. the enrichment of ions or vacancies inside a crystal at one side caused by an external electrical field, has been suspected to be the main reason behind the current enhancement in $SrTiO_3$.

With oxygen vacancies being the predominantly mobile ionic species in STO in the intermediate temperature regime as discussed in Section 2.3.1, it seems obvious to assume that stoichiometry polarization would be mainly dependent on their mobility. Since the mobility is linked to the diffusion coefficient D, and diffusion processes typically show a linear dependency on the square root of time (Equations (4.6) and (4.7)), it was attempted to show such a dependency for LSCr-4. To do this, two data points of every illumination cycle shown in Figure 4.33 a) were taken and plotted against $\sqrt{t}$ (Fig. 4.33 b).

$$D = \frac{\langle x^2 \rangle}{2t} \tag{4.6}$$

$$x \sim \sqrt{t} \tag{4.7}$$

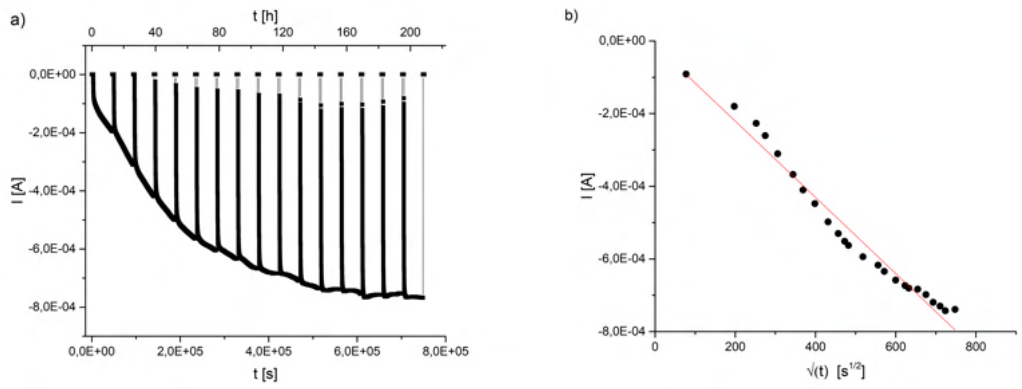

Figure 4.33: a) Current enhancement measurement for LSCr-4, b) Exemplary data points from (a) plotted against $\sqrt{t}$ with linear regression line

While the result, depicted in Figure 4.33 b), shows a high coefficient of determination (R^2 = 0.974), the residues are quite obviously not normally distributed and the data points show a non-linear trend. This indicates that a linear dependency of the current enhancement on the square root of time and thus on stoichiometry polarization is probably not constituted.

Since this observation is not entirely conclusive, further attempts were made to explain the role of stoichiometry polarization by figuring out the approximate time it would take the oxygen vacancies to pass through the entire STO single crystal at a given (photo)voltage of 1 V dropping at the internal resistance of STO. This time can easily be calculated from the crystal's thickness d and the speed v at which oxygen vacancies pass through the crystal, which is in turn dependent on the vacancies' mobility $u_{V_O^{\bullet\bullet}}$ and the electric field E through Equation (4.8).

Combining this with Equation (4.9), we arrive at Equation (4.10) allowing the calculation of the required time t through the crystal's thickness, the applied voltage and the mobility of oxygen vacancies. Since the crystal's thickness is known to be d = 0.5 mm and the voltage is known to be about 1 V, only the mobility of vacancies has to be evaluated.

$$v = u_{V_O^{\bullet\bullet}} \cdot E = \frac{d}{t} \tag{4.8}$$

$$E = \frac{U}{d} \tag{4.9}$$

$$t = \frac{d^2}{u_{V_O^{\bullet\bullet}} \cdot U} \tag{4.10}$$

This is done through Equation (4.11) with values of $u_0 = 149\ \mathrm{cm^2 \cdot K \cdot (V \cdot s)^{-1}}$ and $E_A = 0.62$ eV, all according to *Maier and Russell* [128].

$$u_{V_O^{\bullet\bullet}}(T) = \frac{u_0}{T} \cdot \exp\left(-\frac{E_A}{k_B T}\right) \tag{4.11}$$

For a given temperature T of 350 °C (623 K), the time for an oxygen vacancy to pass through the entire STO single crystal would thus be 1080 s for the SC-LSCr samples and 1350 s for the LSM sample (as only 0.8 V were achieved here). This is clearly far from the approximately 600 000 s it actually took LSCr-4 and 300 000 s it took SC-LSM to reach an equilibrium and further indicates that stoichiometry polarization might actually not be relevant for the long-time development of photocurrent.

Interestingly enough, the timescale of ca. 1000 s fits relatively well to the initial strong increase of current upon every UV illumination before the behaviour changes into the long-time trend (shown in Figure 4.34), which takes around 1300 to 2100 s for every sample. This would indicate that stoichiometry polarization is reset every time the illumination stops (as the voltage vanishes) and has to be built up again every time the sample is illuminated, posing an impediment of 20-40 min should the cell be put into operation, even if I_{eq} has already been reached from the start.

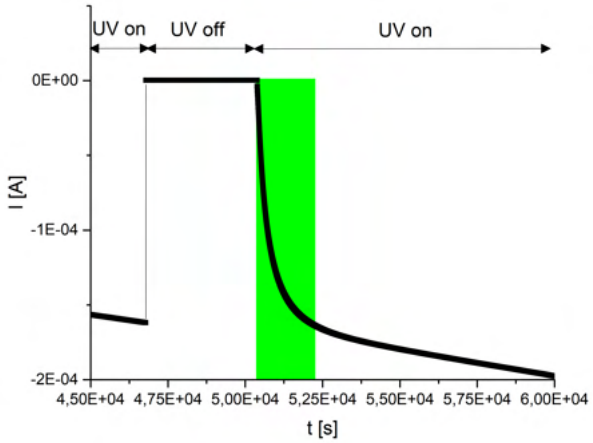

Figure 4.34: Exemplary cutout of current enhancement in LSCr-3. The approximate region of initially strong increase upon UV illumination is marked in green

4.3.6 Temperature dependent measurements

These measurements were mostly conducted on samples after they had already been annealed at 600 °C which actually led to results that differed from what was to be expected of pristine samples. Thus, there will first be a discussion about the permanent changes that were introduced in the samples through high temperature annealing before moving on to the role of intermediate temperature changes (300-400 °C) on the samples' behaviour.

General effects of annealing

As the current enhancement turned out to be permanent (or at least remanent over a large timescale), it was tried to reset this to perform additional measurements of the full enhancement process on the same sample, especially at different temperatures.
Since the reason for the enhancement was initially believed to be related to stoichiometry polarization, the method of choice was high-temperature annealing, as this had already shown in earlier works [17] to be effective when trying to undo the effects of electrocoloration/stoichiometry polarization.

As it turned out, some of the changes in the samples could indeed be reverted to some degree, but generally speaking the annealing process did not exactly reset the samples to their pristine state but instead introduced additional, permanent changes (that went beyond signs of collector grid degradation of some samples, described in Section 4.1.2).

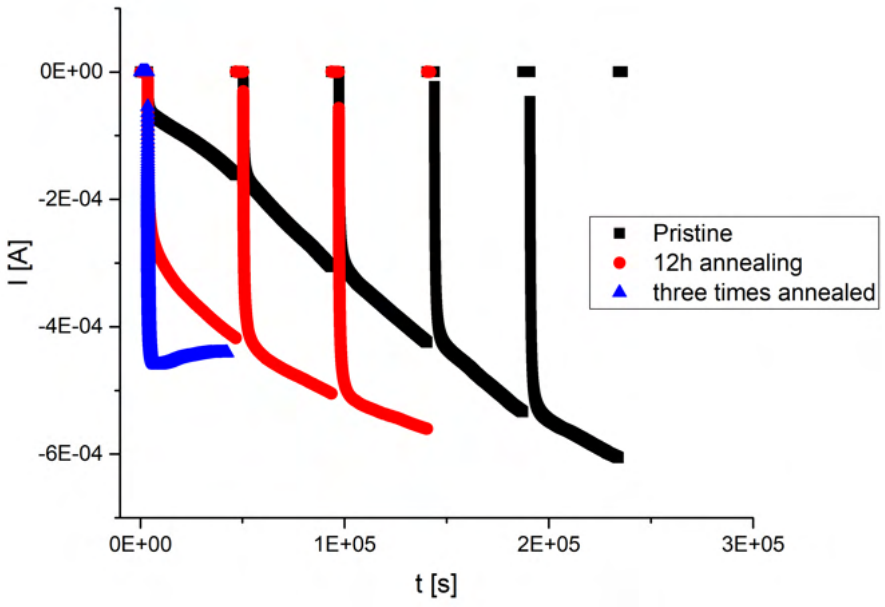

Figure 4.35: Current measurement of sample LSCr-3. Pristine sample is shown in black, sample after the first annealing (12 h) shown in red and sample after the third annealing process (12 + 36 + 24 h) shown in blue

When comparing the three measurements on LSCr-3 depicted in Figure 4.35 to each other, there are some things that are easily apparent. With the pristine sample having achieved a final current value of about 0.6 mA, it can be seen that while the first annealing process did reset the current after the initial strong increase somewhat, this was clearly not a full reset. Since the annealed sample behaved during its first illumination cycle very similar to the pristine sample during the third cycle it was thus assumed that 12 h had simply not been enough annealing time, which led to the decision of additional annealing on LSCr-3 paired with longer annealing times on this sample as well as LSCr-1 (which was first equipped with a Pt-CE instead of the initial Pt-YSZ-CE), 2, 4 and SC-LSM.
In the end, repeated and persistent annealing did not lead to a full reset of the current but instead to a substantial change of the overall behaviour, as a stable equilibrium current I_{eq} was apparently reached after just one cycle of 12 h, but this was much lower than the current achieved with the pristine sample and only about half the pristine sample's presumed I_{eq} of 0.77 mA (from the LSCr-4 measurement). And it can indeed be seen that already the first annealing process did show a similar trend, as the initially achieved current is notably higher than in the pristine sample, but the curve also starts to flatten immediately, whereas the pristine sample still shows a continued increase of photocurrent.
To get comparable results, it was therefore decided to have every sample annealed to the point, where an equilibrium current would be achieved during only one illumination cycle of 12 to 18 h, as anything between the pristine and the fully annealed samples was considered a transient state. Still, as explained in Section 4.1.2, LSCr-4 was never measured in its annealed state

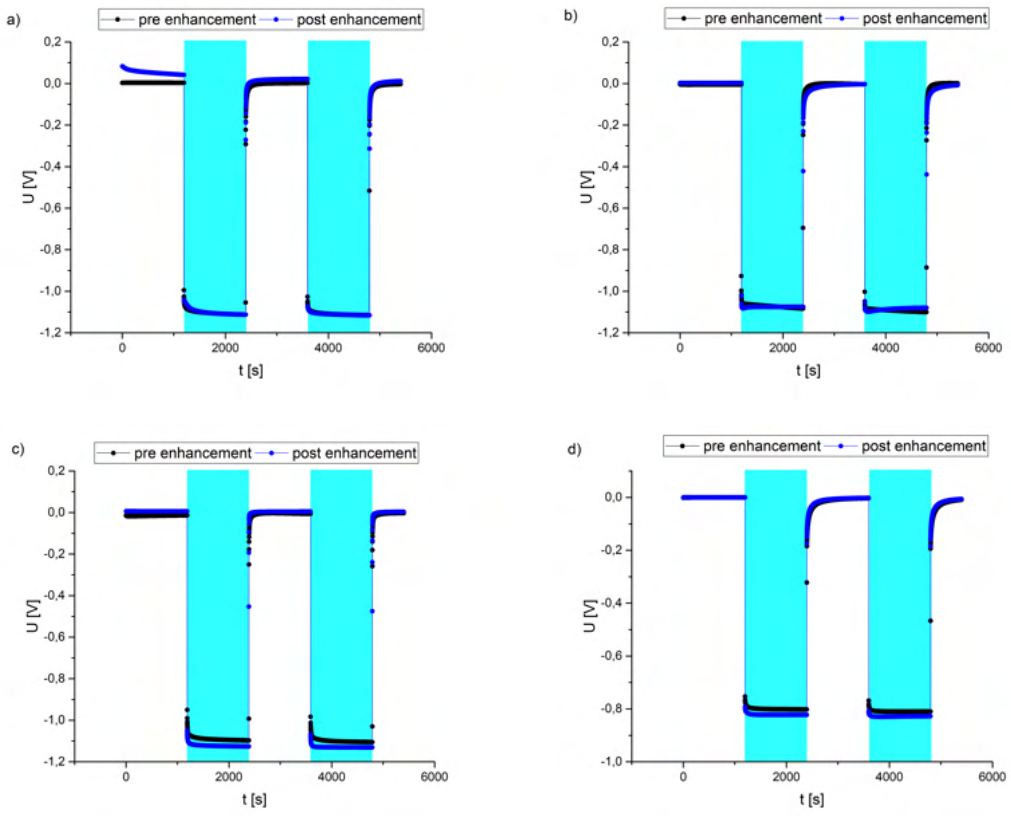

Figure 4.36: Measurements of photovoltage at 350 °C after annealing; a) LSCr-1 (48 h annealed), b) LSCr-2 (36 h annealed), c) LSCr-3 (12+36+24 h annealed), d) SC-LSM (48 h annealed)

Moving on to the effects of annealing on photovoltage depicted in Figure 4.36, it can clearly be seen that this did not lead to any apparent changes. All of the samples still showed the same behaviour as they did after current enhancement was performed on the pristine samples with the LSCr-samples (a, b, c) achieving ca. 1.1 V of photovoltage and the LSM-sample achieving 0.8 V.
Also when photovoltage was measured again after performing the current measurement (depicted in blue in Fig. 4.36), no significant change of photovoltage could be observed. There was only a slight initial offset in U_{dark} for LSCr-1 and a minimal gain in photovoltage for LSCr-3 (c) and SC-LSM (d), though this should only be owed to measurement uncertainty. This further supports the idea that the first measurements on the freshly prepared samples shown in Figure 4.21 were simply not fully equilibrated. Once an equilibrium is reached, the photovoltage does not change any further.

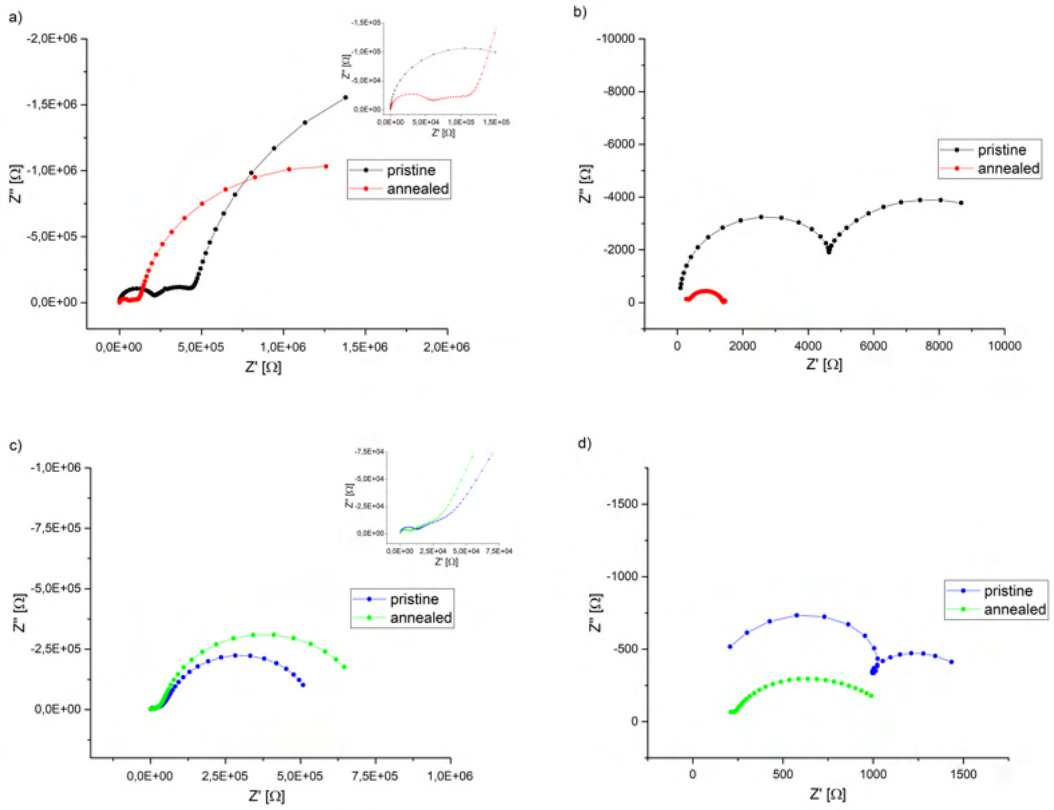

Figure 4.37: Comparison of EIS Measurements of LSCr-2 at 350 °C before and after annealing; a) before further current enhancement, UV off; b) before further current enhancement, UV on; c) after further current enhancement, UV off; d) after further current enhancement, UV on

Impedance spectroscopy after annealing showed expectable results that are generally in line with the observations made for voltage and current measurements. Figure 4.37 depicts the exemplary measurements for LSCr-2, as all samples were very similar in behaviour. In (a) it can be seen that a slight "recovery" of the initial features' resistances took place, but the pristine state could not be reached again (similar to current measurements). After further enhancement takes place (c), the dark spectra do pretty much show the same behaviour as the pristine samples with the differences in resistance owed to uncertainty.

Under illumination (b, d) all samples could now be fully measured and showed the same behaviour as the pristine SC-LSM sample with features in the range of 1 kΩ and the HF feature gradually vanishing over time, which is in line with literature [20]. This was the same before (b) and after (d) further current enhancement. After annealing none of the spectra showed significant difference between LSCr and LSM in use for the working electrode.

Temperature dependency of I_{eq}

As stated above, these measurements were generally only performed on fully annealed samples with the exception of SC-LSM, which was prepared after the effects of annealing were already known. Owed to the still significant time consumption of especially current measurements - even though equilibrium currents could be reached much faster after annealing - the samples were only measured at three different temperatures: 300, 350 and 400 °C. Measurements were always performed by first measuring the equilibrium current at 350 °C (together with voltage measurements and EIS) to make sure that no other measurement would affect this and possibly distort the comparison to the pristine samples, as those were only measured at 350°C. This was followed by the measurement at 300 °C and lastly 400 °C.

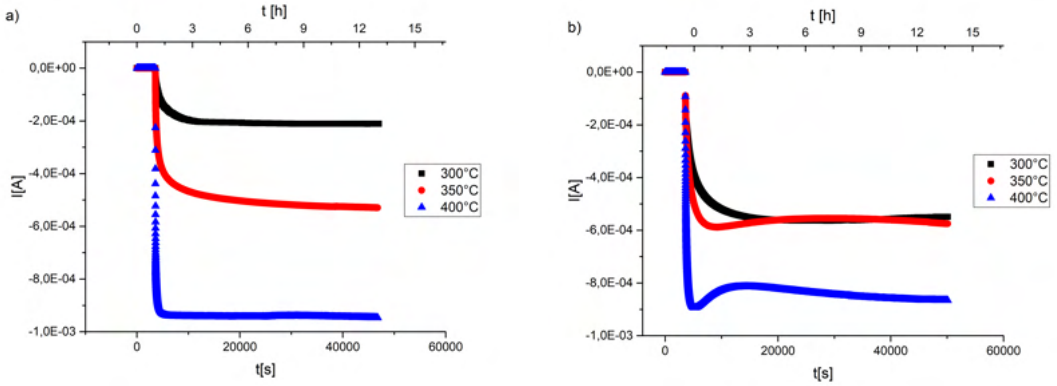

Figure 4.38: Current measurement until an equilibrium was reached in annealed samples: a) LSCr-2 (exemplary), b) SC-LSM

From Figure 4.38 a) it can directly be seen that the measurements of the LSCr series showed expectable results with the equilibrium current steadily rising with temperature. It can be seen in (a) that the equilibration took the longest at 350 °C and that nearly no equilibration had to take place at 400° C which is probably an effect of the order of measurements.
SC-LSM (b) on the other hand showed a more interesting behaviour with the measurements at 300 and 350 °C resulting in more or less the same equilibrium current. Additionally, the measurements seemed to always show a "dip" followed by a small raise before the equilibrium was reached. This seems to be a kinetic effect, as it appears the fastest and most distinct at 400 °C whereas at 300 °C the measurement is still traversing the "dip" after 13 h.

When comparing all of the current measurements (Figure 4.39, it can be seen that all of the SC-LSCr samples were very similar in overall behaviour and only slightly diverged from each other. The dependency of I_{eq} seems almost linear in these samples but a stronger increase in the 350-400 °C range compared to the 300-350 °C range can be made out for LSCr-2 and 3.

This is although relatively minor compared to SC-LSM, where practically no increase in current between 300 and 350 °C took place. While LSM shows higher currents at low temperatures, this advantage over LSCr becomes negligible at 400 °C, as long as fully annealed samples are used. The discrepancy between LSM and LSCr in pristine samples of about 0.2 mA is albeit much larger, as has already been shown in the discussion of initial current measurements. It should also be noted that the overall behaviour of SC-LSM did not change through annealing with the sample consequently achieving equilibrium currents that were ca. 0.4 mA higher in its pristine state compared to its annealed state. No such statement can be made for LSCr since there were no measurements performed on pristine samples at 300 and 400 °C.

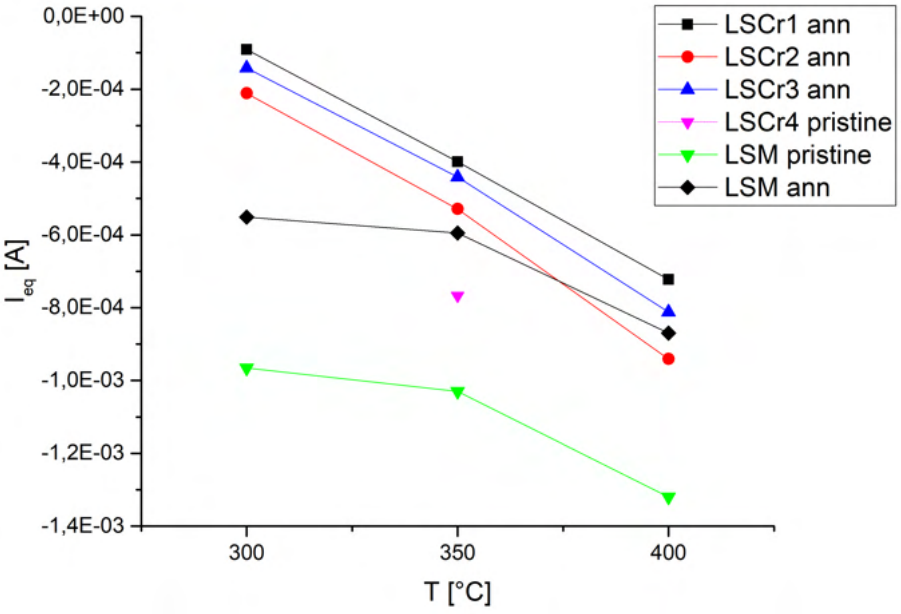

Figure 4.39: Comparison of all measurements for I_{eq}

Temperature dependency of photovoltage

As with current measurements, the overall dependency of photovoltage on the temperature showed the expected result with voltage decreasing as the temperature rises.

As depicted in Figure 4.40 a), photovoltage of annealed LSCr-samples decreased from an absolute value of 1.2 V at 300 °C to about 1 V in a relatively linear fashion. While further current enhancement on annealed samples left the photovoltage more or less unaltered at 350 and 400 °C, there was still a notable increase of ca. 100 mV to be seen at 300 °C for all three measured samples of the SC-LSCr series. This is surprising as the actual equilibration of current had already been performed at 350 °C before the first PV measurement at 300 °C (marked in black in Fig. 4.40). Thus it was actually expected that no further changes in the sample would happen by measuring the current at 300 and 400 °C.

The measurement of SC-LSM (b) did not show any surprising results - with overall temperature dependency similar to LSCr - and no major increase of photovoltage was observed (although this was also never observed in the pristine sample in the first place). In fact, there was even a slight decrease in voltage at 400 °C, which is most decidedly owed to measurement uncertainty. While Figure 4.40 b) only shows the results of the annealed SC-LSM sample, these results did not notably differ from the pristine sample (cf. Fig. 4.30 and Fig. 4.36 at 350°C).

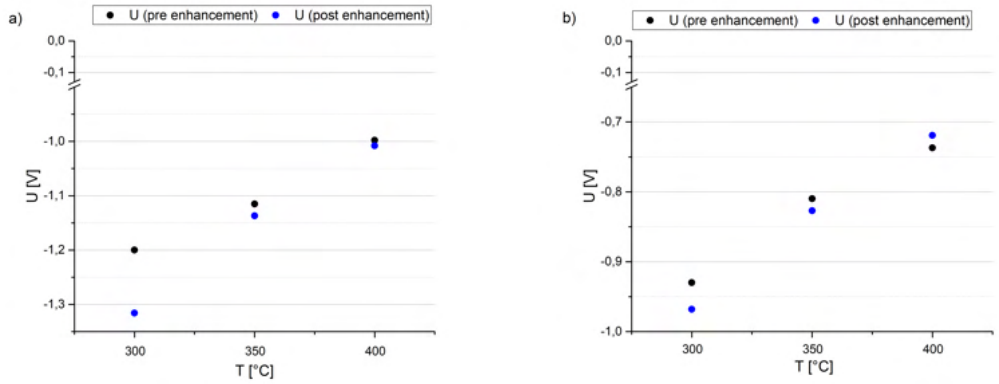

Figure 4.40: Results of PV measurements on annealed samples: a) LSCr-1 (exemplary), b) SC-LSM

Temperature dependent impedance spectroscopy

Akin to temperature dependent measurements of equilibrium current and photovoltage, EIS measurements for different temperatures were in general very consistent with theory. What can be seen in Figure 4.41 is that generally speaking the resistances of all features decrease as expected with rising temperature and (as already discussed) after current enhancement. The only notable oddity among these measurements is that the STO feature of LSM (b) has a larger resistance at 350 °C than at 300 °C.

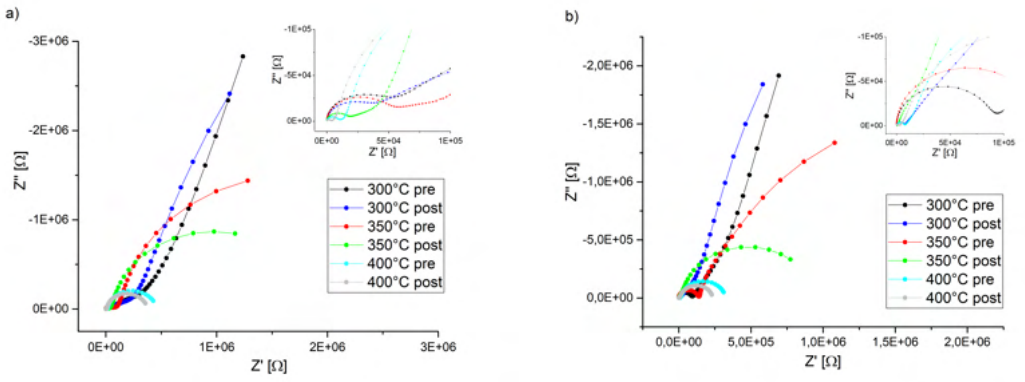

Figure 4.41: Dark spectra of EIS measurements on annealed samples before and after further current enhancement: a) LSCr-1 (exemplary), b) SC-LSM

Influence of the CE on the impedance spectra

The final experiment conducted on the initial SC-LSCr samples after annealing dealt with the influence of the counter electrode on the MF feature in the impedance spectra. Earlier works [19,20], while attributing the HF feature to bulk STO and the LF feature to the STO/LSCr space charge region, suspected the MF feature to be caused by the counter electrode material in use. This idea seemed odd as during the course of this work, the MF feature was always present and did not show any direct relation to the CE in use. First, the TF samples with symmetrical electrode configuration still did prominently show an MF feature in both instances (LSCr/LSCr and LSM/LSM), even though there is no clear distinction between WE and CE in this case. On the other hand, the visibility and overall behaviour of this feature did differ notably between the SC-samples using LSCr as WE and the sample using LSM as WE, although in all cases the CE was porous Pt.

As the resistance of the MF feature did notably decrease during current enhancement and partially recover during annealing, the following idea came to mind: Should the MF feature indeed be caused by the counter electrode, then the MF feature's resistance should return to its pristine state, if an annealed sample is prepared with a fresh CE (with small deviations reserved due to measurement uncertainty).

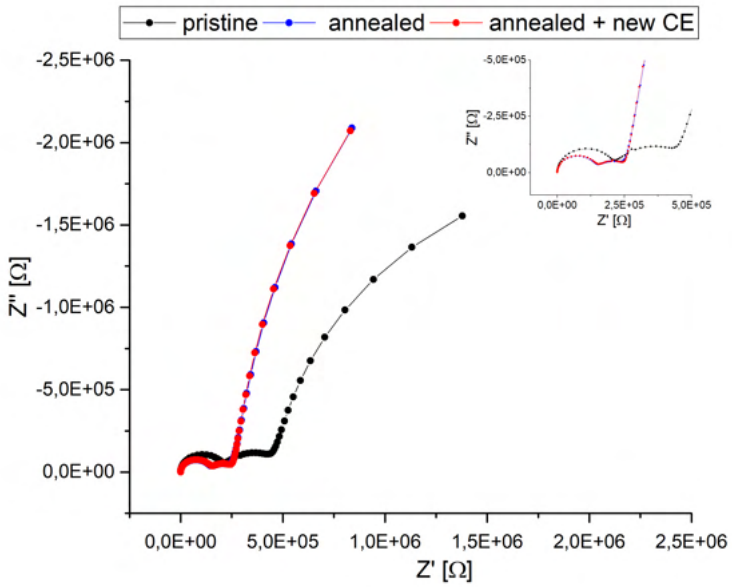

Figure 4.42: Dark spectra of LSCr-3 in fully annealed state with initial (blue) and freshly prepared Pt-CE (red) compared to the pristine sample (black)

Figure 4.42 shows the dark spectra of fully annealed LSCr-3 compared to its pristine state and it can be seen that the resistances of the HF and MF feature in the annealed state are clearly smaller than in the pristine state (although this is the only example showing the LF feature to be larger after annealing than in the pristine state). Now the sample was taken out of the measurement setup, deposited in EtOH and sonicated to wash off the used CE. Afterwards, a new Pt-CE was brushed and dried onto the sample in the same fashion as before, followed by the sample being placed in the measurement apparatus again and the spectrum shown in blue in Figure 4.42 was recorded.

It is evident that despite the fact that the new CE could have shown absolutely no signs of degradation, the MF feature's resistance did not recover to its pristine state. In fact, the spectrum clearly did not change in the slightest despite the sample being taken out of and placed into the apparatus again, not to mention the treatment in between. The high fidelity of these measurements also shows that the difference between the HF feature in the blue and the black spectrum is surely not owed to uncertainty but instead represents the actual state of the sample.

This means that even if the CE should indeed be causative for the MF feature to some degree, this feature would actually represent an effect introduced by the CE into the bulk STO that is located entirely within STO rather than representing the CE itself.

Final observations on the effects of temperature and annealing

While the sample using LSM did indeed achieve a higher equilibrium current than the respective LSCr sample in lab air (ca 1 mA vs 0.8 mA) this might not be fully attributed to the change in material but instead at least partially to the annealing effect, where prolonged exhibition of the samples to temperatures of 600 °C and above leads to overall lower achievable equilibrium currents. During deposition of LSCr, the STO sample is heated to 700 °C for at least 15 min, while the deposition of LSM only needs temperatures of 550 °C (cf. Tab. 3.2 and 3.4).
This difference in sample preparation shows that the SC-LSM sample was never equilibrated above 550 °C before the measurement of current enhancement took place and could thus be able to achieve a higher photocurrent. Still, using LSM also leads to the equilibrium current being reached faster, which is most definitely inherent to the material itself.

On a final note, the parameters used for sample preparation might also be the reason for the conductivity of the STO being very similar for all instances of SC-LSCr samples (see Table 4.4) but diverging by a factor of about 2 to 3 when compared to the SC-LSM sample (Section 4.3.4). Using different temperatures and ambient oxygen pressures seems to equilibrate the STO in different states, which might become "frozen in" upon rapid cooling of the samples, which was generally done with a slope of 15 K/min.

4.3.7 p(O_2)-dependent measurements

The final set of experiments on SC samples consisted in the measurement of samples in atmospheres with varying O_2-content to describe its influence on the overall behaviour of photocurrent and -voltage and how the highest achievable values in both instances are affected.
Since current enhancement permanently changed the initial samples and annealing introduced further changes instead of undoing those caused by current enhancement, new samples had to be prepared as the measurements were to be conducted on pristine samples (as described in Section 3.3.5). As obviously only one current measurement could be conducted on every sample this raised the necessity of preparing one sample for each atmospheric composition that was to be measured. This approach was of course linked to the risk of results varying due to a possibly broad sample distribution, but as LSCr-1 through 4 already showed very comparable results and high reproducibility, this risk was considered a minor issue.

Current measurements

Unlike the measurements of temperature dependency, the results of p(O_2)-dependency showed highly surprising results, which are shown in Figure 4.43. When comparing the three samples (d) it is immediately obvious that p(O_2) and maximum photocurrent are not simply connected, but instead there seems to be a local maximum somewhere between 1 and 100 % O_2-content, as the current is highest in synthetic air and shows lower values for 1 and 100 %.

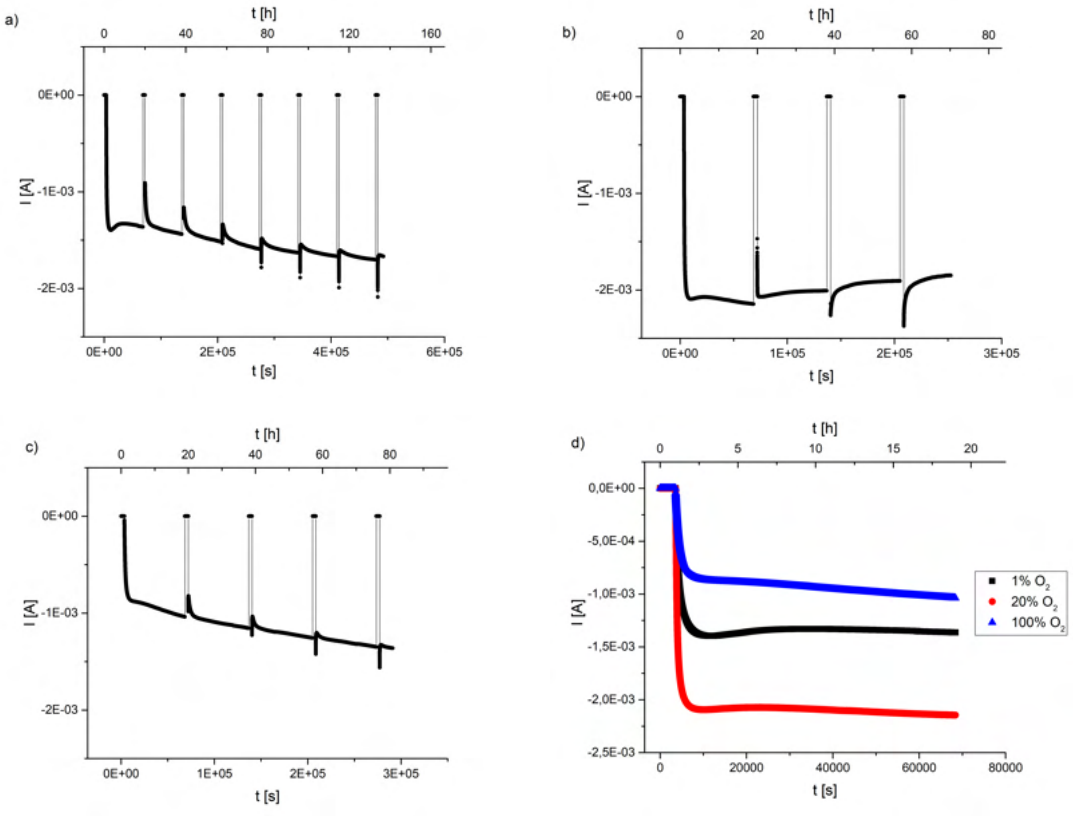

Figure 4.43: p(O_2)-dependent measurements of samples LSCr-5, 6 and 7; a) LSCr-6, 1 % O_2 atmosphere; b) LSCr-7, 20 % O_2 atmosphere (syn. air); c) LSCr-5, 100 % O_2 atmosphere; d) comparison of illumination cycle (18 h)

But what is even more interesting here are the absolute values of current achieved in every case: With a direct initial increase to about 1 mA for LSCr-6 at high $p(O_2)$ (c), 1.4 mA for LSCr-5 at low $p(O_2)$ (a) and a full 2.1 mA for LSCr-7 in synthetic air (b), these samples show an overall massive increase in photocurrent when compared to the samples measured in lab air.

Moreover, while it took LSCr-4 multiple days to achieve 0.77 mA, these samples reach a nearly consistent current maximum after about 1 hour, making them comparable to annealed samples in this regard, although with a clear increase in photocurrent instead of a decrease. The overall similarity in behaviour shown in (d) to annealed samples also suggests the possibility that annealed samples would also still show further current enhancement if measured for an even longer time akin to LSCr-5, 6 and 7, making the I_{eq} on these samples only a quasi-equilibrium state. This would although most decidedly only be a very minor increase and current value >0.6 mA would probably take weeks to achieve if it can can even be achieved at all.
Finally, it can be seen across the board that apparently stoichiometry polarization does not fully reset anymore after just one hour of no illumination, as the time it takes for the sample to reach the quasi-equilibrium becomes increasingly shortened, even resulting in initial current spikes during later illumination cycles. However, a relaxation of stoichiometry polarization on longer timescales is still possible.

All things considered, while the direct correlation between $p(O_2)$ and the maximum photocurrent can not be fully explained through these measurements, it is evidently shown that a clear influence is given. This is although less interesting than the significant difference between measurements in lab air and in synthetic atmospheres, where the long-time current enhancement effect seems to be nearly completely eliminated and overall higher photocurrents can be reached. This indicates that, what was originally considered an enhancement process inherent to STO, actually seems to be more of an initial impediment, which is caused by either moisture or organic contamination in natural air and is slowly counteracted by the PV cell.

Measurements of photovoltage

Following photocurrent, the measurements of photovoltage also did show some interesting differences when compared to LSCr-1 through 4. While the first set of samples initially only achieved about 1 V of photovoltage and a comparably slow equilibration of U_{dark} (cf. Fig. 4.21), which was improved only after the current enhancement took place, the samples measured in synthetic atmosphere achieved ca. 1.1 V and fast equilibration in both directions right from the start (see Figure 4.44 a) to c)). This further indicates that what has already been described as an initial impediment for the cells actually stems from the composition of natural lab air.

When comparing the results of PV measurements in synthetic atmosphere to each other, it can be seen in d) that there seems to be an increase in photovoltage with increasing O_2-content before and after enhancement. This increase is although very minor, amounting to just 30 mV before enhancement and might just be owed to convenient sample distribution. It is slightly higher after the current enhancement took place, now amounting to ca. 80 mV because LSCr-6 slightly decreases in photovoltage. As with the other occurrences of this phenomenon this is attributed to uncertainty.

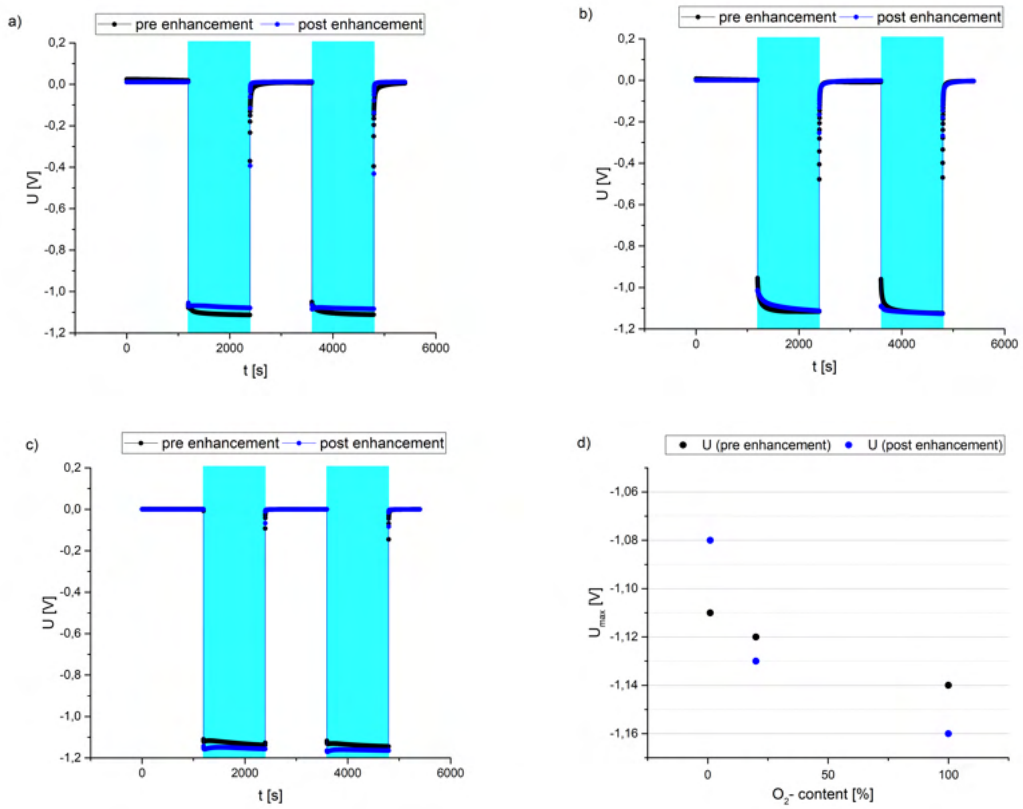

Figure 4.44: p(O_2)-dependent measurements of photovoltage: a) LSCr-6, 1 % O_2 atmosphere; b) LSCr-7, 20 % O_2 atmosphere (syn. air); c) LSCr-5, 100 % O_2 atmosphere; d) comparison of maximum U_{PV} achieved for every sample

EIS measurements

To conclude this chapter, the results of impedance spectroscopy on LSCr-5 to 7 presented in Figure 4.45 will be discussed. It can be seen in a) that there is a clear dependency of the resistance in the samples on the atmospheric O_2 content, with the LF feature's resistance decreasing as the oxygen content increases. The resistance of the STO bulk feature shows dependency similar to current measurements, with the highest resistance to be seen at 20 %, followed by 1 % and finally 100 %. This might again just be convenient sample distribution but it also raises the possibility of predicting photocurrent from initial STO resistance, akin to predicting photovoltage from space charge resistance in classical pn-junctions. This is especially interesting with STO being generally a hole-conducting material, as one would expect that in the given oxygen regime the hole concentration [$h^\bullet$] would change with $p_{O_2}^{1/4}$ and thus R_{STO} would steadily decline with $p_{O_2}^{-1/4}$ [102], provided it equilibrates sufficiently fast at the given temperature, which is probably not the case.
Furthermore, while the STO feature has very similar resistance values between LSCr-7 and the initial samples LSCr-2 to 4 (ca. 170 kΩ) and the resistance of the LF feature differs by a factor of ca 2 (1.8 MΩ vs 3-5 MΩ), the MF feature that is prominently seen under lab air seems to vanish completely. Only in pure oxygen a small "shoulder" can be seen next to the LF feature. Clearly, only the surrounding atmosphere was changed between the samples, further supporting the claim that the MF feature has no direct connection to the counter electrode.

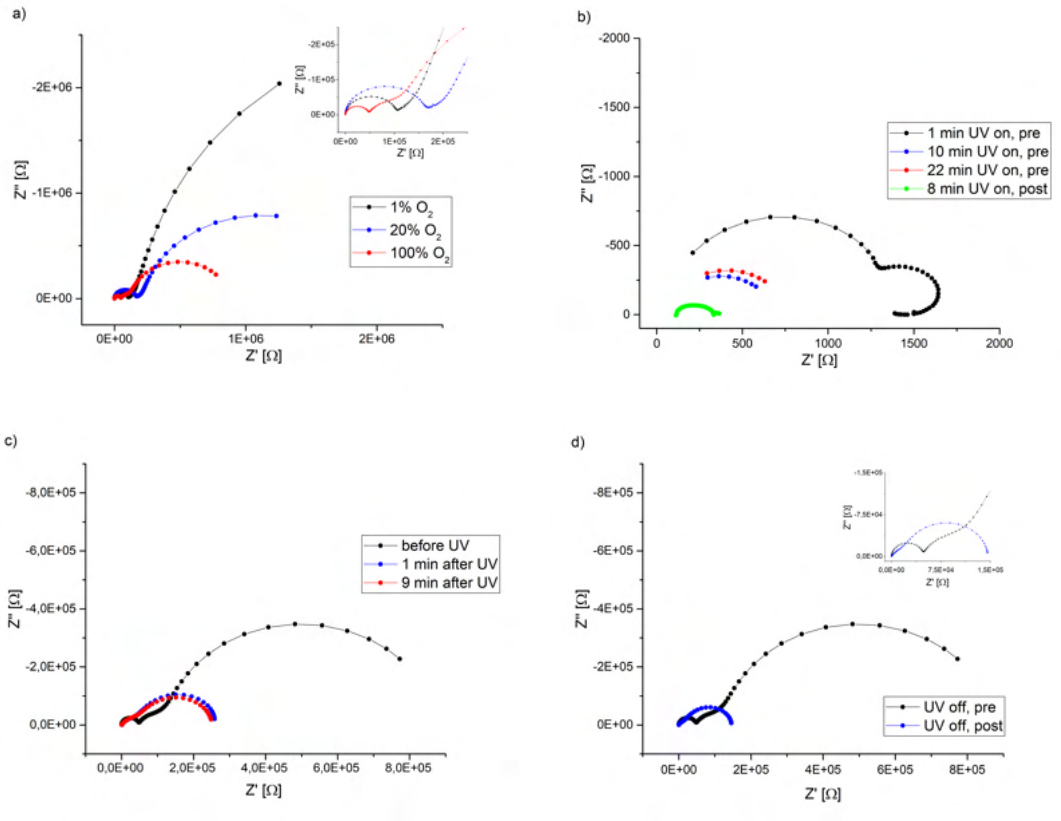

Figure 4.45: EIS measurements on final samples: a) dependency of dark spectra of pristine samples on atmospherical O_2-content, b) changes in illuminated spectra over time and after current enhancement, c) changes of dark spectra upon illumination (LSCr-5), d) changes in dark spectra upon current enhancement (LSCr-5)

The samples upon being illuminated (b) showed the exact same behaviour as the first LSCr-sample series, with initially two features in the low kΩ range to be seen, but only HF data being processed upon repeated measurements. After current enhancement had taken place only a very small elongated feature with a resistance of ca 200 kΩ remains, as the arc representing STO seems to have vanished completely. This is also in line with earlier observations. As the stoichiometry polarization is not able to properly "recover", the resistance switch upon illumination happens instantly, making the resistance afterwards consistent enough to be measured consequently.

Figure 4.45 c) exemplary shows the lasting changes introduced in the dark spectra by illumination (LSCr-5 was chosen as example since it was the only sample initially showing three features). The resistances decrease significantly with the STO feature becoming unrecognizably small and also do not seem to make any discernible recovery during the period of no illumination.
Lastly, comparing the initial spectrum to the spectrum after current enhancement (d), it can be seen that the overall resistance declines even further upon current enhancement which was to be expected from all of the previous EIS measurements on SC samples.

5 Conclusion and Outlook

Based on all measurements of this thesis, it is obvious that at least when following the sample preparation given by this work, samples with single crystalline application of $SrTiO_3$ are significantly better in every aspect concerning photovoltaic properties when compared to thin film applications. While TF samples did generate measurable photovoltage, this was negligibly small compared to the photovoltage generated by SC samples and showed only very limited reproducibility and reliability.

The overall problems encountered with thin film applications are listed in the following:

- Overall very low photovoltages: The photovoltage of all samples was in the range of millivolts with only three samples - STO with no Fe-doping and 0, 7 and 10 % Sr-compensation in the target respectively - being able to generate photovoltage above 100 mV. Any and all of the other samples were clearly below this mark.

- Long equilibration times: Despite using illumination cycles of 2 h, in many cases no constant voltage could be achieved during this time, with either U_{light} or U_{dark} still slowly adjusting when the illumination was switched off or on again, respectively. Furthermore, many of the samples showed a long time drifting effect of the voltage, which sometimes did not stop even after two days of measurement and led to further inconsistencies as no baseline voltage could be found.

- Opposing battery voltage: All of the samples showed a more or less pronounced, time dependent battery voltage with opposing polarity to the initial photovoltage. This was often strong enough to heavily impede or sometimes nearly completely negate the photovoltage.

- Cation non-stoichiometry: Since in both the series of undoped and doped samples, clearly the sample with 7 % Sr-compensation (which translates to ideal stoichiometry in the thin film) in the target showed not only the highest photovoltages, but also the most stable voltage profile, it is concluded that deviation from the ideal Sr:Ti or Sr:(Fe+Ti) ratio of 1 is detrimental to the overall behaviour of the PV cells.

- Fe-doping: While Fe-doping in STO is common and has been used in previous works, it appears that in this case, it is clearly for the better when samples are not only ideally stoichiometric but also undoped. Fe-doping led to overall unreliable behaviour and clearly decreased photovoltages, as even the best example, STO 7/2, could not achieve photovoltages above 80 mV, which is just in the range of the worst result of undoped STO, STO 5 with ca. 95 mV.

Still, some interesting observations were made, e.g. the apparent change of polarity in the samples upon reaching or exceeding ideal stoichiometry. Additionally, it was observed that LSM also creates a photoactive space charge region upon contact with STO, akin to LSCr. Though the impedance spectra of the samples could not be fully explained due to sample geometry and missing knowledge about penetration depth of UV light, it seems that the spectrum generally shows a superposition of the effects introduced into the STO by LSM and LSCr. Thus it would probably be a good idea to substitute either of them with an electrode material that behaves differently, as the interaction between the two materials is most decidedly not synergistic in nature. While there might be potential in thin film applications, a lot more research will be necessary to create a reliable cell that can be industrially applied.

Single crystalline samples, on the other hand, showed remarkable results with both LSCr and LSM as WE material. While LSCr-samples initially showed stable open circuit voltage of ca. 1 V that could be reached in a manner of minutes, LSM was similar, though the photovoltage achieved was lower at about 0.8 V. After current enhancement took place, the LSCr-samples were able to generate increased photovoltage of about 1.1 V and the voltage profile appeared even more sharpened with equilibration often taking a minute or less. No such improvement was observed however for LSM, which still achieved the same voltage as before current enhancement. This improvement in photovoltage for LSCr could also be achieved immediately after preparation of the sample by using synthetic air instead of natural air.

More interesting is, however, the impact that a switch from natural to synthetic air had on the generation of photocurrent. While the initial "self-enhancement" of photocurrent of single crystalline STO-LSCr samples in lab air and at 350 °C took about a week to reach an equilibrium of ca 0.8 mA, a sample of the same setup achieved a current of 2.1 mA after just one hour of equilibration. Additionally, while the sample in lab air took 20-40 min to reach I_{eq} again after subsequent illumination, there was no such inhibition when using synthetic air instead. As explained during the course of this work, it is thus assumed that the reason for the long-time "enhancement" is actually an impediment in the form of air contamination which is slowly counteracted by the PV cell. Stoichiometry polarization, which has initially been suspected to be the reason behind this phenomenon, seems unlikely and considering the timescale would rather fit to the initial strong increase in photocurrent upon illumination.

Another interesting aspect is the impact of high-temperature treatment of SC samples on the photocurrent. Prolonged and repeated exposition of the samples to temperatures above 600 °C (maybe even lower) leads to a faster equilibration of photocurrent but also a permanent decrease in the maximum achievable photocurrent. The faster equilibration might although only be a quasi-equilibration with a small additional gain in current over a long timescale (presumably days to weeks) still possible.

While the exact reason for the initial impediment of photocurrent remains unknown, it can be generally said that there are three different ways to eliminate the problem and reach an equilibrium current:

- Long time equilibration, with the obvious downside of the enormous timescale at which the equilibration takes place
- High-temperature annealing, with the downside of a permanently lowered maximum current due to other processes taking place in the cell during the treatment
- Operation of the cell in synthetic air, which seems to be the most accessible way as it only requires the cell to be kept in containers with defined atmospheric composition

Impedance spectroscopy on single crystalline samples typically revealed three distinct features as had already been the case for thin film samples, although the assignment of features was more straightforward in this case. With the high frequency (>1 kHz) feature showing permittivity and conductivity values fitting for STO, this was attributed to the bulk conductivity of the single crystal. The low frequency (>5 Hz) feature showed very high resistances (>1 MΩ) and fully collapsed upon illumination, making it stand to reason to attribute this to the space charge region. Despite the role of the middle frequency feature still remaining unclear, it is most decidedly not connected to the counter electrode, which had been suspected in earlier works.

While there is still a lot of research necessary to be performed on these samples to figure out the actual reason behind most of the samples' behaviour, e.g. why lab air impedes the current flow or why samples with an LSCr electrode gain additional voltage after the first current measurement as well as how exactly higher temperatures impact the defect chemistry and electrical behaviour of STO, as it stands there is a PV cell that can generate >1 V of stable open circuit photovoltage and >2 mA of stable close circuit photocurrent within a timescale of seconds (voltage) to a few minutes (current). Thus, the LSCr-STO PV cell is a reliable candidate for possible future applications in combination with solid oxide fuel cells or solid oxide batteries to harvest and store renewable energy from natural sources.

6 Acknowledgements

All the while during the composition of this thesis, with every source researched, every calculation performed, every graph drawn and every paragraph written, I was thinking about what to put here. I was thinking up witty remarks and clever nods concerning every person I could possibly express my gratitude to.
But now that the work is finished, I somehow find myself at the end of my wordsmithing abilities and none of my initial ideas seems to come to my mind again. A strange feeling indeed, but a cathartic one; as if my mind just got emptied upon the completion of my work. Thus, I will keep this section concise and just give credit where credit is due.

This will of course be Jürgen Fleig, not only for giving me the opportunity to work on this project but also for even initially awakening my interest in the sector of electrochemistry and solid state ionics, (which I would have never thought to pursue when beginning my studies in chemistry) by giving one of the most fun and interesting lectures I have experienced during my Bachelor's and Master's study. Also I would like to thank Alex Schmid for his direct supervision of my work and all the great gadgets that he developed for this group. For all the fun talks, for his quick responds to my e-mails and somehow always finding time in helping me out when I was either at my wit's end or my measurement apparatus just needed another upgrade, I want to say: thank you.

I would like to further thank of course my parents, whose continued support definitely carried me through my studies (I can't stress this enough and feel a bit sorry for not being able to word it any better). Also I would like to thank my brother Laurenz for all the fun times we had so far and surely will continue to have. You are the best brother I could ask for.
I want to give more shout-outs to all my friends and colleagues that have accompanied through these six years of studies. To Michael and Elmar, with whom I would have liked to attend more concerts if not for COVID-19. To Vinzent, Erik and Jo, who made for great colleagues in the lab and when studying for exams. And of course to Felix and Matthias, who were not only always at my side during my studies, but have also become my closest friends in recent years. I love you, guys.
I also thank all of the Antons and especially you, Marlene, just for being the absolute bestest. So without making this section too kitschy, let me just say: You are truly the apple of my eye.

Finally, I would just like to thank everyone else who ever helped me out or just provided me with any kind of entertainment during the relatively bland years of the pandemic without mentioning everyone by name. And I would like to thank you, dear Reader, whoever you might be, for taking the time to show interest in my work.

7 Appendix

List of Figures

List of Tables

References

[1] P. J. Crutzen and E. F. Stoermer, "The Anthropocene," *Global Change Newsletter*, vol. 41, pp. 17 – 18, 2000.

[2] R. K. Pachauri and L. Maier, "Climate Change 2014: Synthesis Report. Contribution of Working Groups I, II and III to the Fifth Assessment Report of the Intergovernmental Panel on Climate Change," *IPCC*, 2014.

[3] N. Armaroli and V. Balzani, "Solar electricity and solar fuels: Status and perspectives in the context of the energy transition," *Chemistry Europe*, vol. 22, pp. 32 – 57, 2016.

[4] S. Philipps, A. Bett, B. Burger, L. Friedrich, C. Kost, S. Nold, D. Peper, R. Preu, J. Rentsch, G. Stryi-Hipp, H. Wirth, and W. Warmuth, "Photovoltaics report," *Fraunhofer ISE*, 2015.

[5] L. Meng, Y. Zhang, X. Wan, C. Li, X. Zhang, Y. Wang, X. Ke, Z. Xiao, L. Ding, R. Xia, H.-L. Yip, Y. Cao, and Y. Chen, "Organic and solution-processed tandem solar cells with 17.3% efficiency," *Science*, vol. 361, pp. 1094 – 1098, 2018.

[6] E. Yablonovitch, O. D. Miller, and S. R. Kurtz, "The opto-electronic physics that broke the efficiency limit in solar cells," *38th IEEE Conference on Photovoltaic Specialists*, pp. 1556 – 1559, 2012.

[7] M. Gloeckler, I. Sankin, and Z. Zhao, "CdTe solar cells at the threshold to 20% efficiency," *IEEE Journal of Photovoltaics*, vol. 3, pp. 1389 – 1393, 2013.

[8] D. L. Young, J. Keane, A. Duda, J. A. AbuShama, C. L. Perkins, M. Romero, and R. Noufi, "Improved performance in ZnO/CdS/$CuGaSe_2$ thin-film solar cells," *Prog. Photovolt: Res. Appl.*, vol. 11, pp. 535 – 541, 2003.

[9] P. P. Boix, S. Agarwala, T. M. Koh, N. Mathews, and S. G. Mhaisalkar, "Perovskite solar cells: Beyond methylammonium lead iodide," *J.Phys.Chem.Lett.*, vol. 6, pp. 898 – 907, 2015.

[10] R. Wang, M. Mujahid, Y. Duan, Z.-K. Wang, J. Xue, and Y. Yang, "A review of perovskites solar cell stability," *Advanced Functional Materials*, vol. 29, 2019. 1808843.

[11] T. Dittrich, V. Duzhko, F. Koch, V. Kytin, and J. Rappich, "Trap-limited photovoltage in ultrathin metal oxide layers," *Phys. Rev. B*, vol. 65, 2002. 155319.

[12] Y. Nishi, T. Miyata, and T. Minami, "Effect of inserting a thin buffer layer on the efficiency in n-ZnO/p-Cu_2O heterojunction solar cells," *Journal of Vacuum Science & Technology A*, vol. 30, 2012. 04D103.

[13] K. P. Musselmann, A. Marin, L. Schmidt-Mende, and J. L. MacManus-Driscoll, "Incompatible length scales in nanostructured Cu_2O solar cells," *Advanced Functional Materials*, vol. 22, pp. 2202 – 2208, 2012.

[14] H. Katsu, H. Tanaka, and T. Kawai, "Anomalous photoconductivity in $SrTiO_3$," *Japanese Journal of Applied Physics 1*, vol. 39, pp. 2657 – 2658, 2000.

[15] M.-H. Huang, J.-Y. Xia, Y.-M. Xi, and C.-X. Ding, "Study on photochromism in $SrTiO_3$:Fe ceramic powder," *Journal of the European Ceramic Society*, vol. 17, pp. 1761 – 1765, 1997.

[16] R. Merkle, R. A. De Souza, and J. Maier, "Optically tuning the rate of stoichiometry changes: Surface-controlled oxygen incorporation into oxides under UV irradiation," *Angew. Chem. Int. Ed.*, vol. 40, pp. 2126 – 2129, 2001.

[17] A. Viernstein, M. Kubicek, M. Morgenbesser, G. Walch, G. C. Brunauer, and J. Fleig, "High-temperature photochromism of Fe-Doped $SrTiO_3$ caused by UV-induced bulk stoichiometry changes," *Advanced Functional Materials*, vol. 29, 2019. 1900196.

[18] G. Walch, B. Rotter, G. C. Brunauer, A. K. Esmaeili, Esmaeiland Opitz, M. Kubicek, J. Summhammer, K. Ponweiser, and J. Fleig, "A solide oxide photoelectrochemical cell with UV light-driven oxygen storage in mixed conducting electrodes," *J. Mater. Chem. A*, vol. 5, pp. 1637–1649, 2017.

[19] G. C. Brunauer, B. Rotter, G. Walch, E. Esmaeili, A. K. Opitz, K. Ponweiser, J. Summhammer, and J. Fleig, "UV-light-driven oxygen pumping in a high-temperature solid oxide photoelectrochemical cell," *Advanced Functional Materials*, vol. 26, pp. 120 – 128, 2016.

[20] M. Morgenbesser, A. Schmid, A. Viernstein, J. de Dios Sirvent, F. Chiabrera, N. Bodenmüller, S. Taibl, M. Kubicek, F. Baiutti, A. Tarancón, and J. Fleig, "$SrTiO_3$ based high temperature solid oxide solar cells: Photovoltages, photocurrents and mechanistic insight," *Solid State Ionics*, vol. 368, 2021. 115700.

[21] S. Roundy, D. Steingart, L. Frechette, P. Wright, and J. Rabaey, "Power Sources for Wireless Sensor Networks," *Lecture Notes in Computer Science*, vol. 2920, pp. 1 – 17, 2004.

[22] M. Wiesenfarth, S. Philipps, A. Bett, K. Horowitz, and S. Kurtz, "Current status of concentrator photovoltaic (CPV) technology," *Fraunhofer ISE*, 2016.

[23] N. Papež, R. Dallaev, S. Talu, and J. Kaštyl, "Overview of the current state of gallium arsenide-based solar cells," *Materials*, vol. 14, 2021. 3075.

[24] C. Mingbo and Z. Zhongwei, "Development of the GaAs solar cell for space application," *Conference Record of the Twenty Fifth IEEE Photovoltaic Specialists Conference*, pp. 121 – 124, 1996.

[25] V. Quaschning, *Regenerative Energiesysteme: Technologie - Berechnung - Klimaschutz. 10. aktualisierte und erweiterte Auflage.* Carl Hanser Verlag München, 2019.

[26] K. Barnham and G. Duggan, "A new approach to high-efficiency multi- band-gap solar cells," *Journal of Applied Physics*, vol. 67, 1990. 3490.

[27] M. J. Montenegro and T. Lippert, "Films for Electrochemical Applications," in *Pulsed Laser Deposition of Thin Films* (R. Eason, ed.), pp. 563 – 584, John Wiley & Sons, 2006.

[28] C. Xu, S. Wicklein, A. Sambri, S. Amoruso, M. Moors, and R. Dittmann, "Impact of the interplay between nonstoichiometry and kinetic energy of the plume species on the growth mode of $SrTiO_3$ thin films," *J. Appl. Phys. D: Appl. Phys.*, vol. 47, 2013. 034009.

[29] N. Chan, "Nonstoichiometry in $SrTiO_3$," *Journal of the Electrochemical Society*, vol. 128, pp. 1762 – 1768, 1981.

[30] X. Wang, Q. Hu, G. Zang, C. Zhang, and L. Li, "Structural and electrical characteristics of Sr/Ti nonstoichiometric $SrTiO_3$ ceramics," *Solid State Communications*, vol. 266, pp. 1 – 5, 2017.

[31] N. Eror and U. Balachandran, "Electrical conductivity in strontium titanate with nonideal cationic ratio," *Journal of Solid State Chemistry*, vol. 42, pp. 227 – 241, 1982.

[32] M. Morgenbesser, S. Taibl, M. Kubicek, A. Schmid, A. Viernstein, N. Bodenmüller, C. Herzig, F. Baiutti, J. de Dios Sirvent, M. O. Liedke, M. Butterling, A. Wagner, W. Artner, A. Limbeck, A. Tarancón, and J. Fleig, "Cation non-stoichiometry in Fe:$SrTiO_3$ thin films and its effect on the electrical conductivity," *Nanoscale Advances*, vol. 3, pp. 6114 – 6127, 2021.

[33] C. Kittel, *Introduction to Solid State Physics*. John Wiley & Sons, 8th ed., 2005.

[34] M. I. Aroyo, ed., *International Tables for Crystallography*, vol. A, ch. 1.3.2. John Wiley & Sons, 6th ed., 2016.

[35] K. Oura, V. Lifshits, A. Saranin, A. Zotov, and M. Katayama, *Surface Science: An Introduction*. Springer, 2003.

[36] D. Chadi, "Atomic and Electronic Structures of Reconstructed Si(100) Surfaces," *Phys. Rev. Lett*, vol. 43, pp. 43 – 46, 1979.

[37] E. Hornbogen, *Werkstoffe - Aufbau und Eigenschaften von Keramik, Metallen, Kunststoffen und Verbundwerkstoffen*. Springer, 9th ed., 2008.

[38] R. J. Borg, *The Physical Chemistry of Solids*. Academic Press, Inc., 1992.

[39] J. Fleig, "Microelectrodes in solid state ionics," in *Advances in Electrochemical Sciences and Engineering, Volume 8*, pp. 1 – 87, John Wiley & Sons, 2002.

[40] F. A. Kroeger and H. J. Vink, "Relations between the Concentrations of Imperfections in Crystalline Solids," *Solid State Physics*, vol. 3, pp. 307 – 435, 1956.

[41] J. C. Mauro, "Diffusion in Crystals," in *Materials Kinetics: Transport and Rate Phenomena*, pp. 129–147, Elsevier, 2020.

[42] D. M. Smyth, "Intrinsic Ionic Disorder," in *The defect chemistry in metal oxides*, pp. 34 – 56, Oxford University Press, 2000.

[43] A. F. Hollemann, E. Wiberg, and N. Wiberg, "Die Gruppe der Alkalimetalle," in *Lehrbuch der Anorganischen Chemie*, ch. 18, pp. 1259–1300, De Gruyter, 102nd ed., 2007.

[44] J. Maier, "Defect Chemistry: Composition, Transport, and Reactions in the Solid State; Part I: Thermodynamics," *Angew. Chem. Int. Ed. Eng.*, vol. 32, pp. 313 – 335, 1993.

[45] J. Maier, "Nano-ionics: More than just a fashionable slogan," *Journal of Electroceramics*, vol. 13, pp. 593 – 598, 2004.

[46] D. M. Smyth, "Lattice Defects and the Law of Mass Action," in *The defect chemistry in metal oxides*, pp. 21 – 33, Oxford University Press, 2000.

[47] H. Rickert, "Disorder in solids," in *Electrochemistry of solids*, pp. 6 – 40, Springer, 1982.

[48] L. Chen, "Yttria-Stabilized Zirconia Thermal Barrier Coatings — A REVIEW," *Surface Review and Letters*, vol. 13, pp. 535 – 544, 2006.

[49] B. Butz, *Yttria-Doped Zirconia as Solid Electrolyte for Fuel-Cell Applications: Fundamental Aspects*. PhD thesis, Karlsruher Institut für Technologie, 2009.

[50] J. Maier, "Introduction," in *Physical Chemistry of Ionic Materials: Ions and Electrons in Solids*, pp. 11 – 22, John Wiley & Sons, 2004.

[51] K. Kosuge, "Non-stoichiometric compounds derived from point defects," in *Chemistry of Non-stoichiometric Compounds*, p. 194, Oxford University Press, 1994.

[52] D. M. Smyth, "Intrinsic Nonstoichiometry," in *The defect chemistry in metal oxides*, pp. 162 – 196, Oxford University Press, 2000.

[53] R. J. Tilley, "Nonstoichiometry and Intrinsic Electronic Conductivity," in *Defects in solids*, pp. 297 – 350, John Wiley & Sons, 2008.

[54] C. Li, J. J. Chew, A. Mahmoud, S. Liu, and J. Sunarso, "Modelling of oxygen transport through mixed ionic-electronic conducting (MIEC) ceramic-based membranes: An overview," *Journal of Membrane Science*, vol. 567, pp. 228 – 260, 2018.

[55] K. Lunze, *Einführung in die Elektrotechnik*. Verlag Technik GmbH, 1991.

[56] D. M. Smyth, "Ionic Transport," in *The defect chemistry in metal oxides*, pp. 91 – 117, Oxford University Press, 2000.

[57] P. Erhart and K. Albe, "Diffusion of zinc vacancies and interstitials in zinc oxide," *Applied Physics Letters*, vol. 88, 2006. 201918.

[58] S. Lany, "Semiconducting transition metal oxides," *Journal of Physics: Condensed matter*, vol. 27, 2015. 283203.

[59] J. Maier, "Ionic Conduction in Space Charge Regions," *Progress in Solid State Chemistry*, vol. 23, pp. 171 – 263, 1995.

[60] X. Guo and Y. Ding, "Grain Boundary Space Charge Effect in Zirconia," *Journal of The Electrochemical Society*, vol. 151, pp. 1 – 7, 2004.

[61] K. Gelderman, L. Lee, and S. Donne, "Flat-Band Potential of a Semiconductor: Using the Mott–Schottky Equation," *Journal of Chemical Education*, vol. 84, pp. 685 – 688, 2007.

[62] R. Waser, "Electronic properties of grain boundaries in $SrTiO_3$ and $BaTiO_3$ ceramics," *Solid State Ionics*, vol. 75, pp. 89 – 99, 1995.

[63] Y. Wu, P. C. Bowes, J. N. Baker, and D. S. Irving, "Influence of space charge on the conductivity of nanocrystalline $SrTiO_3$," *J. Appl. Phys.*, vol. 128, 2020. 014101.

[64] R. A. De Souza and J. Kilner, "Oxygen transport in $La_{1-x}Sr_xMn_{1-y}Co_yO_{3\pm\delta}$ perovskites - Part I. Oxygen tracer diffusion," *Solid State Ionics*, vol. 106, pp. 175 – 187, 1998.

[65] N. DasGupta and A. DasGupta, "Junction Field Effect Transistor and Metal-Semiconductor Field Effect Transistor," in *Semiconductor Devices: Modelling and Technology*, pp. 214 – 233, PHI Learning Limited, 2011.

[66] L. Bergmann, C. Schaefer, and W. Raith, *Festkörper*. No. 6 in Lehrbuch der Experimentalphysik, de Gruyter, 1992.

[67] R. T. Tung, "Formation of an electric dipole at metal-semiconductor interfaces," *Phys. Rev. B*, vol. 64, 2001. 205310.

[68] J. Bardeen, "Surface States and Rectification at a Metal Semi-Conductor Contact," *Phys. Rev.*, vol. 71, pp. 717 – 727, 1947.

[69] V. Heine, "Theory of Surface States," *Phys. Rev.*, vol. 138, 1965. A1689.

[70] M. Balkanski and R. F. Wallis, *Semiconductor Physics and Applications*. Oxford University Press, 2000.

[71] Y. Deshayes and L. Béchou, "State-of-the-Art of Infrared Technology," in *Reliability, Robustness and Failure Mechanisms of LED Devices*, pp. 1 – 44, Elsevier, 2016.

[72] T. Soga, "Fundamentals of Nanostructured Solar Cells," in *Nanostructured Materials for Solar Energy Conversion*, ch. 1, pp. 3 – 43, Elsevier, 2006.

[73] T. Markvart and L. Castañer, "Solar Cells," in *Solar Cells - Materials, Manufacture and Operation*, ch. 1, pp. 3 – 25, Elsevier, 2nd ed., 2013.

[74] S. Leu and D. Sontag, "Crystalline Silicon Solar Cells: Homojunction Cells," in *Solar Cells and Modules* (A. Shah, ed.), vol. 301 of *Springer Series in Materials Science*, ch. 5, pp. 97 – 138, Springer, 2020.

[75] K. W. Böer, "Semiconductor Heterojunctions," in *Survey of Semiconductor Physics*, vol. 5, ch. 20, pp. 676 – 700, Springer Science, 1992.

[76] B. J. Skromme and G. Sujan, "Semiconductor heterojunctions," *Reference Module in Materials Science and Engineering*, 2018.

[77] E. Schubert, L. Tu, G. Zydzik, R. Kopf, A. Benvenuti, and M. Pinto, "Elimination of heterojunction band discontinuities by modulation doping," *Appl. Phys. Lett.*, vol. 60, pp. 466 – 468, 1992.

[78] C. van Opdorp, *Si-Ge isotype heterojunctions*. PhD thesis, Technische Hogeschool Eindhoven, 1969.

[79] W. G. Oldham and A. Milnes, "n-n Semiconductor Heterojunctions," *Solid State Electronics*, vol. 6, pp. 121 – 127, 1963.

[80] J. P. Donnelly and A. Milnes, "The current-voltage characteristics of p-n Ge-Si and Ge-GaAs heterojunctions," *Proceedings of the IEEE*, vol. 113, pp. 1468 – 1476, 1966.

[81] E.-K. Kang, C. I. Yeo, S. J. Kang, J. W. Min, Y. M. Song, and Y. T. Lee, "Improved Light Absorption of GaInP/GaAs/Ge Solar Cell Modules With Micro/Nanoengineered Coverglasses," *IEEE Journal of Photovoltaics*, vol. 5, pp. 1130 – 1136, 2015.

[82] N. D. Gupta and V. Janyani, "Lambertian and photonic light trapping analysis with thickness for GaAs solar cells based on 2D periodic pattern," *IET Optoelectron.*, vol. 11, pp. 217 – 224, 2017.

[83] J. Katayama, K. Ito, M. Matsuoka, and J. Tamaki, "Performance of Cu_2O/ZnO solar cell prepared by two-step electrodeposition," *Journal of Applied Electrochemistry*, vol. 34, pp. 687–692, 2004.

[84] B. Li, Y. Zhang, L. Zhang, and L. Yin, "Graded Heterojunction Engineering for Hole-Conductor-Free Perovskite Solar Cells with High Hole Extraction Efficiency and Conductivity," *Advanced Materials*, vol. 29, 2017. 1701221.

[85] J. He, H. Lindtsröm, A. Hagfeldt, and S.-E. Lindquist, "Dye-Sensitized Nanostructured p-Type Nickel Oxide Film as a Photocathode for a Solar Cell," *J. Phys. Chem. B*, vol. 103, pp. 8940–8943, 1999.

[86] S. Rühle, A. Y. Anderson, H.-N. Barad, B. Kupfer, Y. Bouhadana, E. Rosh-Hodesh, and A. Zaban, "All-Oxide Photovoltaics," *J. Phys. Chem. Lett.*, vol. 3, pp. 3755 – 3764, 2012.

[87] A. Pérez-Tomás, A. Mingorance, D. Tanenbaum, and M. Lira-Cantú, "Metal Oxides in Photovoltaics: All-Oxide, Ferroic, and Perovskite Solar Cells," in *The Future of Semiconductor Oxides in Next-Generation Solar Cells* (M. Lira-Cantú, ed.), Metal Oxides, ch. 8, pp. 267–356, Elsevier, 2018.

[88] J. Wang, Y. Liu, X. Chen, C. Chen, P. Chen, Z. Wang, Y. Duan, *et al.*, "Functional Metal Oxides in Perovskite Solar Cells," *ChemPhysChem*, vol. 20, pp. 2580 – 2586, 2019.

[89] J.-W. Lee, L. Meng, and Y. Yang, "Semiconducting Metal Oxides for High Performance Perovskite Solar Cells," in *The Future of Semiconductor Oxides in Next-Generation Solar Cells* (M. Lira-Cantú, ed.), Metal Oxides, ch. 7, pp. 241 – 266, Elsevier, 2018.

[90] N. G. Elfadill, M. Hashim, K. M. Chahrour, and S. Mohammed, "Preparation of p-type Na-doped Cu_2O by electrodeposition for a p-n homojunction thin film solar cell," *Semicond. Sci. Technol.*, vol. 31, pp. 8–15, 2016.

[91] S. Yang, L. Martin, *et al.*, "Photovoltaic effects in $BiFeO_3$," *Applied Physics Letters*, vol. 95, 2009. 062909.

[92] E. McCalla, J. Walter, and C. Leighton, "A Unified View of the Substitution-Dependent Antiferrodistortive Phase Transition in $SrTiO_3$," *Chem. Mater.*, vol. 28, pp. 7973 – 7981, 2016.

[93] J. Sidoruk, *Konkurrierende ferroische Ordnungsparameter in $SrTiO_3$: Domänenverhalten und Schaltverhalten*. PhD thesis, Georg-August-Universität Göttingen, 2014.

[94] C. Collignon, X. Lin, C. W. Rischau, B. Fauqué, and K. Behnia, "Metallicity and Superconductivity in Doped Strontium Titanate," *Ann. Rev. Condens. Matt. Phys.*, vol. 10, pp. 25–44, 2019.

[95] R. A. De Souza, J. Fleig, J. Maier, O. Kienzle, Z. Zhang, W. Sigle, and M. Rühle, "Electrical and Structural Characterization of a Low-Angle Tilt Grain Boundary in Iron-Doped Strontium Titanate," *J. Am. Ceram. Soc.*, vol. 86, pp. 922–928, 2003.

[96] Y. Yamada, H. Yasuda, T. Tayagaki, and Y. Kanemitsu, "Temperature Dependence of Photoluminescence Spectra of Nondoped and Electron-Doped $SrTiO_3$: Crossover from Auger Recombination to Single-Carrier Trapping," *Phys. Rev. Lett.*, vol. 102, 2009. 247401.

[97] T. Wolfram and S. Ellialtioglu, "Optical properties of the d-band Perovskites," in *Electronic and Optical Properties of d-Band Perovskites*, ch. 7, pp. 138 – 181, Cambridge University Press, 2006.

[98] H. J. Scheel, "Kristallzüchtung und Charakterisierung von Strontiumtitanat $SrTiO_3$," *Zeitschrift für Kristallographie - Crystalline Materials*, vol. 143, pp. 417–428, 1976.

[99] H. J. Scheel and L. Lytvynov, "Flame-Fusion (Verneuil) Growth of Oxides," in *Crystal Growth Technology: From Fundamentals and Simulation to Large-scale Production* (H. J. Scheel and P. Capper, eds.), ch. 16, pp. 415–433, Wiley-VCH, 2nd ed., 2011.

[100] R. A. De Souza, J. Fleig, R. Merkle, and J. Maier, "$SrTiO_3$: a model electroceramic," *Z. Metallkunde*, vol. 94, pp. 218–225, 2003.

[101] R. Moos and K. H. Hardtl, "Defect Chemistry of Donor-Doped and Undoped Strontium Titanate Ceramics between 1000 and 1400 °C," *J. Am. Ceram. Soc.*, vol. 80, pp. 2549–2562, 1997.

[102] M. Siebenhofer, F. Baiutti, J. de Dios Sirvent, T. M. Huber, A. Viernstein, S. Smetaczek, C. Herzig, M. O. Liedke, M. Butterling, A. Wagner, E. Hirschmann, A. Limbeck, A. Tarancón, J. Fleig, and M. Kubicek, "Exploring point defects and trap states in undoped $SrTiO_3$ single crystals," *Journal of the European Ceramic Society*, vol. 42, pp. 1510 – 1521, 2022.

[103] R. A. De Souza, "Oxygen Diffusion in $SrTiO_3$ and Related Perovskite Oxides," *Advanced Functional Materials*, vol. 25, pp. 6326 – 6342, 2015.

[104] R. Merkle and J. Maier, "How Is Oxygen Incorporated into Oxides? A Comprehensive Kinetic Study of a Simple Solid-State Reaction with $SrTiO_3$ as a Model Material," *Angew. Chem. Int. Ed.*, vol. 47, pp. 3874 – 3894, 2008.

[105] R. A. Maier, A. C. Johnston-Peck, and M. P. Donohue, "(Magic Dopant) Amphoteric Behavior of a Redox-Active Transition Metal Ion in a Perovskite Lattice: New Insights on the Lattice Site Occupation of Manganese in $SrTiO_3$," *Advanced Functional Materials*, vol. 26, pp. 8325–8333, 2016.

[106] A. Viernstein, *Oxygen Stoichiometry Changes in $SrTiO_3$ under UV Illumination*. PhD thesis, Technische Universität Wien, 2021.

[107] C. Khattak and D. Cox, "Structural Studies of the (La,Sr)CrO_3 system," *Materials Research Bulletin*, vol. 12, pp. 463–472, 1977.

[108] D. Meadowcroft, "Some properties of strontium-doped lanthanum chromite," *J. Phys. D: Appl. Phys.*, vol. 2, pp. 1225–1233, 1969.

[109] J. W. Fergus, "Lanthanum chromite-based materials for solid oxide fuel cell interconnects," *Solid State Ionics*, vol. 171, pp. 1–15, 2004.

[110] S. Wang, K. Huang, B. Zheng, J. Zhang, and S. Feng, "Mild hydrothermal synthesis and physical property of perovskite Sr doped $LaCrO_3$," *Materials Letters*, vol. 101, pp. 86–89, 2013.

[111] T. Wei, L. Jia, J.-L. Luo, B. Chi, J. Pu, and J. Li, "CO_2 dry reforming of CH_4 with Sr and Ni co-doped $LaCrO_3$ perovskite catalysts," *Applied Surface Science*, vol. 506, 2020. 144699.

[112] A. Mackor and G. Blasse, "Visible-light induced photocurrents in $SrTiO_3$-$LaCrO_3$ single-crystalline electrodes," *Chemical Physics Letters*, vol. 77, pp. 6 – 8, 1981.

[113] H. Anderson, M. Nasrallah, B. Flandermeyer, and A. Agarwal, "High-temperature redox behavior of doped $SrTiO_3$ and $LaCrO_3$," *Journal of Solid State Chemistry*, vol. 56, pp. 325 – 334, 1985.

[114] N. Kuganathan, F. Baiutti, A. Tarancón, J. Fleig, and A. Chroneos, "Defect energetics in the $SrTiO_3$-$LaCrO_3$ system," *Solid State Ionics*, vol. 361, 2021. 115570.

[115] I. Koriba, B. Lagoun, A. Guibadj, S. Belhadj, A. Ameur, and A. Cheriet, "Structural, electronic, magnetic and mechanical properties of three $LaMnO_3$ phases: Theoretical investigations ," *Computational Condensed Matter*, vol. 29, 2021. e00592.

[116] J.-L. Ortiz-Quiñonez, L. Carcía-González, F. E. Cancino-Gordillo, and U. Pal, "Particle dispersion and lattice distortion induced magnetic behavior of $La_{1-x}Sr_xMnO_3$ perovskite nanoparticles grown by salt-assisted solid-state synthesis," *Materials Chemistry and Physics*, vol. 246, 2020. 122834.

[117] C. Monterrubio-Badillo, H. Ageorges, T. Chartier, J. Coudert, and P. Fauchais, "Preparation of $LaMnO_3$ perovskite thin films by suspension plasma spraying for SOFC cathodes," *Surface and Coatings Technology*, vol. 200, pp. 3743 – 3756, 2006.

[118] X. Yin, L. Shen, S. Wang, B. Wang, and C. Shen, "Double adjustment of Co and Sr in $LaMnO_{3+\delta}$ perovskite oxygen carriers for chemical looping steam methane reforming," *Applied Catalysis B: Environmental*, vol. 301, 2021. 120816.

[119] O. Kwon, R. Huang, T. Cao, J. M. Vohs, and R. J. Gorte, "Dry reforming of methane over Ni supported on $LaMnO_3$ thin films," *Catalysis Today*, vol. 382, pp. 142 – 147, 2021.

[120] R. Sorita and T. Kawano, "A highly selective CO sensor: screening of electrode materials," *Sensors and Actuators B*, vol. 35-36, pp. 274 – 277, 1996.

[121] M. E. Orazem and B. Tribollet, "Electrical Circuits," in *Electrochemical Impedance Spectroscopy*, The Electrochemical Society Series, ch. 4, pp. 75 – 88, John Wiley & Sons, 2nd ed., 2017.

[122] B. Hirschorn, M. E. Orazem, B. Tribollet, V. Vivier, I. Frateur, and M. Musiani, "Determination of effective capacitance and film thickness from constant-phase-element parameters," *Electrochimica Acta*, vol. 55, pp. 6218 – 6227, 2010.

[123] M. E. Orazem and B. Tribollet, "Methods for Representing Impedance," in *Electrochemical Impedance Spectroscopy*, The Electrochemical Society Series, ch. 17, pp. 467 – 492, John Wiley & Sons, 2nd ed., 2017.

[124] D. P. Norton, "Pulsed Laser Deposition of Complex Materials: Progress Toward Applications," in *Pulsed Laser Deposition of Thin Films: Applications-Led Growth of Functional Materials* (R. Eason, ed.), ch. 1, pp. 1 – 31, John Wiley & Sons, 2007.

[125] R. A. De Souza and V. Metlenko, "Behavior of oxygen vacancies in single-crystal $SrTiO_3$: Equilibrium distribution and diffusion kinetics," *Phys. Rev. B*, vol. 85, 2012. 174109.

[126] C. Ahamer, A. K. Opitz, G. M. Rupp, and J. Fleig, "Revisiting the Temperature Dependent Ionic Conductivity of Yttria Stabilized Zirconia (YSZ)," *J. Electrochem. Soc.*, vol. 164, pp. 790 – 803, 2017.

[127] N. F. Muhamad, R. A. Maulat Osman, M. S. Idris, and M. N. Mohd Yasin, "Physical and electrical properties of $SrTiO_3$ and $SrZrO_3$," *EPJ Web of conferences*, vol. 162, 2017. 01052.

[128] R. A. Maier and C. A. Randall, "Low-Temperature Ionic Conductivity of an Acceptor-Doped Perovskite: I. Impedance of Single-Crystal $SrTiO_3$," *J. Am. Ceram. Soc.*, vol. 99, pp. 3350 – 3359, 2016.